SLAC-R-516
UC-404
(SSRL-M)

DETERMINATION OF INTERFACIAL ROUGHNESS USING X-RAY SCATTERING

Anneli Munkholm

Stanford Linear Accelerator Center
Stanford Synchrotron Radiation Laboratory
Stanford University, Stanford, California 94309

May 1997

Prepared for the Department of Energy under contract number DE-AC03-76SF00515

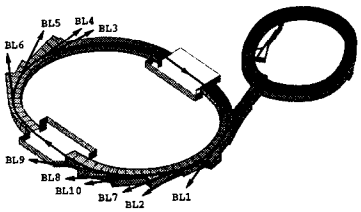

Printed in the United States of America. Available from the National Technical Information Service, U.S. Department of Commerce, 5285 Port Royal Road, Springfield, Virginia 22161

* Ph.D. thesis

DETERMINATION OF INTERFACIAL ROUGHNESS USING X-RAY SCATTERING

A DISSERTATION
SUBMITTED TO THE DEPARTMENT OF MATERIALS SCIENCE AND ENGINEERING
AND THE COMMITTEE ON GRADUATE STUDIES
OF STANFORD UNIVERSITY
IN PARTIAL FULFILLMENT OF THE REQUIREMENTS
FOR THE DEGREE OF
DOCTOR OF PHILOSOPHY

By
Anneli Munkholm
May 1997

Back of

~~Title~~

Page ii

is

blank

Abstract

Crystal truncation rod (CTR) scattering is shown to be a powerful technique for determining interfacial roughness non-destructively. By measuring the decay of scattering away from a Bragg reflection in the surface direction an rms roughness of the surface or interface can be extracted. We obtain rms roughness values with an accuracy of ± 0.1 Å. Sensitivity to lateral length scale roughness ranges from the wavelength of the x-rays to between 1000-10000 Å depending on the instrument function and the specific truncation rod.

The influence of different cleans, as well as the thermal oxidation process, on the Si-SiO_2 interface is investigated. A hot water treatment prior to the thermal oxidation is shown to roughen the Si-SiO_2 interface. CTR scattering results also show a smoothing of the interface as a result of the oxidation process even for as little as 60 Å of thermal oxidation.

Comparison between AFM and CTR scattering gives a consistent picture of the relative roughness of the wafers, although the absolute numbers do not agree. The differences in the absolute values can be explained by the lateral roughness scale that the two techniques measure, indicating that it is at periodicities below $\sim$100 Å that the increased roughness observed by the x-rays is found.

Crystal truncation rods are shown to be perpendicular to the surface and not along the crystallographic axes of a miscut crystal. It is shown that for a crystal terminated by a regular step array both an atomistic and a continuum description of CTR scattering give identical results. Furthermore, the atomistic approach is used to show that a diamond cubic surface with a miscut is inherently rough. Even for a small miscut the tilt of the CTR with respect to the crystallographic axes results in

complications for measuring the rod intensity. We present schemes for determining the exact position of the CTR in reciprocal space and for measuring the miscut of a single crystal. These methods were applied to the measurement of CTR intensities of silicon(001) wafers with miscuts of 0.1 and 4 degrees.

Contents

List of Tables

List of Figures

Chapter 1

Introduction

1.1 Motivation

Integrated circuitry based on metal-oxide-semiconductor field effect transistors (MOSFETs) is the dominant technology in the semiconductor industry. At the heart of each of these transistors is a gate which controls the flow of electrons through a channel between a source and a drain. The name *field effect* refers to the control of the conductivity within the channel caused by the presence of an electric field. Between the gate and the channel is a very thin dielectric, creating in effect a capacitor. Generally, this dielectric is a thermal oxide grown directly on the silicon wafer. This oxide film, known as the gate oxide, is critical to the proper functioning of the FET transistor. If there is leakage through the gate oxide, the device draws too much current. If the breakdown voltage is too small, the field in the channel is too low and one cannot control the current between the source and drain.

The quality of the gate oxide is critical for device characteristics. For a typical bias of 5 V over a gate oxide with a thickness of 60 Å the actual electric field is 8.3 MV/cm. To avoid leakage through the gate, the gate oxide needs to have a very high dielectric constant, and its properties need to be uniform across the width of the gate. One parameter which can significantly effect device properties is surface and interfacial roughness. Increased roughness of the silicon substrate before oxidation has been shown to result in lower charge-to-breakdown and increased defect-related breakdown [1]. Roughness of the Si-SiO_2 interface has also been shown to decrease the electron channel mobility due to enhanced scattering of carriers off the roughness at the interface [2]. As device sizes decrease, the importance of interfacial roughness on the quality of gate oxides increases. With future generations of gate oxide thicknesses expected to be 35-50Å, both surface and interfacial roughness can dramatically effect device performance. In order to optimize the process parameters for a smoother interface, a technique is desired which can measure the interfacial roughness non-destructively.

X-ray reflectivity measurements have proven to be a powerful technique for measuring the surface roughness with atomic resolution [3, 4]. This technique takes advantage of the external reflection of x-rays at low angles. Due to the index of

refraction of most materials being slightly less than one in the x-ray region, there exists a critical angle below which the rays only penetrate evanescently into the top atomic layers. In a specular reflectivity experiment the momentum transfer is along the surface normal, which means that one is sensitive to all the surfaces and interfaces in the sample. For a single thin film on a substrate, especially one which has an index of refraction close to that of the substrate, it is difficult to separate the roughness effect of the top surface from that of the interface. Several groups have used x-ray reflectivity to study oxide films, including native oxides, room-temperature dry oxides and wet thermal oxides. [5, 6, 7, 8].

Grazing incidence x-ray scattering (GIXS) has also been used in the past to characterize the Si-SiO_2 interface [9, 10]. However, in GIXS the scattering vector is nearly parallel to the plane of the sample, so this technique is sensitive to in-plane surface structure, but not interfacial roughness.

Atomic force microscopy (AFM), which was invented in 1986 [11], has since been used widely in industry for characterizing the surface morphology of silicon wafers prior to oxidation. The surface morphology is imaged by scanning a tip over the surface. The tip is attached to a cantilever which deflects as the tip rides over the surface. Forces acting between the tip and the sample surface causes the cantilever to bend, which is registered by a laser beam deflecting off the cantilever. It is capable of sub-Angstrom vertical resolution and produces a real space image of the surface. However, even though this technique can measure the effect of pre-oxidation cleaning on the morphology of the surface, it cannot measure the roughness at the actual Si-SiO_2 interface after oxide growth. In order to do so, one needs to strip off the oxide using chemicals, which leaves some concern that the morphology of the surface measured does not correspond to that of actual interface. In spite of this concern, this etch back technique is commonly used both with AFM and STM (Scanning Tunneling Microscopy) to obtain information of the effect of processing parameters on interfacial roughness [12, 13, 14, 15].

Over the past decade x-ray scattering techniques have been developed to study the truncation of bulk order in crystalline materials [16, 17]. By measuring only

the termination of bulk order, the roughness of the Si-SiO_2 interface can be determined independently of the top surface roughness. The measurement is performed by studying the decay of the scattered x-ray intensity away from a bulk diffraction peak in the direction of the surface. This fall-off in intensity is known as a Crystal Truncation Rod, or CTR. CTR scattering was initially demonstrated by Andrews & Cowley in 1985. They developed a continuum model to describe the scattering of Bragg tails in the direction of the surface. It was also shown experimentally that the rods were perpendicular to the surface, so that if a miscut is present, the rod intensity is along the surface normal rather than the crystallographic axes. I.K. Robinson shortly thereafter used a layer-summation method to describe the rod intensity. Several rods on metal surfaces (W, Pt) were measured and showed good agreement with his theoretical predictions. Both of these models will be described in greater detail in Chapter 2. These two papers along with the availability of synchrotron radiation sources caused a wide range of CTR scattering experiments to be performed in the following years. Many of these early studies of CTRs involved the study of interface structures [18, 19, 20, 21]. Another type of experiment conducted was the study of clean surfaces where the goal was to determine the rearrangement (reconstruction or relaxation) of the top layers of the bulk crystal [22, 23]. CTR scattering has also been applied to studies of a phase transition of the Au(001) surface [24], surface roughening of Ge(001) [25] and surface segregation studies of the $Cu_3Au(001)$ surface [26]. Theoretical work has also continued by introducing new models for the termination of a crystal [27, 28]. Takahashi and Nakatani [29, 30] confirmed that 3-beam effects are negligible in the tails of the Bragg peak, so that a kinematic theory is sufficient for considering CTR scattering.

Cowley *et al.* were the first to employ CTR scattering to measure the interfacial roughness of the Si-SiO_2 interface [31, 32]. For silicon wafers terminated by thermal oxides of 0, 30 and 50 Å thickness they obtained zero roughness, which is in agreement with their x-ray reflectivity results on these same samples. However, due to experimental difficulties, their error bars are relatively large ($\sim$ 2 Å). More recently, K. Evans-Lutterodt and his group have investigated wafers of technological interest [33]. They used a continuum model similar to that proposed by Andrews & Cowley to

model their data, using a Gaussian roughness to describe the interface. The rms roughness was extracted from three different rods on the wafer, which resulted in different rms values, the largest range being 2.0-2.9 Å for a single wafer. Since their first publication they have reported results on the roughness dependence on the growth temperature [34], on nitrogenated oxides [35], on oxide thicknesses [36] and most recently discussed the spectral sensitivity of the technique [37].

1.2 Content and Structure of Thesis

In this thesis I have explored the use of crystal truncation rod scattering using synchrotron radiation for measuring the interfacial roughness of the Si-SiO_2 interface. The influence of different cleaning procedures on the resulting interfacial roughness was investigated. To emphasize the utility of this technique for buried interfaces, the silicon(001) surface/interface was measured both before and after the growth of a thermal oxide. A large emphasis of this work has been on investigating industrially interesting samples through collaborations with Hewlett-Packard, Intel and Texas Instruments. Since AFM is the preferred technique in industry for measuring the roughness of the silicon surface, results obtained by both AFM and CTR scattering from the same wafers were compared. Miscut of single crystals and its effect on CTR's have been assumed to be negligible in previous studies. Since all real crystals are miscut, it is important to examine whether this assumption holds. The effect of miscut on CTR's is investigated both in theory and practice for silicon wafers with a miscut of up to four degrees.

A brief introduction of x-ray diffraction is given in Chapter 2. This chapter will discuss previous theories developed to describe CTR's and the influence on CTR intensity profiles of surface effects such as roughness, reconstruction and relaxation.

Since only the surface atoms are contributing to the scattering far from the Bragg peaks, the rod intensity is very low. Using synchrotron radiation enables us to measure these intensities. The experimental procedures as well as the beam line optical components are described in Chapter 3.

The influence of roughness on CTR scattering is examined in detail in Chapter 4.

A modified theory is proposed for CTR's which is used throughout this thesis to fit the experimental data. The lateral roughness length scales at which CTR scattering is sensitive are determined. They depend on beam coherence, the bandpass of the monochromator and the instrument function. The roughness of the Si-SiO_2 interface is measured for a variety of cleans and thermal oxidation processes. Finally, a comparison of the surface roughness obtained with AFM and CTR scattering is done.

Miscut of single crystals causes the CTR's to be tilted with respect to the crystallographic axes. The theory is shown both for a single cubic and a diamond cubic lattice in Chapter 5. Both an atomistic and a continuum approach give the same rod intensity for a regular step array. One interesting result is that a regular step array of a simple cubic lattice does not affect the CTR intensity, only the position of the rod in reciprocal space. However a diamond cubic crystal with a miscut is shown to be inherently rough. A method is presented for determining the size of the miscut and its direction. Since the rods and the crystallographic axes are no longer aligned it is more problematic to determine the position of the CTR. A new method is proposed for locating the exact rod position, which is shown to yield reliable and consistent data for a number of wafers.

Conclusions are given in Chapter 6.

Chapter 2

Crystal Truncation Rod Scattering

Summary

The basic concepts of X-ray scattering will briefly be reviewed at the beginning of this chapter. The phenomenon of Crystal Truncation Rod (CTR) scattering which arises due to the termination of the crystal at the surface will be described as well. Two theories are presented which calculate the rod intensity based on a continuum and an atomistic model, respectively. A variety of surface effects, such as roughness, relaxation, reconstruction etc. and their influence on the CTR intensity will be discussed with an emphasis on (001) oriented silicon. It will be shown that relaxation and reconstruction result in a decay of the rod intensity which is not symmetric about the Bragg peak, whereas roughness results in a symmetric decay. Thus the two effects are separable.

2.1 X-ray Scattering

X-ray scattering has long been known to be a powerful tool for studying the atomic arrangements of matter, since the wavelength of x-rays is comparable to interatomic distances ($\sim$ 1 Å). Photons scattering from a periodic array interfere constructively along specific scattering directions, whereas they destructively interfere along all other directions. Diffraction from periodic structures such as crystals, multilayers, and superlattices is, in the kinematic limit, governed by Bragg's law:

$$\lambda = 2d \sin\theta, \tag{2.1}$$

where θ is the Bragg angle for incident x-rays with wavelength λ scattering off a material with a periodicity of d (see for example [38]). Bragg's law can also be expressed in terms of the scattering vector $\vec{Q}$, which corresponds to the momentum transfer of the diffraction process. $\vec{Q}$ is defined as the difference between the incident ($\vec{k_i}$) and outgoing ($\vec{k_o}$) wave vector of the x-rays onto the sample:

$$\vec{Q} = \vec{k_o} - \vec{k_i}. \tag{2.2}$$

A schematic of this relation ship is shown in Figure 2.1a. Since the length of a wave vector is $2\pi/\lambda$ the diffraction condition can be written as:

$$|\vec{Q}| = \frac{4\pi \sin\theta}{\lambda} = \frac{2\pi}{d}. \tag{2.3}$$

Thus, the length of the scattering vector is inversely related to the d-spacing probed. Also note that the scattering vector is perpendicular to the planes from which diffraction of x-rays occurs.

It is often convenient to describe the diffraction condition in terms of a reciprocal lattice, which is the Fourier transform of the electron density within the crystal. Although this is a mathematical construct, it turns out that the diffraction condition is satisfied when a scattering vector coincides with a reciprocal lattice point. Thus, reciprocal space is the map of all the allowed reflections. For a simple cubic lattice with cell dimensions a, the reciprocal lattice is also simple cubic, however the length of the cell is $2\pi/a$. Let $\vec{h}, \vec{k}$ and $\vec{l}$ represent the axes of the reciprocal lattice, then

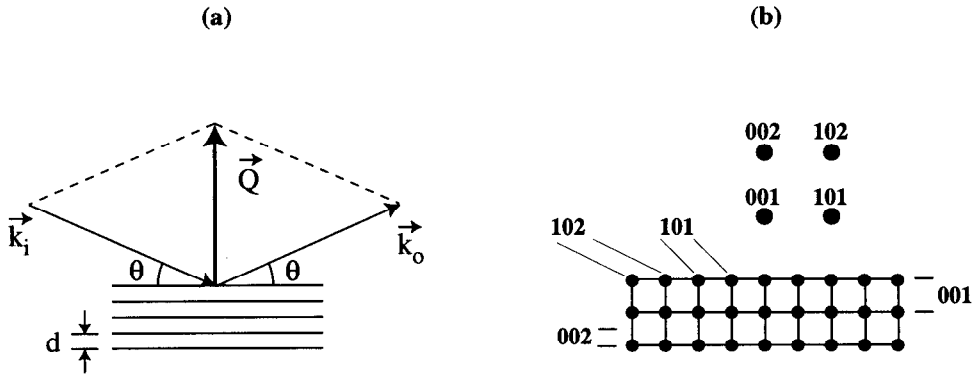

Figure 2.1: (a) Symmetric scattering geometry showing the relationship between the scattering vector $\vec{Q}$ and the incident and outgoing k-vectors when diffraction is occurring from planes with a d-spacing given by Bragg's law. (b) Schematic of the relationship between planes in real space and points in reciprocal space.

diffraction from the (hkl) plane in real space corresponds to the scattering vector pointing from the origin to the hkl reciprocal lattice point. Although reciprocal space is infinitely large, the number of measurable Bragg peaks is limited by the photon energy ($E = hc/\lambda$) and the accessible diffraction angles of the diffractometer. The smallest d-spacing that theoretically can be probed is equal to half the wavelength of the x-rays, which can be seen by considering Bragg's law in backscattering geometry.

The nature of a Fourier transform causes long wavelength periodicities in real space to be close to the origin in reciprocal space and vice versa, e.g. planes with a small d-spacing result in a point further away from the origin than planes with a larger d-spacing. This is illustrated in Figure 2.1b where the relationship between planes in real space and the corresponding point in reciprocal space is shown for a simple cubic lattice. In order to understand the concept of crystal truncation rod scattering, it is illustrative to first consider how 1D, 2D, and 3D objects in real space are represented in reciprocal space. As described above, a 3D lattice gives rise to points in reciprocal space. The Fourier transform of a 2D lattice, such as a monolayer of adsorbates on a surface, is a set of rods of constant intensity perpendicular to the monolayer. For a 1D array of atoms, e.g. a quantum wire, the Fourier transform into reciprocal space is sheets of uniform intensity which are perpendicular to the wire.

2.2 CTR Theories

CTR's are regions of additional scattered x-ray intensity associated with each Bragg reflection. This extra intensity is perpendicular to the surface and arises from the termination of the bulk crystal, with a more abrupt termination resulting in a more intense streak. The phenomenon can be thought of as a relaxation of the diffraction condition in the direction perpendicular to the surface, so that the points of scattered intensity in reciprocal space representing an infinite crystal become rods of intensity in the direction where the crystal becomes finite. These rods are most intense at the Bragg peaks and the intensity decays as the distance from the Bragg peak increases.

2.2.1 Continuum Model

In the theory for surface scattering by Andrews and Cowley [16] the crystal is described as an infinite lattice multiplied by a shape function. This shape function describes the termination of the lattice, i.e. the value of the shape function corresponds to the completeness of the lattice. In the case of a perfectly flat crystal this is the Heaviside function:

$$\begin{aligned} \rho(z) &= \rho_0 \qquad \text{for z} < 0 \\ \rho(z) &= 0 \qquad \text{for z} \geq 0 \end{aligned} \tag{2.4}$$

The scattered intensity is given by the absolute square of the Fourier transform of the electron density, hence the intensity is given by the absolute square of the convolution of the Fourier transform of the crystal lattice (its reciprocal lattice) with the Fourier transform of the shape function. Thus, in the case of a Heaviside function, each Bragg peak is convoluted with tails of the form $1/q_\perp^2$, where $q_\perp$ is the component of the scattering vector in the direction of the surface relative to the Bragg peak. Therefore, the intensity along a specific rod is given by:

$$I = \sum_{\vec{\tau}} \frac{|\rho_0(\vec{\tau})|^2}{q_\perp^2} \tag{2.5}$$

where ρ_0 is the average electron density of the crystal. $\vec{q}_\perp$ corresponds to the reduced scattering vector, which is the out-of-plane momentum transfer relative to the Bragg

condition is relaxed along the [001] direction, then the above equation can be written as:

$$I = |f_0|^2 N_1^2 N_2^2 \frac{1}{2\sin^2(\pi l)}, \qquad h, k = integer \tag{2.10}$$

where the last term results in streaks of intensity between the Bragg peaks in the [001] direction. The same is true for the [100] and [010] directions, if the diffraction condition is relaxed along one of those directions. Robinson explains the existence of rods along the surface normal as being due to the sharp termination of the lattice in that direction. However, there are no rods in the in-plane directions of the crystal, since in those directions the termination is defined by the beam coherence length, which is not a sharp boundary.

Equation 2.10 is identical to the intensity calculated using Andrews and Cowley's approach, which can be seen from the mathematical equality [39]:

$$\frac{1}{\sin^2(\pi l)} = \sum_{n=-\infty}^{\infty} \frac{1}{\pi^2 (l-n)^2} = \sum_{\vec{\tau}} \frac{1}{a^2 q_\perp^2} \tag{2.11}$$

Thus, the summation of the intensity from the Bragg peaks of a rod is equal to the periodic expression obtained from the sum of the structure factor for the atomic layers. Figure 2.2 shows the intensity for each rod and the summation of all of them. Note, Eqn 2.11 is only true when the layer summation method is not sensitive to the exact termination of the bulk, i.e. for crystals in which the layer spacing perpendicular to the surface is uniform.

2.3 Effect of Crystal Structure on CTR Scattering

For a crystal structure which is not simple cubic certain Bragg reflections are forbidden and the CTR scattering from those reflections also disappears. Using the theory developed by Robinson it can be shown that the basis of a unit cell effects the CTR intensity of the allowed reflections as well. Silicon has a diamond cubic lattice which is shown as a schematic in Figure 2.3. Expanding the theory by Robinson to a diamond cubic lattice with an (001) termination is more easily done by using surface units rather than bulk units. The surface unit cell of a diamond cubic structure is shown

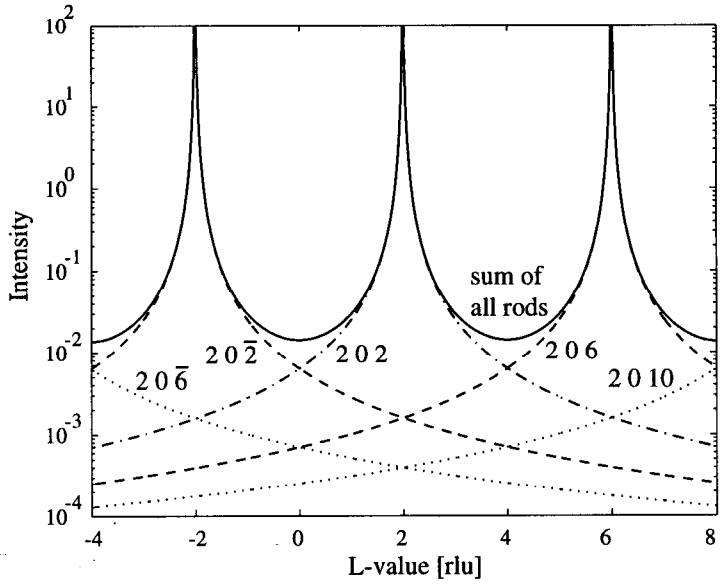

Figure 2.2: CTR intensity calculation for the $(20l)$ rod of a silicon(001) crystal. The solid line corresponds to the atomistic model by Robinson, whereas the dashed lines represent intensity from each Bragg peak using the continuum model by Andrews & Cowley. A sum over all the dashed lines yields the solid curve.

on the right in Figure 2.4. The unit cell in surface units is tetragonal with the same out-of-plane lattice length c as for the cubic unit cell ($c = a_0 = 5.431$ Å). The basis of the surface unit cell is rotated 45 degrees with respect to the in-plane vectors of the cubic unit cell, so that

$$[100]_{surf} = \frac{1}{2}[1\bar{1}0]_{bulk} \tag{2.12}$$

$$[010]_{surf} = \frac{1}{2}[110]_{bulk} \tag{2.13}$$

$$[001]_{surf} = [001]_{bulk}. \tag{2.14}$$

This tetragonal unit cell has 4 atoms per cell so the volume is only half that of the cubic unit cell. The diamond cubic crystal can be described as a sum of planes of atoms which are perpendicular to the [001] direction as in the case of the simple cubic lattice. However, in the case of a diamond cubic lattice, two types of planes are present (A & B) as indicated in Figure 2.4. The structure factor from each bilayer

(which has a basis of two atoms) is:

$$\begin{aligned} F_{DC-bilayer} &= f_0(1+e^{2\pi i(\frac{k}{2}-\frac{l}{4})})\sum_{j_1=0}^{N_1-1} e^{2\pi i h j_1}\sum_{j_2=0}^{N_2-1} e^{2\pi i k j_2} \\ &= f_0(1+e^{\pi i(k-\frac{l}{2})})\left(\frac{e^{2\pi i h N_1}-1}{e^{2\pi i h}-1}\right)\left(\frac{e^{2\pi i k N_2}-1}{e^{2\pi i k}-1}\right), \end{aligned} \tag{2.15}$$

where h, k and l refer to the surface unit cell. Although the structure factor for the crystal is determined using surface units, the reference to the rods is kept in bulk units in this thesis.

The structure factor of a diamond cubic crystal with a perfectly smooth surface is given by summing the structure factor of the bilayers over all the bilayers present in the crystal:

$$\begin{aligned} F_{DC} &= F_{DC-bilayer}\sum_{j_3=1}^{N_3}(1+e^{2\pi i(\frac{h}{2}+\frac{k}{2}-\frac{l}{2})})e^{2\pi i l j_3} \\ &= f_0(1+e^{\pi i(k-\frac{l}{2})})(1+e^{\pi i(h+k-l)})* \\ &\quad \left(\frac{e^{2\pi i h N_1}-1}{e^{2\pi i h}-1}\right)\left(\frac{e^{2\pi i k N_2}-1}{e^{2\pi i k}-1}\right)\left(\frac{e^{2\pi i l N_3}-1}{e^{2\pi i l}-1}\right). \end{aligned} \tag{2.16}$$

The two first products correspond to the basis of the unit cell, whereas the last three products are each a sum over the unit cells in the different crystallographic directions. The intensity from a perfectly flat crystal with a diamond cubic lattice is therefore:

$$\begin{aligned} I_{DC} &= |f_0|^2\cos^2(\frac{\pi}{2}(h+k-l))\cos^2(\frac{\pi}{4}(2h-l))* \\ &\quad \left(\frac{\sin^2(\pi h N_1)}{\sin^2(\pi h)}\right)\left(\frac{\sin^2(\pi k N_2)}{\sin^2(\pi k)}\right)\left(\frac{\sin^2(\pi l N_3)}{\sin^2(\pi l)}\right). \end{aligned} \tag{2.17}$$

As mentioned earlier, the layer summation method is sensitive to the termination of the bulk if the atomic layer spacing perpendicular to the surface is non-constant, such as for a Si(111) surface. However, this is not an issue for the (001) termination of silicon. Using the equation derived above, the rod intensity is calculated for the $< 111 >$ type reflections and shown in Figure 2.4. The $(11l)$ and $(1\bar{1}l)$ rods correspond to the solid and dashed lines, respectively. The diamond cubic lattice of silicon (spacegroup $Fd\bar{3}m$) has a four-fold screw axis (4_1) along the [001] direction. Due to

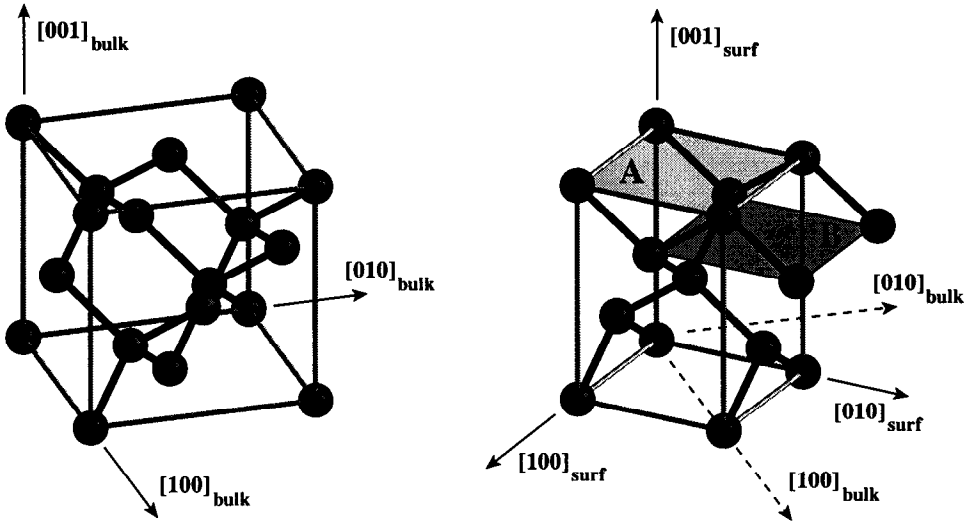

Figure 2.3: A diagram of the diamond cubic lattice of silicon. The unit cell shown on the left is the bulk unit cell, whereas the cell on right is the surface unit cell. A silicon crystal can be described as a stacking of the bilayer sequence AB along the [001] direction.

the center of symmetry imposed onto the structure when using x-ray scattering, the Bragg reflections show 4-fold symmetry, however as shown in Figure 2.4 the rods do not. This is due to the atomic configuration of the (110) and $(1\bar{1}0)$ planes, which are identical, but translated by a quarter of a unit cell according to the screw axis. A perfectly flat surface will terminate the (110) and $(1\bar{1}0)$ planes at different places within the repeat unit, so that the (110) half-plane differs from the $(1\bar{1}0)$ half-plane. All rods which are sensitive to the difference between these half-planes will show a change depending on which surface actually terminates the bulk. The only rods for which this is not true are the $< 10l >$ type planes, where, for instance, the (202) and (022) rods have identical decays of intensity. As will be shown in Chapter 5, however, the presence of a miscut surface will result in equal densities of both surface terminations, which means that this crystal structure asymmetry is not observed even for crystals with miscuts as small as 0.1 degrees.

The influence of the zincblende crystal structure on CTR scattering has been studied for GaAs [40]. Due to the different scattering power of Ga and As the asymmetry

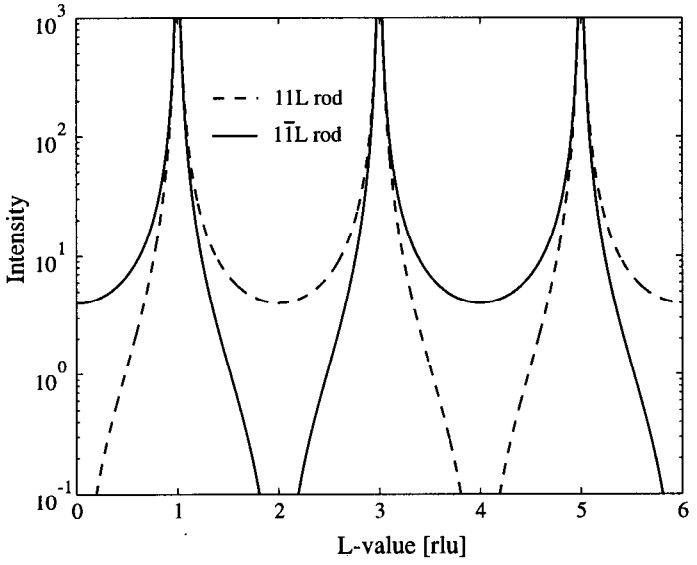

Figure 2.4: CTR intensity for a perfectly flat diamond cubic crystal calculated using the layer summation method.

between the different types of rods is more pronounced than for silicon. In fact a difference is observed but the effect is much smaller than anticipated. This is believed to be due to roughness and the presence of steps on the surface.

2.4 Effect of Surface Structure on CTR Scattering

Crystal Truncation Rods arise from a change in electron density of the bulk lattice and are, therefore, affected by all phenomena which influence the electron density profile of the bulk lattice. Although this thesis is mainly focused on determination of the roughness of an interface, it is important to clarify how various surface and interface effects influence the CTR intensity in order to be able to interpret the data. In addition to roughness, relaxation or reconstruction of the top atomic layer(s) can also effect the CTR intensity. What will be shown in the following sections is that it is unlikely that either relaxation or reconstruction are present at the interface of the thermally oxidized wafers used in this study. The scattering data that will be

presented in Chapters 4 and 5 will have a decrease in intensity away from the Bragg reflection which is symmetric for both the (202) and (311) rod. This would not be the case if either relaxation or reconstruction was present at the interface. The influence of miscut on the CTR scattering is treated separately in Chapter 5.

Because CTR's arise due to the termination of the bulk lattice, neither vacuum nor an amorphous film affects the shapes the shape of the CTR scattering. Therefore, one can explicitly isolate the scattering due to the substrate-film interface by measuring the truncation rod from a reflection whose scattering vector is inclined with respect to the surface normal. In contrast, if the bulk crystal is covered by a crystalline film, then the truncation rods may be modified by scattering from periodicities in the overlayer which have the same direction as the substrate reflection [19, 41].

2.4.1 Relaxation

Relaxation of the top atomic layer (either expansion or contraction) results in asymmetry of the rod profile [42]. Various models can be considered such as one where several layers will have a gradually different lattice parameter out-of plane compared with the bulk, or only the outermost layer is relaxed. For simplicity consider the effect of a constant displacement of a single layer, where the atoms are shifted with respect to the usual lattice sites along the surface normal by Δ. The structure factor for the crystal is given by the sum of the structure factor from the bulk crystal as derived in Eqn. 2.16 and the structure factor of the relaxed atomic layer:

$$\begin{aligned} F &= F_{DC} + F_{relax} \\ &= F_{DC} + f_0 e^{-2\pi i l\Delta} \sum_{j_1=0}^{N_1-1} e^{2\pi i h j_1} \sum_{j_2=0}^{N_2-1} e^{2\pi i k j_2} \\ &= f_0 \left(\frac{e^{2\pi i h N_1} - 1}{e^{2\pi i h} - 1} \right) \left(\frac{e^{2\pi i k N_2} - 1}{e^{2\pi i k} - 1} \right) * \\ &\quad \left((1 + e^{\pi i (k - \frac{l}{2})})(1 + e^{\pi i (h+k-l)}) \left(\frac{e^{2\pi i l N_3} - 1}{e^{2\pi i l} - 1} \right) + e^{-2\pi i l \Delta} \right), \end{aligned} \tag{2.18}$$

where Δ is the expansion of the top layer in reciprocal lattice units. Any displacement of the top layer normal to the surface results in asymmetry in the intensity from

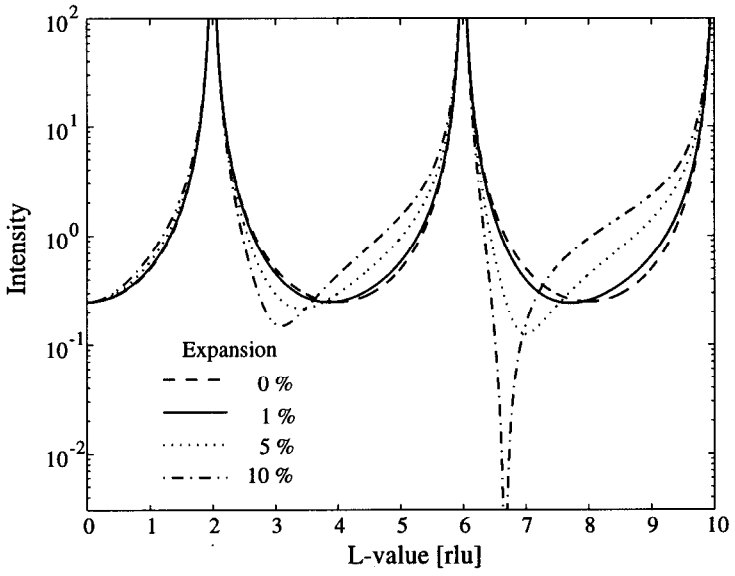

Figure 2.5: $20l$ CTR intensity for a perfectly flat diamond cubic crystal calculated using the layer summation method. The three curves correspond to an increasing degree of expansion of the top layer.

all Bragg reflections. The asymmetry is more pronounced for higher order Bragg reflections, as shown in Figure 2.5, where the CTR intensity has been plotted for the $20l$ rod for a Si(001) crystal with no roughness. The angle between the surface of the crystal and the scattering vector is larger for higher order Bragg reflections, and the scattering vector is consequently probing structures more perpendicular to the surface. Thus the sensitivity to an out-of plane d-spacing change is larger at higher l-values.

A contraction of the surface layers causes the asymmetric effect to be reversed, so that the low side of a Bragg reflection has a slower fall off in intensity than the high side of the reflection.

2.4.2 Reconstruction

For native oxides there is experimental evidence for a partial 2×1 reconstruction of the Si-SiO_2 interface [6, 10]. Although there is no indication that this should be

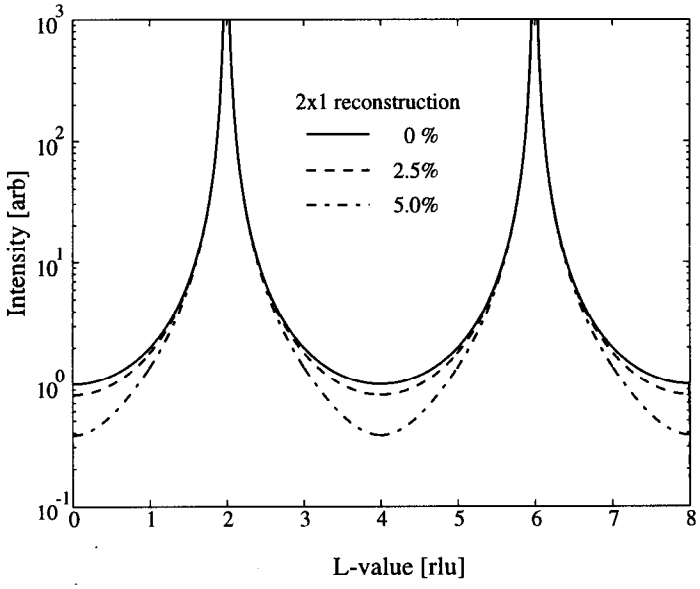

Figure 2.6: $20l$ CTR intensity for a perfectly flat diamond cubic crystal with a reconstruction of the top layer calculated using the layer summation method. The three curves correspond to an increasing degree of dimerization.

the case for a thermally grown oxide, the effect of a reconstructed surface, i.e. the rearrangement of atoms in the plane of the surface, is worth exploring.

The dimerization of the top layer for a 2×1 reconstruction will always occur in the direction perpendicular to the bonds, so that the A-atoms (see Figure 2.4) will translate in the [100]-direction whereas the B-atoms will translate in the [010]-direction. For simplicity consider a perfectly flat crystal terminated by a reconstructed A-plane. To account for this reconstruction it is necessary to have a basis of two unit cells, since alternate row of atoms are translated along the positive or negative [100] direction. A sum over the diamond cubic lattice of silicon using two unit cells in the [100] directions is given by:

$$\begin{aligned} F_{DC-2} &= f_0(1+e^{\pi i(k-\frac{l}{2})})(1+e^{\pi i(h+k-l)})(1+e^{2\pi ih})* \\ &\left(\frac{e^{2\pi ihN_1}-1}{e^{4\pi ih}-1}\right)\left(\frac{e^{2\pi ikN_2}-1}{e^{2\pi ik}-1}\right)\left(\frac{e^{2\pi ilN_3}-1}{e^{2\pi il}-1}\right) \end{aligned} \tag{2.19}$$

Analogously to relaxation, the structure factor of a reconstructed crystal is given by

the sum of a doubled diamond cubic lattice and that of the reconstructed surface layer:

$$\begin{aligned} F &= F_{DC-2} + F_{recon} \\ &= F_{DC-2} + f_0(e^{2\pi ih\Delta} + e^{2\pi ih(2-\Delta)}) \sum_{j_1=0}^{N_1/2-1} e^{4\pi ihj_1} \sum_{j_2=0}^{N_2-1} e^{2\pi ikj_2} \\ &= f_0 \left(\frac{e^{2\pi ihN_1}-1}{e^{4\pi ih}-1}\right)\left(\frac{e^{2\pi ikN_2}-1}{e^{2\pi ik}-1}\right)\left(e^{2\pi ih\Delta} + e^{2\pi ih(2-\Delta)} + \right. \\ &\quad \left. (1+e^{\pi i(k-\frac{l}{2})})(1+e^{\pi i(h+k-l)})(1+e^{2\pi ih})\left(\frac{e^{2\pi ilN_3}-1}{e^{2\pi il}-1}\right)\right). \end{aligned} \tag{2.20}$$

Figure 2.6 shows the $20l$ rod intensity calculated for a silicon(001) wafer with no roughness. Reconstruction of the top layer causes a decrease in the scattered intensity, which is also the case if roughness is present, as will be discussed in the section following this. The picture is very different for the $31l$ rod intensity as shown in Figure 2.7. In order to exclude any crystal structure effects, the scattered intensity was averaged over domains with different crystal termination. Thus, the $31l$ rod is symmetric about the Bragg peaks when there is no reconstruction, but as the degree of dimerisation increases so does the rod asymmetry. The same is true for all other rods which are not along a $< 100 >_{bulk}$ direction.

2.4.3 Roughness

The influence on the CTR scattering when roughness is present is shown below for the two models (continuum and atomistic). A modified theory is presented with experimental results in Chapter 4.

Continuum Model

A simple model for a rough surface is one where the distribution of heights above and below some mean value can be described by a Gaussian function. The rms roughness σ is given by the standard deviation of this distribution of heights. This assumption is appropriate if the scattering is averaged over a large surface area of random roughness.

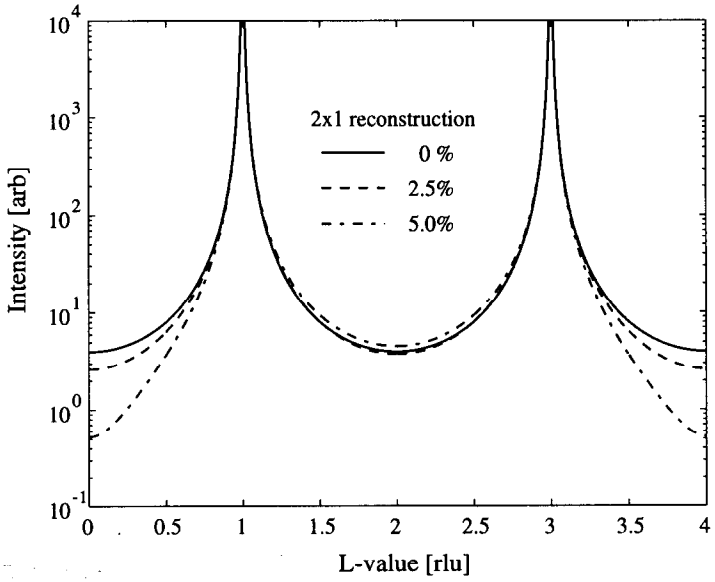

Figure 2.7: $31l$ CTR intensity for a perfectly flat diamond cubic crystal with a reconstruction of the top layer calculated using the layer summation method. The three curves correspond to an increasing degree of dimerization.

The electron density in a one-dimensional model with a Gaussian interface can be described via the complementary error function:

$$\rho(z) = \frac{1}{2}\rho_0 erfc\left(\frac{z}{\sqrt{2}\sigma}\right). \tag{2.21}$$

The electron density of the crystal can then be described by the above equation multiplied by delta-functions at the atomic positions of an infinite lattice. The complimentary error function is essentially a Gaussian convoluted with a Heaviside function. Fourier transformation of the complimentary error function is thus given by the Fourier transform of a Gaussian multiplied by the Fourier transform of the Heaviside function. A Gaussian with an interface width σ is given by:

$$f(z) = \exp(-\frac{z^2}{2\sigma^2}), \tag{2.22}$$

for which the Fourier transform is:

$$F(q_\perp) = \sigma\sqrt{2\pi}\exp(-\frac{\sigma^2 q_\perp^2}{2}). \tag{2.23}$$

The Fourier transform of the Heaviside function is given by:

$$F(q_\perp) = \frac{i}{2\pi q_\perp} - \frac{1}{2}\delta(q_\perp) = \frac{i}{2\pi q_\perp}. \tag{2.24}$$

The intensity, which is convoluted onto every reflection in reciprocal space is thus proportional to:

$$I(\vec{q}_\perp) \propto \sum_{\vec{\tau}} \frac{|\rho_0(\vec{\tau})|^2}{q_\perp^2} \exp(-\sigma^2 q_\perp^2). \tag{2.25}$$

The damping term arising from the Gaussian interface causes a faster decay of the scattered intensity away from the Bragg reflection. Roughness causes some of the photons to be scattered in other directions. This is known as diffuse scattering. It is this scattering which is now "missing" from the rod. Roughness can also be characterized by the number of Fourier components which are needed to describe the change in electron density. A perfectly flat surface or interface requires many Fourier components, which extends the Bragg peak in the direction of the surface. A rough surface can be modelled by fewer Fourier components and thus the intensity decays more quickly. Figure 2.8 shows the CTR intensity in the vicinity of a single Bragg peak. Unlike reconstruction and relaxation of the surface layer, roughness causes a symmetric decay of scattering on both sides of the Bragg peak. The larger the roughness, the faster the decay of intensity. The exponential decay of scattering away from a Bragg peak causes the intensity far from a Bragg peak to vanish, so only the intensity close to the rod is shown in the figure.

Atomistic model

Roughness is introduced in the layer summation method by adding layers with partial occupancy to the surface of a semi-infinite crystal. Each atomic layer added to the crystal is filled by the fraction β^{-j}, where β is the roughness parameter and j is numbering of the layer above the semi-infinite crystal. Robinson assumes a fractional occupancy at each atomic site in this model. In order to be consistent with the derivations in section 2.2.2, j is a negative number starting at zero for the first layer added to the flat crystal. Note that the roughness used in this model is not Gaussian. Instead the termination of the crystal follows a power-law decrease in the fractional

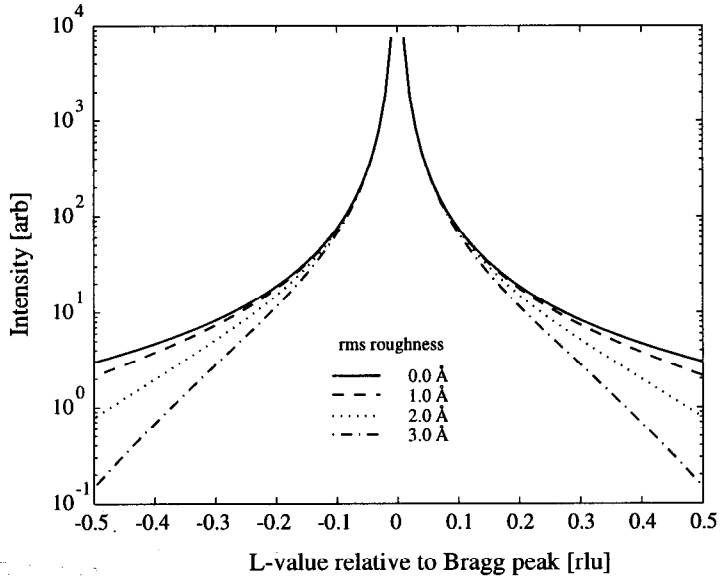

Figure 2.8: CTR intensity for crystals with various surface roughnesses calculated using the continuum model. An increase in surface roughness causes a faster decay of intensity away from the Bragg reflection.

occupacy of the surface layers, which corresponds to a very asymmetric interface. The roughness parameter can be related to the rms roughness σ by:

$$\sigma_{rms} = \frac{\sqrt{\beta}}{1-\beta} d_{\perp} \tag{2.26}$$

where $d_{\perp}$ represents the atomic distance perpendicular to the surface. The intensity for a simple cubic crystal terminated by a rough surface in the [001] direction is [17]:

$$\begin{aligned} I &= N_1^2 N_2^2 \left| \sum_{j=-\infty}^{0} \beta^{-j} e^{2\pi i l j} + \sum_{j=1}^{\infty} e^{2\pi i l j} \right|^2 \\ &\rightarrow N_1^2 N_2^2 \frac{(1-\beta)^2}{1+\beta^2-2\beta\cos(2\pi l)} * \frac{1}{4\sin^2(\pi l)} \end{aligned} \tag{2.27}$$

For the silicon(001) surface the occupancy of the layers needs to be assigned to the A and B-layers separately. The term for summing up over all the A layers is:

$$F_A = f_0 \sum_{j=0}^{-\infty} (\beta^3 + \beta e^{\pi i (h+k-l)}) \beta^{-4j} e^{2\pi i l j} = f_0 \frac{\beta^3 + \beta e^{\pi i (h+k-l)}}{1-\beta^{-4} e^{2\pi i l}} \tag{2.28}$$

Summing up over all the B layers yields:

$$F_B = f_0 \sum_{j=0}^{-\infty} (\beta^2 + e^{\pi i(h+k-l)}) e^{\pi i(h-\frac{l}{2})} \beta^{-4j} e^{2\pi i l j} = f_0 \frac{(\beta^2 + e^{\pi i(h+k-l)}) e^{\pi i(h-\frac{l}{2})}}{1 - \beta^{-4} e^{2\pi i l}} \quad (2.29)$$

Therefore, the structure factor from a rough silicon crystal is given by adding up the structure factor of the semi-infinite crystal (Eqn. 2.16) and that of the partial layers:

$$\begin{aligned} F_{DC-rough} &= F_{DC} + F_{rough} \\ &= F_{DC} + (F_A + F_B) \sum_{j_1=0}^{N_1-1} e^{2\pi i h j_1} \sum_{j_2=0}^{N_2-1} e^{2\pi i k j_2} \\ &= f_0 \left(\frac{e^{2\pi i h N_1} - 1}{e^{2\pi i h} - 1} \right) \left(\frac{e^{2\pi i k N_2} - 1}{e^{2\pi i k} - 1} \right) * \\ &\quad \left((1 + e^{\pi i(k-\frac{l}{2})})(1 + e^{\pi i(h+k-l)}) \left(\frac{e^{2\pi i l N_3} - 1}{e^{2\pi i l} - 1} \right) + \right. \\ &\quad \left. (\beta + e^{\pi i(h-\frac{l}{2})})(\beta^2 + e^{\pi i(h+k-l)}) \frac{1}{1 - \beta^{-4} e^{2\pi i l}} \right) \end{aligned} \quad (2.30)$$

Based on this equation, the intensity is calculated along the rod and shown in Figure 2.9. The $20l$ rod is shown for different rough silicon surfaces. As in the continuum model, the decay of the scattering is symmetric about the Bragg reflection, with a faster decay of intensity for rougher surfaces.

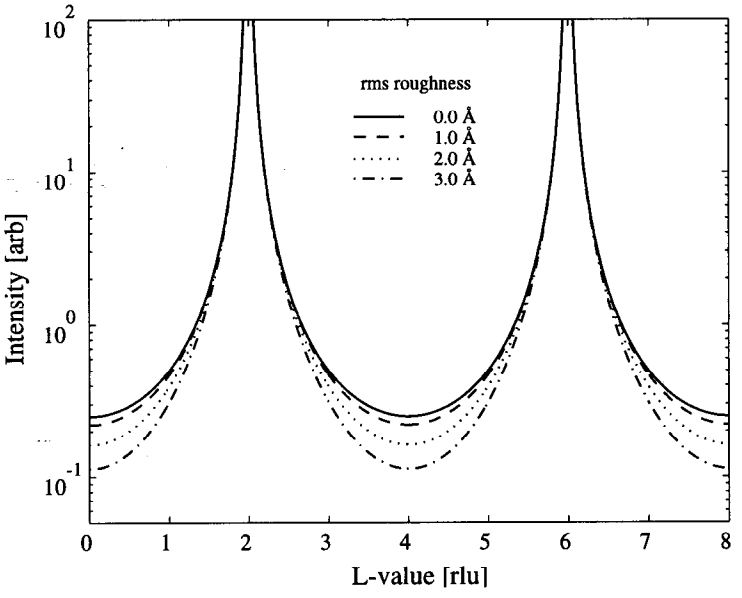

Figure 2.9: $20l$ rod of silicon(001) with various surface roughnesses calculated using the layer summation method. As the roughness of the surface increases, the intensity between the Bragg reflections decreases.

Chapter 3

Experimental Procedures

Summary

Experiments were performed at Stanford Synchrotron Radiation Laboratory (SSRL) on beam lines 6-2, 7-2 and 10-2. This chapter will briefly review the production of synchrotron radiation followed by a description of the beam line components with an emphasis on the x-ray optics of beam line 7-2. The diffraction geometry is explained along with scans used for data collection in these experiments. Finally the slit setting and its influence on crystal truncation rod scattering is discussed.

3.1 Synchrotron Radiation

Synchrotron radiation is much more intense than the radiation produced by conventional X-ray sources. The spectrum of x-rays emitted by a synchrotron source is continuous from the visible out to an energy which is related to the energy of the circulating electrons and the bending radius of the magnets in the electron path. A monochromator is used to select a particular wavelength for an experiment (although some experiments use the white beam). Due to the small divergence of the synchrotron source (~0.1 mrad) and the small source size (~2 mm^2), the brightness of the synchrotron (photons/sec/mA/mrad^2/mm^2/0.1% BW) is typically 6-7 orders of magnitude larger than that of a conventional x-ray source. It is this increased brightness which enables the experiments described in this thesis to be done.

3.1.1 Source Characteristics

The source of beam line 7-2 is an 8-pole, 1.8 T electromagnetic wiggler consisting of 4 periods of 45.0 cm. The alternating magnetic field of the insertion device forces the electrons to oscillate in an otherwise straight section of the electron orbit. Radiation produced by each wiggle adds up incoherently to yield a higher flux than that obtainable by a bending magnet. The device critical energy E_c=10,775 eV ($E_c = 0.665 E_{ring}^2[GeV] B_o[T]$ [43]) corresponds to the energy which divides the white beam power spectrum in half. The flux as a function of photon energy is plotted in Figure 3.1 integrated over the vertical divergence for a ring current of 100 mA. The opening angle in the vertical plane is approximately given by $1/\gamma$ which is a function of the electron energy in the ring:

$$1/\gamma = \frac{m_e c^2}{E_{ring}} = \frac{0.511\ MeV}{3\ GeV} = 0.17\ mrad \tag{3.1}$$

where the ring energy corresponds to that of SPEAR.

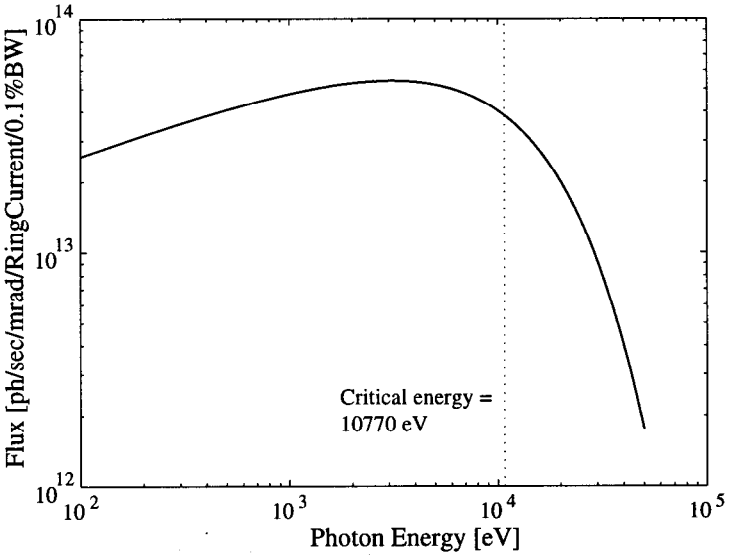

Figure 3.1: Flux vs. Photon Energy produced by the beam line 7-2, 1.8 T 8-pole wiggler at SPEAR. The critical energy at 10.77 keV is shown as the dashed vertical line.

3.1.2 Aperture

Slits positioned before the mirror are designed to cut down both the horizontal and vertical divergence. Inserting the slits reduces the heat load on the rest of the optical components in the beam down stream. The vertical aperture, which is just upstream of the mirror, consists of 3 openings in a mask, which allows an angular acceptance of 64.5 μrad, 129 μrad or 252 μrad. The horizontal aperture is defined by a vee slit of 70 degrees, which allows the user to select a continuous range of angles from 0-4 mrad in the horizontal plane. A schematic is shown in Figure 3.2. In these experiments a horizontal acceptance of 1 mrad and a vertical acceptance of 129 μrad was used. Due to the energy dependence of the opening angle of the photons, the vertical slit is more effective at reducing the long wavelength photons.

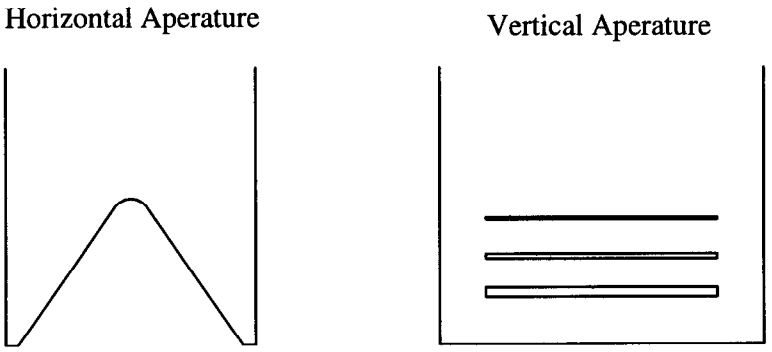

Figure 3.2: Horizontal and vertical aperture for beam line 7-2. The vertical aperture is placed 12.6 m from the source, whereas the horizontal aperature is 12.7 m from the source. Both are just upstream of the focusing mirror.

3.2 X-ray Optics

3.2.1 Mirror

One can show using Snell's law that, for materials with an index of refraction less than 1, there is an incidence angle below which x-rays of wavelength λ are almost totally reflected. If one ignores the energy dependence of the index of refraction, this angle, known as the critical angle, is defined by:

$$\alpha_c = \lambda\sqrt{\frac{r_e\rho_e}{\pi}} \tag{3.2}$$

where λ is the wavelength, ρ_e is the average electron density of the material, and r_e the classical electron radius. A more accurate definition of the critical angle would include the effects of anomalous scattering and turn ρ_e into an effective $\rho_e(\lambda)$. For angles of incidence below α_c there is still an evanescent wave field in the material and the reflectivity can never be 100% since real materials absorb. Since the critical angle for total external refraction is inversely proportional to the energy of the photons, for a given angle of incidence on the material there is a photon energy above which the photons penetrate rather than being reflected. In analogy with the critical angle α_c this energy is known as the critical energy E_c. Because the critical angle (and critical energy) are proportional to the square root of the electron density of the material, dense materials such as platinum are used as reflecting surfaces. Absorption edges of

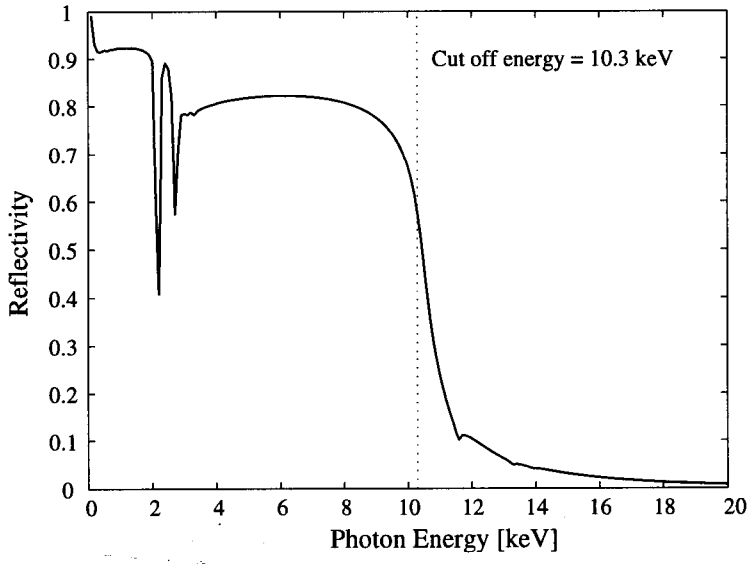

Figure 3.3: Normalized reflectivity for Platinum for an angle of incidence of 7.7 mrad (0.44 degrees). The cut off energy at 10.3 keV is shown as the dashed line. The sharp dips in the reflectivity at low energies are due to the change in index of refraction at the M and L-edges.

the mirror coating will cause the reflectivity to drop further at those energies primarily due to the change in f', the real part of the change in the electron scattering factor. For platinum the L edges are at 11.564 keV, 13.273 keV and 13.880 keV and the M-edges range from 2.122-3.296 keV. Figure 3.3 is the calculated normalized reflectivity shown as a function of photon energy for an angle of incidence of 7.7 mrad (0.44 deg) corresponding to the 7-2 mirror.

Mirrors can be made to either collimate or focus the beam. Due to the above described properties, the mirror also serves for cutting off higher energies (low pass filter) to minimize the power on the first monochromator crystal. The 7-2 mirror is a 1/2 degree angle of incidence fused silica bent cylinder coated with platinum (1000 Å). The reflected beam rises at ~1 degree with respect to the plane of the electron orbit in SPEAR. An ellipsoidal mirror would be ideal for focusing the beam, but it is difficult to produce for these wavelengths. Since the radius in the beam direction is rather large (10e5 cm), bending a cylinder is more practical and the meridional

focal length is tunable by changing the bend. A cylinder will mainly focus the beam horizontally. The radii of the 7-2 mirror are 10 cm by 1650 m with a cutoff photon energy of 10.3 keV. The maximum horizontal acceptance is 4.6 mrad. The length of the mirror is 580 mm. The angle of incidence was chosen such that the critical energy is close to the platinum L-edge energies to more sharply curtail the decrease in reflectivity above the critical energy.

3.2.2 Monochromator

The monochromator selects the wavelength from the continuous synchrotron radiation spectrum. Depending on the experimental requirements the monochromator can be chosen to optimize some, but not all, of the following features: the energy resolution, a wide tunable wavelength range, high transmitted intensity, resistance to heat and radiation and absence of higher order harmonics. For these experiments an upward reflecting water-cooled non-dispersive double crystal Si(111) monochromator was used, which is commonly used at SSRL for x-ray diffraction experiments. This non-dispersive monochromator is also called the minus setting or (+1,-1) since it consists of 2 single crystals, the first one reflecting upward and the second downward, a schematic of which is shown in Figure 3.4. Diffraction from atomic planes in a crystal which are separated by a distance d is allowed when the wavelength λ of the photons match the incident angle θ according to Bragg's law [38, 44, 45]:

$$\lambda = 2d \sin\theta \tag{3.3}$$

The same symmetric reflection is used in both crystals so that the incident and outgoing angle is constant for the two crystals. For these symmetrically cut crystals the diffracting planes are parallel with the surface of the crystal in the Bragg case (reflection rather than transmission), and the incident angle therefore equals the outgoing angle. The energy is chosen by rotating the two crystals with respect to the beam so that the Bragg angle θ changes. The advantage of this setting is that there is no angular deflection of the outgoing beam, however there is a vertical translation of the beam when the energy is scanned.

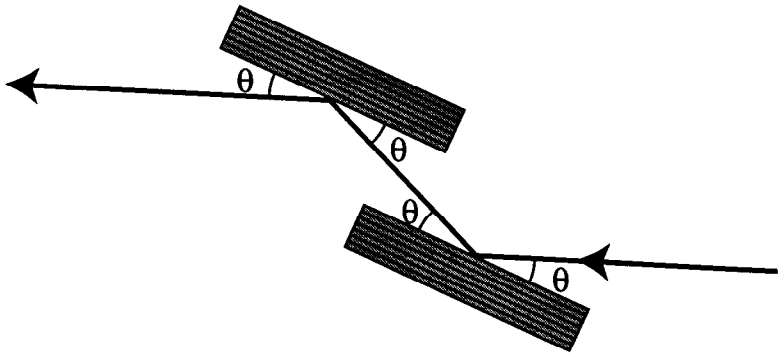

Figure 3.4: Schematic of a non-dispersive (+1,-1) monochromator. This double crystal setting ensures that there is no angular deflection of the beam.

3.3 Components in the Hutch

3.3.1 Diffractometer

A standard 4-circle diffractometer is placed inside the hutch. The diffractometer can rotate the sample about three perpendicular axes θ, χ and ϕ (using the notation of Busing and Levy [46]). A schematic of the angular relationship is shown in Figure 3.5. The θ axis, which lies in the horizontal plane perpendicular to the direction of the incident beam, is also called the instrument axis. The detector rotates about this axis at an angle 2θ with respect to the incident beam. However since the sample and the detector can rotate independently, the rotation of the sample is not necessarily half that of the detector rotation. This offset angle is called ω. The scattering plane is defined by the incident and diffracted beam, i.e. perpendicular to the θ axis. The χ axis, which lies in the scattering plane, makes an angle $\theta + \omega$ with the incident beam. The χ axis is defined as right handed, whereas the θ and ϕ axes are both left handed. Angle positions are controlled via the software SUPER [47, 48], which also controls the energy selected by the monochromator, table translations, etc. Since the motion of the sample around the instrument axis is controlled by a single motor the sum of the angles ω and θ is called Theta within SUPER, i.e. Theta $= \theta + \omega$.

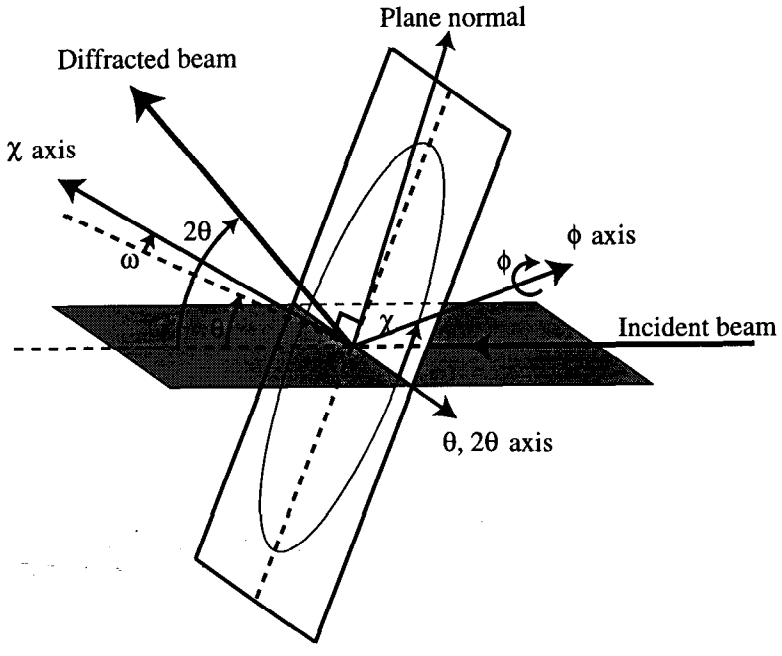

Figure 3.5: Schematic showing the 4-circle diffractometer with a vertical scattering geometry and the definitions of the angles according to Busing and Levy [46]. The axis labelled by θ and 2θ is the instrument axis.

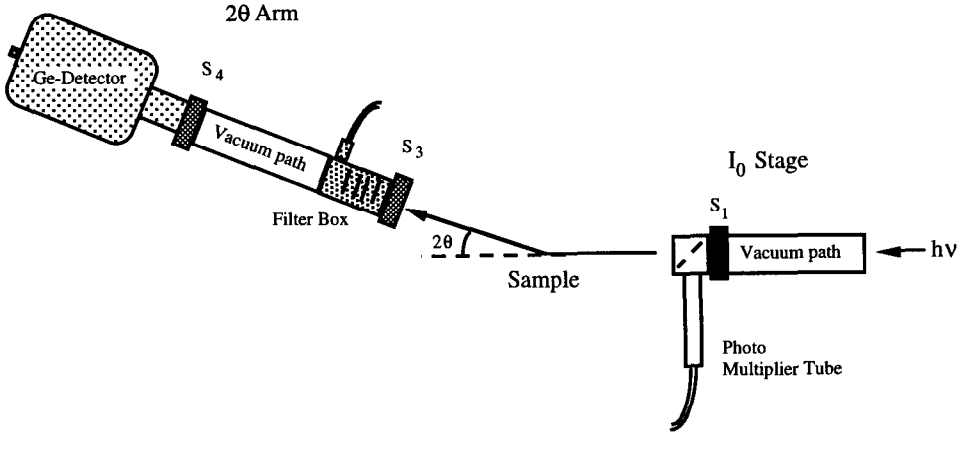

Figure 3.6: Schematic of the components in the hutch.

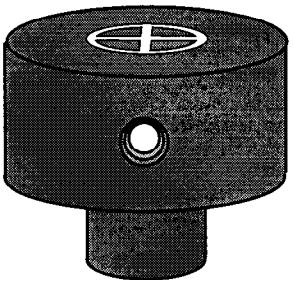

Figure 3.7: Schematic of the aluminum vacuum chuck used for mounting the wafers on the goniometer.

3.3.2 Sample Mount

The sample is positioned on a goniometer in the center of the diffractometer as shown in Figure 3.6. The sample surface normal is aligned with the ϕ-axis using the procedure given in the manual for SUPER [48]. For easy sample changing a vacuum chuck as shown in Figure 3.7 was used, which was made after a design by T. Rabedeau of the SSRL staff. The wafer is contained in a helium environment although the diffraction experiments conducted in this thesis are high angle scattering and thus air scattering into the detector is not critical. However, the low density of helium reduces absorption.

3.3.3 I_0 Stage

The I_0 stage corresponds to the components upstream of the diffractometer in the hutch, which are all placed on a vertical translation table. A slit (S_1) is positioned 25 cm upstream of the diffractometer defining the beam size on the sample. Upstream of the slit is a vacuum path which reduces absorption. Downstream of the slit is a kapton film positioned at an angle of 45° with respect to beam. A small part of the photons scatter off the kapton and into a photo multiplier tube (PMT), which is mounted at a 90° to the beam as indicated in Figure 3.6. This detector monitors the incident beam flux (hence called the "Monitor"). Changes in the incident flux are measured for normalizing purposes.

The flightpath on the 2θ arm has a slit (S3) positioned close to the sample, which

is a scatter slit. The defining slit (S4) is placed in front of the germanium detector.

3.3.4 Detector

A Germanium solid-state detector was used for the experiments in this thesis. An incident photon on the detector creates electron-hole pairs, the number of which is proportional to the photon energy. Since the photon energy is proportional to the detector signal an electronic window is set around the elastic peak in order to filter out any higher harmonics. Thus, for instance, photons with three times the desired energy passed by the (333) monochromator reflection are not counted. When cooled with liquid nitrogen the Ge-detector is very good for low count rate experiments. However the detector goes non-linear for high count rates limiting the maximum count rate to ~5000 photons per second.

3.3.5 Absorbers

The flux into the detector is controlled by inserting filters in the beam path. Four filters are mounted on the 2θ arm 50 cm from the sample. These absorbers, which are controlled by pneumatics, can be inserted manually or be controlled by SUPER. Molybdenum filters of thickness 25 μm, 50 μm, 100 μm and 200 μm worked well for 10 keV photons. The absorption length of Mo at 10 keV is 11.6 μm which for this filter setup corresponds to a beam attenuation of 1.16e-1,1.35e-2,1.82e-4, 3.31e-8, respectively. Calibration of the absorbers is done by measuring the transmitted intensity for the same incident flux using different filter combinations. Molybdenum was chosen over aluminum for the filter material, since it is more efficient at absorbing the higher harmonics passed by the monochromator due to its K-absorption edge of 20 keV.

3.3.6 Slits

Slits positioned before and after the sample define the beam trajectory. The incident beam size is defined by the S_1 slit, which determines the beam size on the sample.

	Horizontal	Vertical
S_1	250 μm	1 mm
S_2	1 mm	4 mm
S_3	1 mm	4 mm

Table 3.1: Typical slit setting for CTR scattering experiments.

By positioning the S_1 slit close to the sample, the beam size will only change slightly before hitting the sample. The S_3 slit, which is placed close to the sample on the 2θ arm, prevents non-useful photons from entering the flight path. S_4, the angle defining slit, is positioned next to the detector at a distance of ~600 mm from the center of the diffractometer. In diffraction experiments such as x-ray reflectivity a narrow slit is used in the direction of the scattering vector to achieve good resolution, however the slit is relatively wide in the direction perpendicular to the scattering vector to get high flux. In CTR scattering the rod rotates with respect to the instrument as the rod is being scanned, so a similar approach cannot be used. Instead the slit scheme described by Specht & Walker [49] is used, which is designed for CTR scattering experiments. By employing relatively large slits all of the diffracted beam is collected by the detector without moving the sample for both large perpendicular and parallel momentum transfer. This will be discussed further in section 3.6. A typical slit setting is given in Table 3.1

3.4 Alignment

3.4.1 Alignment of a Single Crystal

The orientation of a single crystal can be established when two independent crystallographic directions and the unit cell parameters are known. The software SUPER [48], which is used to control the motion of the diffractometer, can also calculate an angular setting for a given reflection when the photon energy, two reflections and the unit cell have been given [46]. The four-circle diffractometer has an extra degree of freedom which allows the same reflection to be reached by an unlimited number

of angle settings corresponding to different angles of rotation of the sample about the scattering vector. Several modes can be chosen which constrain the selection of diffractometer angles to certain criteria. This work was primarily done in the "ω=0" mode, which keeps θ at half the value of 2θ and thus ensures that the incident (α) and outgoing (β) angles onto the surface are equal. In order to align a single crystal with respect to a diffractometer two reflections of the crystal need to be found, called the primary and secondary reflections. These are typically chosen to be along major orthogonal directions. In the case of Si(001) wafers the [001] direction is close to that of the surface normal and the $< 110 >$ type directions are in the surface plane of the wafer indicated by either one or two flats along the wafer edge. In the case where a wafer is mounted on the goniometer with its surface normal aligned along the ϕ-axis and the incident beam along a flat an initial orientation matrix would be:

	H	K	L	OMEGA	CHI	PHI
Primary:	0.0000	0.0000	4.0000	0.000	90.000	0.000
Secondary:	2.0000	2.0000	0.0000	0.000	0.000	0.000

H,K and L correspond to the indices of the reflection and Omega, Chi and Phi to the angular setting associated with that reflection. Note that Omega is defined as the difference between θ and half of 2θ (Omega $= \theta - 2\theta/2$). This matrix is only approximate and the exact angular positions of the two reflections need to be determined experimentally. Alignment of a single crystal is most easily done by finding a reflection along the surface normal, as it can be measured independently of the ϕ-rotation of the sample. In the case of a Si(001) wafer the (004) reflection is used for the initial alignment since it is easy to find at any value of ϕ and it is also used for the energy calibration (see below). Its angular position is determined by sequential scans of the θ and χ motor, keeping ϕ constant. For aligning the crystal, an asymmetric reflection needs to be found as well, e.g. the (111),(202) or (311) reflection. The position of an asymmetric reflection is determined by sequential scans of the χ and ϕ motor keeping θ at half the value of 2θ. The angular positions are then put into SUPER in a similar manner as shown above. An orientation matrix is calculated, based on these two

reflections and the unit cell parameters, which translates a reciprocal lattice vector into the angle space of the diffractometer and vice versa. Note that the primary reflection is fixed, so that the calculated angles for that reflection after refinement of the transformation matrix corresponds exactly to the those found experimentally. However, generally this is not true for the secondary reflection, because the transformation matrix needs to be consistent with the given unit cell. The primary reflection is used to fix the orientation, whereas the secondary reflection determines the rotation of the crystal about this direction. Therefore, the crystal orientation is most accurate close to the defined primary reflection. Thus, for crystal truncation rod scattering one should define the Bragg peak of the rod one wants to measure as the primary reflection and the secondary reflection as an asymmetric reflection close by, e.g. for the (202) rod use (202) as the primary and (311) as the secondary reflection.

3.4.2 Calibration of the Photon Energy

The energy of the photons passed by the monochromator is initially calibrated with respect to an absorption edge such as the copper K-edge. Improving the accuracy of the energy can be achieved by measuring the angular position of two Bragg reflections. In fact, such a measurement not only yields the photon energy but also any offset in the θ value. The section above describing how to align a single crystal with respect to the diffractometer assumes that the photon energy is known. However this procedure only causes the scattering vector to be aligned with the plane normal without ensuring that the length of the scattering vector matches that of the plane spacing. The length of the scattering vector is changed by scanning 2θ, which is done after finding an out-of-plane reflection (e.g. Si(004)). Iterative scans of 2θ, θ and χ with a repositioning of the motor to the maximum of the scan will yield the angular position of the reflection. Using the same procedure to determine the angular position of another out-of-plane reflection will give two sets of angles (θ_1 and θ_2) for two different d-spacings (d_1 and d_2) along the same crystallographic direction. Although the Si(002) is not bulk-allowed there is enough scattered intensity to use it for calibration. Two equations with two

unknowns can be derived from Bragg's law:

$$\begin{aligned} \lambda &= 2d_1 \sin(\theta_1 + d\theta) \\ \lambda &= 2d_2 \sin(\theta_2 + d\theta) \end{aligned} \tag{3.4}$$

where λ is the x-ray wavelength and $d\theta$ is the offset in θ. This offset is a combination of a true offset of the θ value combined with any miscut of the sample in the beam direction. The photon energy ($E = hc/\lambda$) can be derived numerically along with $d\theta$ from these equations and is implemented in SUPER.

3.5 Samples

The samples used in this thesis were all 6 inch Silicon(001) industry production wafers. Wafers terminated by both native and thermal oxides were investigated as well as the influence of various cleaning procedures prior to oxidation. The specifics of the sample preparation will be given in Chapters 4 and 5.

3.6 Scattering Geometry

The scattering geometry for CTR scattering is shown in Figure 3.8. $\vec{k}_i$ and $\vec{k}_o$ corresponds to the incoming and outgoing k-vectors onto the sample and $\vec{Q}$ is the resulting scattering vector ($\vec{Q} = \vec{k}_o$ - $\vec{k}_i$). The incident and outgoing angles are kept constant using the "omega=0" mode.

3.6.1 Footprint on the Sample

As discussed in the theory section, crystal truncation rod scattering is sensitive to the surface structure. Therefore, the diffracted intensity along the rod needs to be corrected for any changes in the area on the sample from which the x-rays scatter. Since the angular setting of the diffractometer changes as a rod is being scanned, the sample area illuminated by the beam also changes. The footprint on the sample is defined by the incident slit and the angles χ and θ of the diffractometer. Assuming

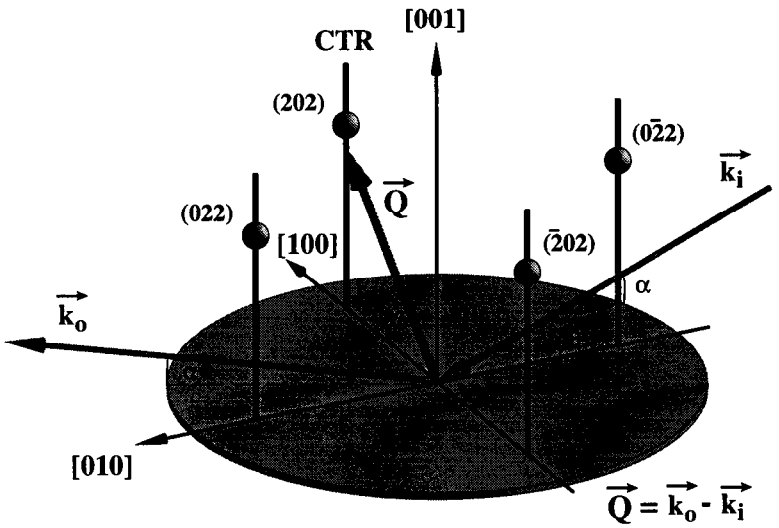

Figure 3.8: Crystal truncation rod scattering geometry for a Si(001) wafer. Using the "omega=0" mode, the incident and outgoing angles stays constant.

a perfectly collimated beam through a rectangular incident slit ($S1_{vert} \times S1_{horz}$) the footprint on the sample is a parallelogram as shown in Figure 3.9a. There are two limiting cases which determine the width of the footprint. At large angles of χ the horizontal slit size limits the width, whereas for small χ values, it is the vertical slit size which limits the footprint width. In general, the width of the footprint is given by:

$$\frac{S1_{vert}}{\cos\chi} \quad , \chi \leq \chi_{crit} \tag{3.5}$$

$$\frac{S1_{horz}}{\sin\chi} \quad , \chi > \chi_{crit}, \tag{3.6}$$

where χ_{crit} defines the transition from this transition:

$$\tan\chi_{crit} = \frac{S1_{horz}}{S1_{vert}} \tag{3.7}$$

which in the case of the our slit setting (see Table 3.1) corresponds to a χ_{crit} of 14.04 degrees. For the rod associated with the (202) reflection χ is larger than this critical value, however for the (311) rod at l-values less than 0.8, it is the vertical size of S_1 which limits the width of the spot size on the sample. Note, that the maximum width of the footprint (which occurs at $\chi = \chi_{crit}$) is given by $\sqrt{S1_{horz}^2 + S1_{vert}^2}$.

With the slit setting according to Table 3.1 this corresponds to 1.03 mm. The actual footprint width is given in Table 3.2 for the (202) and (311) rod of Si(001) using 10 keV photons. The length of the footprint on the sample (in the scattering direction) is a function of both θ and χ:

$$\frac{2S1_{vert}}{\sin\theta} \quad ,\chi \leq \chi_{crit} \tag{3.8}$$

$$\frac{S1_{vert}}{\sin\theta} + \frac{S1_{horz}}{\sin\theta\tan\chi} \quad ,\chi > \chi_{crit}. \tag{3.9}$$

There are two components to the length of the footprint. Consider the situation where χ=90 degrees, then the footprint on the sample is a rectangle, the length of which depends on the rotation of θ. A rotation in χ will not change the length, however it will skew the footprint so that it becomes a parallelogram. In the equations above the length does depend on the χ rotation, however the length calculated is the total length of the footprint, not the length at a specific point along the width. It is this total width that needs to be considered when evaluation if the sample is large enough to collect the entire beam. These lengths, which change from 4.67 mm to 3.28 mm for the (202) rod, are given in Table 3.2. In general, the samples examined in these studies are 6 inch wafers. Although keeping the beam on these samples is not a problem, the illuminated area on the sample needs to be known for data correction purposes. However, it is also informative to know the area of the sample from which the roughness is deduced. This area can be expressed in general terms as:

$$\frac{S1_{vert}^2}{\sin\theta\cos\chi} \quad ,\chi \leq \chi_{crit} \tag{3.10}$$

$$\frac{S1_{vert}S1_{horz}}{\sin\theta\sin\chi} \quad ,\chi > \chi_{crit} \tag{3.11}$$

For these experiments the area is 0.9-1.5 mm^2 for the (202) rod and 1.5mm-2.8 mm^2 for the (311) rod. Note that the rms roughness obtained from CTR scattering does not include roughness on these length scales as is discussed in the next chapter.

3.6.2 Footprint on Detector

By collecting the entire diffracted beam in the detector without moving the sample or the detector, the integrated intensity of the rod is measured directly. The size of

hkl	Width [mm]	Length [mm]	Area [mm^2]
2 0 1.5	0.42	4.67	1.46
2 0 2.0	0.35	3.87	1.10
2 0 2.5	0.32	3.28	0.88
3 1 0.5	1.01	5.47	2.77
3 1 1.0	0.83	4.73	2.19
3 1 1.5	0.58	3.82	1.46

Table 3.2: Width, length and area of the beam footprint on the sample surface for a Si(001) wafer using 10 keV photons. Calculations are based on an incident slit which is 0.25 mm wide and 1.00 mm tall.

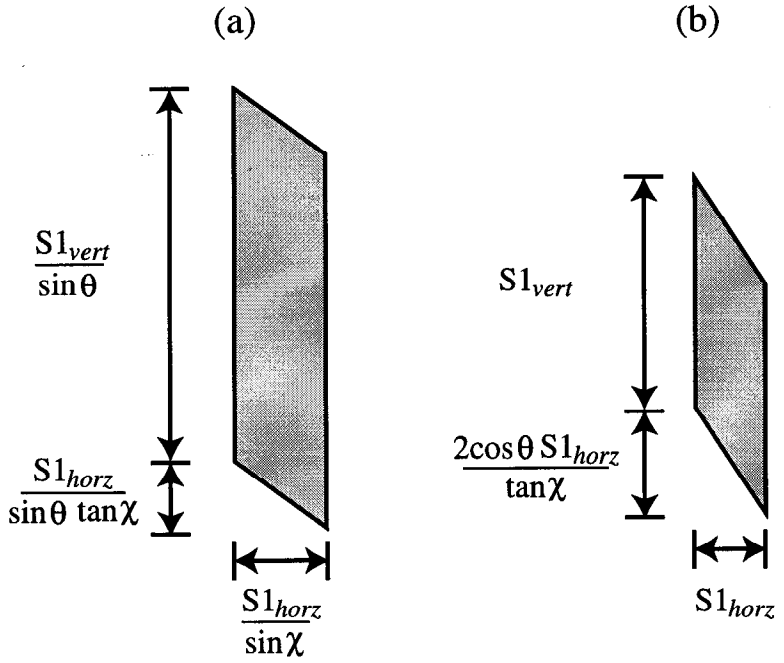

Figure 3.9: Footprint of a perfect collimated beam on the sample (a) and detector (b) for an incident slit size $S1_{vert}$x$S1_{horz}$ for the case of $\chi > \chi_{crit}$

the beam footprint at the detector is determined by the size of the slit S_1 positioned prior to the sample. For a collimated beam the footprint on the detector will have the shape shown in Figure 3.9b. The width of the footprint on the detector is the same as the width of the incident beam ($S1_{horz}$), whereas the height is given by:

$$3S1_{vert} \quad , \chi \leq \chi_{crit} \tag{3.12}$$

$$S1_{vert} + \frac{2S1_{horz}}{\tan \chi} \quad , \chi > \chi_{crit} \tag{3.13}$$

For the slit sizes listed in Table 3.1 the width of the footprint on the detector is 0.25 mm. The height varies from 1.4-1.7 mm for the (202) rod and from 2.1 mm to 3.0 mm for the (311) rod. Beam divergence will increase these values. By using a detector slit of 1×4 mm the total diffracted beam was collected for all the rods measured.

3.6.3 CTR Scans

In crystal truncation rod scattering the scattered intensity along the surface normal in the vicinity of a Bragg reflection is probed. A pure l-scan samples the intensity by moving all four diffractometer motors simultaneously in such a way that the projection of the scattering vector onto the surface stays constant. The trajectory of the scattering vector in reciprocal space is shown in Figure 3.10. However, since the width of the rod is narrow the crystal would have to be very well aligned in order for the scattering vector to probe the rod at all points during a l-scan. Also a pure l-scan would give the total scattered intensity which in addition to the rod intensity includes thermal diffuse scattering and scattering from defects (see section 3.7). Instead of performing a pure l-scan along the rod, θ-rocking curves were measured at a series of l-values in order to separate the CTR scattering from these other types of scattering. In a θ-scan only the sample is rotated and thus the length of the scattering vector stays constant, while its direction is being rotated in reciprocal space. A schematic of a θ scan is also shown in Figure 3.10. As the crystal is turned the scattering vector moves across the rod. The width of the rocking curve is determined

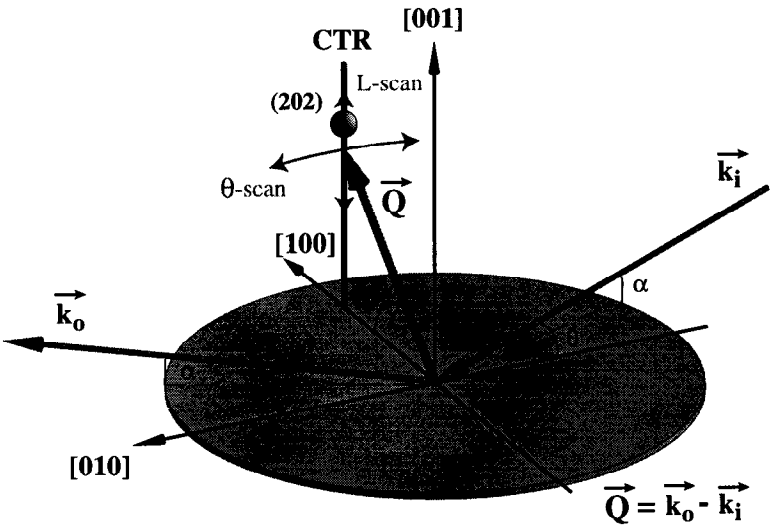

Figure 3.10: The trajectory of a θ and l-scan is shown for the 202 rod of a Si(001) wafer.

by how much the crystal is rotated before the rod intensity is no longer collected by the detector. The scattering from the rod can be cut off by either the horizontal or vertical slits on the detector. The critical angle setting for the transition from the horizontal to the vertical slit being defining occurs at:

$$\tan\chi = \frac{a}{b}\cos\theta, \tag{3.14}$$

where a and b are the horizontal and vertical acceptance of the detector, respectively. Since these experiments operate with a large in-plane slit (a = 2 mrad, b = 8 mrad) the transition will occur for relatively large χ-values. For silicon using 10 keV photons the transition occurs at (2,0,3.55) of the (202) rod and hence it does not affect these data. For all our rod scans the diffracted beam from the rod is defined by the out-of-plane slit. The total width w of the CTR as measured using a θ-rocking curve is a function of the horizontal angular acceptance of detector b and can be derived from equation 10 in [49] as:

$$w = \frac{b}{2}\frac{\tan\chi}{\cos\theta}. \tag{3.15}$$

As the sample is rotated, different l-values of the rod are being probed. The slope at the center of the rocking curve is an indication of the change in intensity of the

CTR at that rod position, e.g. closer to the Bragg peak the slope of the rocking curve will be larger than further away. The length of the rod scanned is given by:

$$\triangle l = \frac{cb}{\lambda \cos \chi} \tag{3.16}$$

where c is the lattice parameter of the crystal along the z-direction. Independent of the h, k-value of the rod, when rotating the crystal in a positive direction around the θ-axis the rod is probed toward increasing l-values. The slope at the top of the rocking curve is therefore positive below a Bragg reflection and negative above one.

3.7 Data Correction

The CTR intensity was selected as the intensity at the center of the rocking curve minus the background intensity. These results were then corrected for the change in atomic form factor as a function of the magnitude of the scattering vector, the Debye-Waller factor, the Lorentz-factor, and the area of the sample illuminated by the beam. Since the scattering plane is vertical and the beam is largely polarized in the horizontal plane, there is no correction for polarization effects.

3.7.1 Temperature effects

Thermal vibrations of the atoms about their lattice positions have two effects on the scattered intensity. First, the displacements of the atoms decrease the intensity by a factor of e^{-2M} but without changing the shape of the reciprocal lattice features. The quantity M is a measure of how far the atoms are displaced from their equilibrium position and is given as [44]:

$$M = 8\pi^2 \bar{u_s^2} \frac{\sin^2(\theta)}{\lambda^2}, \tag{3.17}$$

where $\bar{u_s^2}$ is the mean-square of the vertical displacement of the atoms along the scattering vector. M can also be approximated as a function of the Debye temperature Θ_D, which is a measure of the stiffness of the crystal:

$$M = \frac{6h^2 T \sin^2 \theta}{m k_B \Theta_D^2 \lambda^2} \left(\frac{\Theta_D}{4T} + \frac{T}{\Theta_D} \int_0^{\Theta_D/T} \frac{z}{e^z - 1} dz \right), \tag{3.18}$$

where h is Plank's constant, k_B the Boltzmann constant, m the atomic weight and T the temperature. The expression inside the parentheses is known as the Debye-Waller factor. Evaluating the equation for silicon at room temperature using T=298 K, Θ_D=640 K [50] and m_{Si}=(28.086 g/mole)/N_A yields:

$$M = 214.1\frac{\sin^2\theta}{\lambda^2}\ \mathring{A}^2. \tag{3.19}$$

Besides the decrease in scattering power as a function of the length of the scattering vector, the thermal vibrations also give rise to a broad weak background of intensity. This scattering, which is called thermal diffuse scattering (TDS), is coupled to the phonons within the crystal and can be expressed as the sum of the scattering arising from each individual lattice vibration mode. The derivation is shown in detail in James [44] and results in:

$$I_{TDS} = \frac{1}{2}|f_o|^2 e^{-2M}\sum_{\phi j} G_{\phi j}\{I_o(\vec{Q}-\vec{g}) + I_o(\vec{Q}+\vec{g})\}, \tag{3.20}$$

where $\vec{g}$ is the wavevector of the phonon in polarization state j. I_o refers to the intensity from the crystal at rest so that I_o with the argument $\vec{Q}-\vec{g}$ offsets the intensity spectrum by the wavevector $\vec{g}$ of the phonon with respect to the reciprocal lattice. The factor $\frac{1}{2}G_{\phi j}$, which is a function of the atomic displacements, causes the intensity to be much lower than that of I_o. In a crystal the number of phonons allowed is a function of the crystal size, e.g. for a simple cubic crystal the number of lattice waves is $3N_1N_2N_3$, where N_1,N_2 and N_3 correspond to the number of unit cells in the three orthogonal directions. The prefactor 3 arises from the three types of polarization. The scattered intensity associated with a single phonon has features in reciprocal space which are similar to that of the spectrum from the crystal itself, but the intensity is much weaker. Instead of a peak at the reciprocal lattice point, the TDS has two maxima which are displaced symmetrically about the Bragg peaks according to the wavevector of the phonon $\pm\vec{g}$. The shorter wavelength of the lattice vibration, the further away from the Bragg reflection the intensity will be. When the scattered intensity associated with the phonons is summed up, the resulting spectrum is continuous and centered at the reciprocal lattice points. Due to preferential directions of the lattice vibration along the crystallographic directions, the TDS intensity

appears as streaks connecting the Bragg peaks. Thus, a substantial part of the TDS is at the same place in reciprocal space as the crystal truncation rods and the TDS needs to be subtracted from the CTR data. However, the CTR is a very narrow feature, whereas the TDS is much broader. The width of the rod is inversely proportional to the length over which the x-rays scatter coherently, which is approximately 10 μm for this experiment as will be discussed in detail in Chapter 4. The TDS, on the other hand, has components which are inversely related to the wavelength of the phonons. Thus, there will be intensity at the rod position from phonons larger than the coherent scattering length and up to size of the crystal, but also TDS intensity at much broader positions corresponding to phonons with a periodicity of the unit cell. Since the TDS is a slowly varying function, it will be subtracted as background from the rocking curves which cut through the rod.

3.7.2 Scattering effects

Atomic form factor

Elastic scattering from electrons decreases as a function of the length of the scattering vector. Hence the form factor decreases as l increases and the scattered rod intensity would appear asymmetric without that correction. The form factor has been calculated using Cromer and Mann [51] and taken into account.

Scattering from defects

Huang scattering is another type of diffuse scattering which appears in the vicinity of the Bragg peaks. It arises from point defects (vacancies and interstitials) within a crystal. Besides residual defects in silicon wafers, the defect density also depends on damage caused by implantation of dopants. The intensity of Huang scattering can be expressed by the reciprocal lattice vector of the Bragg peak ($\vec{Q}_{hkl}$) and the reduced scattering vector $\vec{q}$, i.e. $\vec{Q} = \vec{Q}_{hkl} + \vec{q}$ [52]:

$$I_{Huang} = N|f_o|^2|\vec{Q}_{hkl} \cdot \vec{D}(\vec{q})|^2 \tag{3.21}$$

where N is the number of defects and $\vec{D}(\vec{q})$ is the Fourier transform of the elastic displacement field caused by the defects. The magnitude of the elastic displacement field is inversely proportional to the distance from the defect, but the angular dependence is a function of the anisotropy of the crystal. Thus, the Huang scattering decreases with a $1/q^2$ dependence away from the Bragg reflection as is the case of CTR scattering from a flat surface. However, the Huang scattering is very diffuse with a shape that depends on the actual types of defects. Thus scattering from defects is subtracted from CTR scattering simultaneously with thermal diffuse scattering, as they are both slowly varying. In addition to Huang scattering, defects within the crystal give rise to other types of diffuse scattering, e.g. scattering due to displaced atoms far from defects, defect clusters, dislocation loops etc. They all give rise to diffuse scattering which is much broader then the rod, and are therefore subtracted as background.

3.7.3 Geometric effects

Lorentz-factor

A volume element in reciprocal space is related to the scattering volume of the sample through the Lorentz factor. As the crystal is rotated about the 2θ axis, the volume element in reciprocal space probed by the detector increases for a constant slit size. Since the polarization factor for synchrotron radiation using a vertical scattering plane is 1, the Lorenz factor is simply $1/\sin 2\theta$.

Sample area

Variations in area illuminated by the beam are proportional to $\sin\theta \sin\chi$ when $\chi > \chi_{crit}$, which is the case for most of the rods measured in this thesis with the chosen slit slitting. Crystal truncation rods arise from scattering from surface or interfaces and therefore it is the surface area on the sample and not the illuminated volume of the crystal which needs to be considered for normalization.

3.8 Instrument resolution

The instrument resolution corresponds to the volume of reciprocal space probed by the detector without moving the sample. It is a function of the divergence of the incident beam, the angular acceptance of the detector slits and the spectrum of wavelengths passed by the monochromator. The instrument function is convolved onto the intrinsic features in reciprocal space, thus smearing out those features and reducing the resolution of the experiment.

The initial divergence of the beam on beamline 10-2 is defined upstream of the mirror by slits. Reflection off the focusing mirror causes the horizontal divergence of the beam to couple into the vertical divergence[53]. For a slit acceptance of 128 μrad vertical and 1.0 mrad horizontal, focusing using a 3.6 mrad angle of incidence cylindrical mirror results in a vertical divergence of 145 μrad. The horizontal divergence remains 1 mrad. This beam divergence corresponds to a cone segment of wave vectors $\vec{k}_i$ incident on the sample.

The beam footprint on the sample and slits positioned immediately in front of the detector define the angular acceptance of the detector. In this experiment the angular acceptance of the detector was 8 mrad in the scattering plane and 2 mrad perpendicular to the scattering plane. Hence the slit size allows for a cone of outgoing wave vectors $\vec{k}_o$ from the sample.

The energy resolution of a beam of photons from a synchrotron source is determined by a convolution of the Darwin width of the monochromator and the vertical divergence of the beam. The Darwin width, which is the intrinsic width of a Bragg reflection, is 26.8 μrad at 10 keV for a silicon(111) reflection. Since the vertical divergence (145 μrad) is significantly larger, the Darwin width can be neglected when estimating the energy spread of the beam passed through the monochromator. The energy resolution of the Si(111) double monochromator can be deduced from Bragg's law (Eqn. 3.3):

$$\frac{dE}{E} = -\cot\theta d\theta. \tag{3.22}$$

Thus, for a Bragg angle of ($\theta = 11.4°$) and 145 μrad vertical beam divergence the

energy resolution is 7.2 eV. The energy spread of photons also corresponds to a range of allowed wave vectors. However, a variation in incident wavelength only changes the lengths of the wave vectors and not their direction.

The scattering vector $\vec{Q}$ is given by the sum of the incident $\vec{k}_i$ and outgoing wave vector $\vec{k}_o$ at the sample. For a given range of incident and outgoing wave vectors, there exists a range of scattering vectors. This volume of allowed scattering vectors in reciprocal space is the instrument function.

The spread of incident wave vectors is small compared to the angular acceptance of the detector, so as a first approximation the incident beam can be treated as a plane wave. The rectangular cone of outgoing wave vectors $\vec{k}_o$ due to the angular detector acceptance can be represented as a plane of allowed scattering vectors at some distance from the sample. This plane is inclined with respect to the sample surface normal by an angle γ. It can be seen geometrically that this angle is related to the diffractometer angles θ and χ [46] by:

$$\sin\gamma = \sin\theta \sin\chi. \tag{3.23}$$

Note, the angle γ is equal to the incident angle α and take-off angle β of the beam on the sample (in ω=0 mode [46]). The range of lengths of allowed scattering vectors ΔQ corresponds to the energy bandwidth, i.e.

$$\Delta Q = -\frac{4\pi \sin\theta}{\lambda}\frac{\Delta\lambda}{\lambda} = Q\frac{\Delta E}{E}. \tag{3.24}$$

This causes the plane of allowed scattering vectors to be extended in the direction of the scattering vector to form a parallelepiped in reciprocal space. The angle between the plane of scattering vectors and the extension along the scattering vector due to the energy bandwidth is equal to θ.

Because the CTR's are parallel to the surface normal, the angle between the CTR's and the plane of allowed scattering vectors is also equal to γ. The out-of-plane component of the scattering vector $Q_\perp$ is given by:

$$Q_\perp = \frac{4\pi \sin\alpha}{\lambda}, \tag{3.25}$$

where α is the angle of incidence on the sample. Since $\alpha = \gamma$, the angle between the resolution function and any rod depends only on the l-component of the rod, e.g. the angle between the resolution function and the $20l$ rod at (2,0,1.5) is equal to the intersection with the $31l$ rod at (3,1,1.5).

In order to evaluate the in-plane resolution one needs to convert the instrument function from the coordinate system of the diffractometer to the coordinate system of the crystal. A horizontal acceptance a and vertical acceptance b of the detector can be related to the right handed coordinate system of the scattering plane (z': direction of the scattering vector, x': direction perpendicular to the scattering plane, y': in the scattering plane perpendicular to both x' and z') by:

$$\begin{pmatrix} x' \\ y' \\ z' \end{pmatrix} = \begin{pmatrix} 1 & 0 & 0 \\ 0 & -\sin\theta & \cos\theta \\ 0 & \cos\theta & \sin\theta \end{pmatrix} \begin{pmatrix} a \\ b \\ 0 \end{pmatrix} \tag{3.26}$$

The spread in wavelength of the beam corresponds to an additional spread in the z'-direction. A rotation of χ about the y'-axis transforms the instrument function onto a coordinate system which is aligned with respect to the surface of the sample (z: direction along surface normal, x: direction in the surface of the sample perpendicular to the scattering direction, y: direction in the surface along the scattering direction):

$$\begin{pmatrix} x \\ y \\ z \end{pmatrix} = \frac{2\pi}{\lambda} \begin{pmatrix} \sin\chi & 0 & \cos\chi \\ 0 & 1 & 0 \\ -\cos\chi & 0 & \sin\chi \end{pmatrix} \begin{pmatrix} x' \\ y' \\ z' \end{pmatrix}. \tag{3.27}$$

These equations will be used in Chapter 4 in the discussion of the lateral length scales of roughness measured by crystal truncation rod scattering.

Chapter 4

Interfacial Roughness

Summary

The use of CTR scattering for extracting the roughness of surfaces and interfaces is examined. A modified version of the theory by Andrews and Cowley is presented. A variety of rods are present at the surface, so the question arises as to whether the same information about the roughness of the interface is obtained from different rods. It is shown that an ordered roughness does not have a different effect on different truncation rods. Lateral roughness scales probed with Crystal Truncation Rod scattering are discussed. The influences of the coherence of the beam and the instrument function are discussed in detail. A comparison of the roughness of wafers terminated by a native oxide measured by Atomic Force Microscopy (AFM) and CTR show similar although not identical results. Differences in measured roughness between the two techniques can be explained by the difference in the lateral length scale probed. An analysis of the roughness wavelength of the AFM images support this.

4.1 Modified Cowley Theory

In a previous chapter the theory by Andrews & Cowley [16] was described. The intensity from a surface with a Gaussian roughness profile characterized by the rms roughness σ is given by:

$$I(\vec{q}_\perp) = \sum_{\vec{\tau}} \frac{|\rho_0(\vec{\tau})|^2}{q_\perp^2} \exp(-\sigma^2 q_\perp^2). \tag{4.1}$$

For a crystal with a rough surface, the exponential decay of scattered intensity evident in Eqn 4.1 means that the scattered intensity at a particular $q_\perp$ is dominated by the nearest Bragg peak. Thus the intensity is directly given by:

$$I(\vec{q}_\perp) = \frac{|\rho_0(\vec{\tau})|^2}{q_\perp^2} \exp(-\sigma^2 q_\perp^2), \tag{4.2}$$

where $q_\perp$ and $\vec{\tau}$ refer to the closest Bragg peak.

The difference between the sum over all Bragg peaks and the intensity from the closest Bragg peak is shown in Figure 4.1 for the $20l$ rod of a silicon(001) wafer. Even for a roughness of only 0.5 Å, the difference is less than 1 % a full reciprocal lattice unit away from the reflection. Thus, diffraction data obtained from crystals with significant roughness is best fitted to a function with a $1/q_\perp^2$ rather than a $\sum_{\vec{\tau}} 1/q_\perp^2$ as proposed by Andrews & Cowley or the $1/\sin^2(aq_\perp)$ dependence given by Robinson.

This modified version of the theory by Andrews & Cowley is used throughout this thesis to fit the data. It not only gives very nice fits to the scattering data, but it is also consistent with the theory derived for a miscut crystal as will be discussed in Chapter 5.

4.2 CTR Sensitivity to Roughness Texture

The theory developed above to describe the CTR intensity and its dependence on roughness does not distinguish between different rods (e.g. 20L, 31L, etc.). Clearly both the direction and the length of the scattering vector differ for each rod, so one might expect that the CTR is coupling into roughness in a particular direction due to

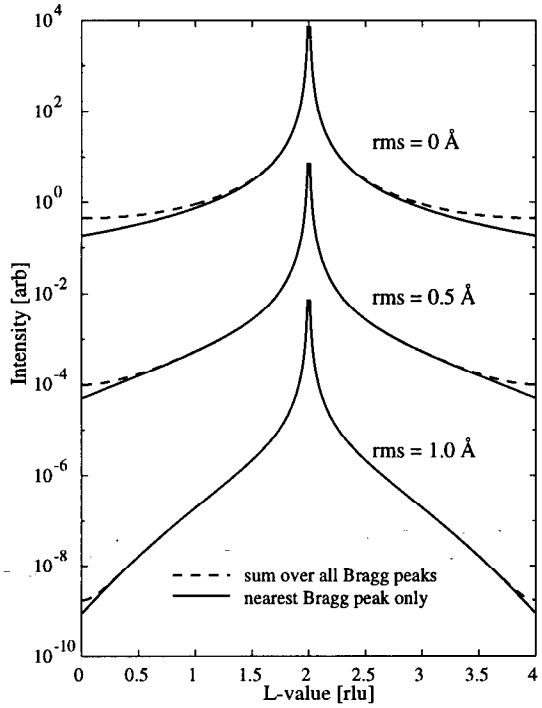

Figure 4.1: Calculation of the $20l$ rod intensity of silicon(001) for three surface rms roughnesses: 0 Å, 0.5 Å and 1.0 Å. The curves derived for the different roughnesses are offset for clarity. The solid lines corresponds to the rod intensity from the 202 Bragg peak, whereas the dotted lines is the summed intensity for all rods with the same in-plane momentum transfer, e.g. $20\bar{6}$ $20\bar{2}$ 202 206 etc.

its in-plane component. In order to explore this hypothesis it is convenient to consider a one-dimensional roughness with a single periodicity as shown in Figure 4.2. The scattered intensity from such a structure is derived using the layer summation method in Appendix A and is shown to be:

$$I = 4|f_0|^2 \cos^2(\pi(h\Lambda - lT)) \frac{\sin^2(\pi h 2\Lambda M)}{\sin^2(\pi h 2\Lambda)} \frac{\sin^2(\pi h \Lambda)}{\sin^2(\pi h)} \frac{\sin^2(\pi k N_2)}{\sin^2(\pi k)} \frac{\sin^2(\pi l N_3)}{\sin^2(\pi l)}, \quad (4.3)$$

where f_0 is the atomic form factor, 2Λ is the period of the grating and T is the step height. h, k and l correspond to the crystallographic axes of the simple cubic lattice, N_2 and N_3 are the number of atoms in the k and l direction, respectively, whereas M is number of grating periods on the crystal.

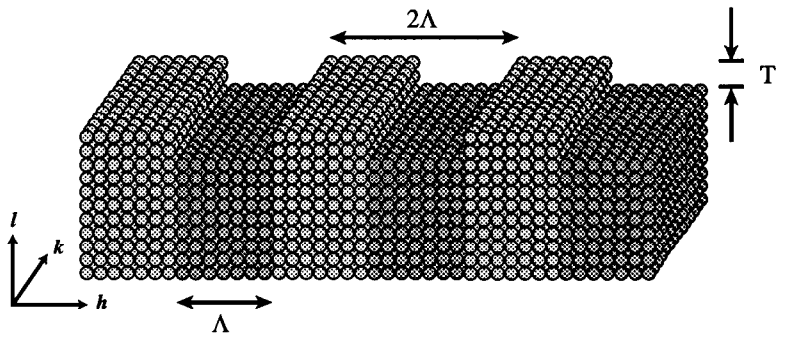

Figure 4.2: Illustration of a crystal surface with a one-dimensional grating periodicity of 2Λ. The step height is given by T. The calculation assumes a cubic crystal with Λ and T being integer numbers of unit cells.

The last three factors in the equation above correspond to the standard Laue factors resulting from adding up the scattering from a perfect crystal, except that in the h-direction the scattering is only summed up over the number of atoms in a single terrace (Λ) instead of the full crystal length. Consequently, the decay of the scattering in the h-direction is slower, i.e. the diffraction condition has been relaxed. The second factor in the equation, in which the scattering from the periodicity of the terraces is taken into account, causes a sharp decay of the scattering in the h-direction but allows scattering to occur with a periodicity of $1/\Lambda$ in reciprocal space. These subsidiary maxima will appear close to the Bragg peak where the product of the first two sine terms is non-zero. In the l-direction the intensity falls off as $1/q^2$ away from the Bragg reflection due to the presence of the surface. This is the crystal truncation rod (CTR). The cosine term results in a faster decay of intensity caused by roughness of the surface (the grating), with taller steps causing the intensity to decay more quickly. It affects each of the subsidiary maxima in the same way. A model calculation based on these equations is shown in Figure 4.3.

What is evident from the above model is that every CTR, independent of its in-plane component, has the same decay in the l-direction. An ordered roughness in a particular direction along the surface results in additional scattering visible as

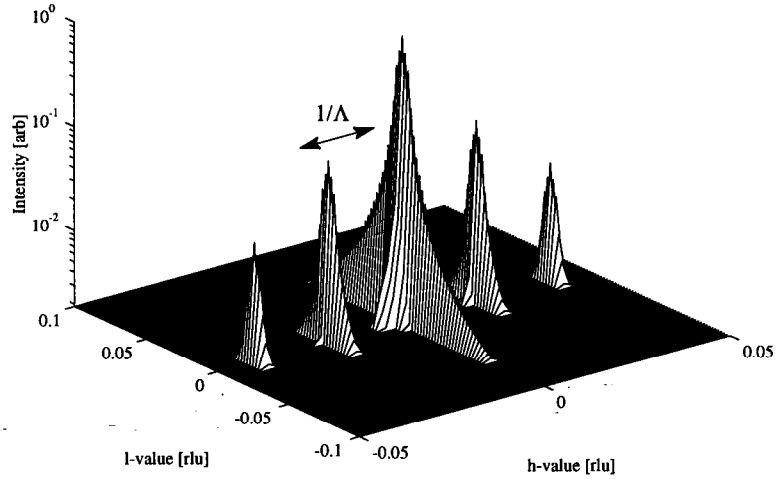

Figure 4.3: Features in reciprocal space due to the periodic roughness shown in Figure 4.2. Streaks of intensity can be seen parallel to the CTR and spaced by $1/\Lambda$ in the direction of the ordering. The intensity of these side lobes decreases with the distance from the Bragg reflection. The decay in the l-direction is identical for all the peaks in the figure.

side-lobes on either side of the Bragg peak (in the direction of the ordering), as seen in Figure 4.3. Thus, a periodic roughness can be seen as additional scattering at the in-plane momentum transfer of that periodicity or an allowed reflection plus that periodicity. For a range of roughness periodicities on the surface, scattering will occur over an equivalent range in reciprocal space. Thus, for a range of periodicities out to the sample size, the intensity will fill in between the subsidiary maxima in Figure 4.3. This is the diffuse scattering observed around each Bragg peak, including the 000 peak. Note that this diffuse scattering is observable as an increase in intensity in the h and k-directions, not an increase in the l-direction. Interfacial roughness does not affect the peak scattered intensity from a Bragg peak, only the decay rate of that intensity in a direction perpendicular to the surface. As discussed above, a perfectly flat interface will result in a decay in the CTR intensity which is inversely

proportional to the square of the scattering vector away from the Bragg reflection. The scattering from a rough surface results in diffuse scattering and hence a decrease in the CTR intensity. A rougher surface will have a CTR which decays more rapidly. The width of the crystal truncation rod parallel to the surface is affected by diffuse scattering, with scattering from long wavelength roughness visible close to the $h, k=$ integer values, and scattering from short wavelength roughness located further from the CTR. Whether one can observe a particular wavelength of roughness on the surface depends on the scattering resolution employed. The poorer the instrumental resolution, the more the long wavelength diffuse scattering will be incorporated into the main CTR scattering, making it unresolvable.

4.3 Lateral Roughness Scale

Silicon surface and interface morphology is affected by roughness on every length scale. At long wavelengths wafer curvature dominates while mechanical damage due to polishing can result in roughness on the micron length scale. At still shorter length scales, such things as terraces or islands can cause height variations, and at the atomic level vacancies or point defects occur. Generally, device characteristics such as mobility, charge-to-breakdown and carrier lifetime are affected by roughness on a length scale of less than 1000 Å.

The simplest description of surface or interfacial roughness is the root mean square (rms) value. This metric is the average of the height-height correlation of the surface over all length scales. Experimentally, the average occurs between the minimum and maximum distance probed by the technique employed to measure the roughness. These distances are different for each technique, hence the measured rms value may differ depending on the overlap between the length scale of the roughness and the spatial limits of the measurements. A more complete description of the surface or interfacial roughness would include a discussion of the specific length scales at which the roughness is occurring [54].

A particular technique is only sensitive to a certain range of roughness length scales. In order to compare techniques one must be careful to take this difference in

length scales into account.

The lower limit of the lateral roughness measured by scattering is given primarily by the wavelength λ of the incoming wave field. This can be illustrated by considering the grating equation, which applies to a surface with only one roughness period Λ:

$$\sin\theta_o = \sin\theta_i + m\frac{\lambda}{\Lambda}, \qquad m : integer \tag{4.4}$$

θ_i and θ_o are the incident and outgoing angles, respectively. In the specular direction ($\theta_i = \theta_o$) the diffracted wave is always in phase, independent of the lateral roughness dimension. If the incident and diffracted angle differ, the path length difference determines if the diffracted waves are in or out of phase. If corrugations on the surface have a spatial extent which is large compared to the wavelength of the incident wave, the wave will scatter into many different directions. For a period which is less than that of the incident wavelength ($\Lambda < \lambda$), there are no allowed directions other than the specular, and the surface will appear perfectly smooth. Thus the wavelength of the probe defines the lower limit of the lateral roughness periodicity to which it is sensitive.

The upper limit on the sensitivity of the probe to lateral roughness depends both on the coherent scattering length and the instrument resolution. Photons separated by a distance less than the coherent scattering length will have a well-defined phase relationship, whereas photons at distances larger than this scattering length will have a random phase relationship. Thus photons separated by less than the scattering length will interfere with each other, whereas outside of that length the photons only add up as intensities. Hence roughness on length scales larger than this coherent scattering length will not be observed. The reason the instrumental resolution is important is that scattering from roughness which cannot be separated from the specular scattering by the instrument does not contribute to the roughness measured. That is, unless the roughness is seen as a reduction in the specular reflectivity, it cannot be measured. The coherent scattering length is a function of the longitudinal and transverse coherence of the beam and the scattering angle, whereas the instrument function is defined by the incident beam monochromaticity and the slit system used for the experiment. These issues are discussed further in the sections below.

4.3.1 Coherence

In a sufficiently small volume of the sample the photon wave packets maintain a phase relationship so that they add up in phase. Within this volume the x-rays scatter coherently. At larger distances the x-rays no longer interfere and thus add up as intensities. Therefore, information cannot be obtained about any correlations within the sample at distances larger than this characteristic length $\Lambda_{coherent}$ where the x-rays scatter coherently. The coherence of the beam can be separated into two parts: longitudinal and transverse coherence.

Longitudinal coherence of x-rays, also called temporal coherence, is the distance in the propagation direction of the x-rays over which the x-rays maintain coherence. This characteristic length is a function of the wavelength spread $\Delta\lambda$ of the beam and defined as:

$$\Lambda_{temporal} = \frac{\lambda}{2}\frac{\lambda}{\Delta\lambda} = \frac{\lambda^2}{2\Delta\lambda} \tag{4.5}$$

where λ is the average wavelength of the x-rays. For an energy spread of 7.2 eV (as derived in the Chapter 3) for 10 keV photons the temporal coherence is 860 Å.

The coherence of the beam in the direction perpendicular to the propagation direction of the beam depends on the source size and the distance to the source. This transverse coherence defines an area over which all the rays effectively originate from a point source and thus maintain a phase relationship. The transverse coherence can be characterized as an opening angle $\theta_{transverse}$ which is determined by the source size d and the wavelength λ:

$$\theta_{transverse} = \frac{\lambda}{2\pi d} \tag{4.6}$$

At a distance R away from the source the transverse coherence length is (for small angles):

$$\Lambda_{transverse} = R\theta_{transverse} = \frac{R\lambda}{2\pi d} \tag{4.7}$$

For a non-circular source the transverse coherence of the beam becomes anisotropic. At beamline 10-2 the diffractometer is 25.4 m away from the ~100 μm (vertical FWHM) by ~3 mm (horizontal FWHM) source, yielding a transverse coherence length of 5.0 μm in the vertical direction and 0.25 μm in the horizontal direction.

Since we are scattering in the vertical plane it is the vertical transverse coherence length of 5.0 μm which is important.

The length on the surface over which the x-rays scatter coherently is only a function of the transverse coherence when the path length of all the scattered photons is constant, whereas the temporal coherence becomes important when a path difference is present. In reflectivity from a single surface the path length of all the reflected x-rays is constant. In this case it is only the transverse coherence length which defines the sensitivity limit. The length in the sample over which the x-rays scatter coherently is then given by the projection of the transverse coherence onto the plane of reflection. For a scattering angle θ:

$$\Lambda_{\parallel} = \frac{\Lambda_{transverse}}{\sin\theta}. \tag{4.8}$$

At low angles this length can be quite large for specular reflectivity. For an incident angle of 10 mrad $\Lambda_{\parallel}$ is $\sim$500 μm using the vertical transverse coherence length derived above (5.0 μm).

In Bragg scattering or in the case of reflectometry from multiple interfaces, the photons collected by the detector have experienced different path lengths and thus the temporal coherence of the beam is important. In back-scattering geometry the length in the sample over which the x-rays scatter coherently depends only on the temporal coherence. The path difference between rays diffracted from two planes separated by the distance a is given by twice that distance, i.e. $2a$. Thus, $\Lambda_{coherent}$ in back scattering is half that of the temporal coherence length. In the more general case, the characteristic length in the direction perpendicular to the diffraction planes over which the x-rays scatter coherently is for a diffraction angle θ given by:

$$\Lambda_{\perp} = \frac{\Lambda_{temporal}}{2\sin\theta}. \tag{4.9}$$

Note that in Bragg scattering, the longitudinal coherence only influences the length over which the x-rays scatter coherently in the direction of the scattering vector, whereas the in-plane direction is only affected by the transverse coherence of the beam.

In the case of crystal truncation rod scattering, scattering of x-rays occurs from the outermost atomic planes of the crystal. Therefore, there is essentially no path

difference between the rays, so that $\Lambda_{coherent}$ is dominated by the transverse coherence of the beam. This might seem counter-intuitive since CTR scattering is Bragg scattering. However, it is the tails far away from the Bragg peak which are being probed and thus only very few atomic layers contribute to the diffraction. This can be seen in kinematical diffraction theory where the intensity is a function of the planes N over which scattering occurs [38]:

$$I \propto \frac{\sin^2(Nx)}{\sin^2(x)}. \tag{4.10}$$

The penetration depth can be derived and yields:

$$L_{depth} = \frac{0.94\lambda}{\Delta\theta \cos\theta} \tag{4.11}$$

which is essentially the Sherrer equation. A decrease in the number of planes from which scattering occurs results in a broader diffraction peak due to a relaxation of the diffraction condition. Thus by probing a broad rocking curve as in the case of crystal truncation rod scattering, only the top few planes contribute to the signal. For instance, the change in θ between the (2,0,1.5) and (2,0,2.5) reflections is ~5 degrees which implies a penetration depth of approximately 15 Å. This limited penetration depth justifies the use of the transverse rather than the longitudinal coherence length.

For a 5.0 μm transverse coherence length the in-plane coherence length for the rod associated with the (202) reflection is ~15.5 μm using equation 4.8. For the (311) rod the lateral coherence length is approximately 13 μm.

4.3.2 Instrument Resolution

In CTR scattering the intensity of the Bragg tails is probed in the direction perpendicular to the surface. The intersection of the instrument function with the rod determines the resolution of the experiment. As shown above, scattering from roughness with a long in-plane wavelength has Fourier components close to the rod whereas roughness with a short wavelength results in scattered intensity further away from the rod. A projection of the instrument function onto the surface of the sample gives the in-plane resolution of the experiment. Scattering from roughness with a sufficiently

large in-plane correlation length will be collected by the detector simultaneously with the CTR, so it cannot be distinguished from the CTR scattering. The technique is thus not sensitive to roughness with an in-plane correlation length which will give rise to scattering close enough to the rod that it cannot be resolved by the instrument function. Assuming non-directional roughness, scattering from roughness of the same correlation length will appear at a distinct radius away from the center of the rod. Thus, the minimum radial distance of the projected resolution function is inversely proportional to the upper limit of roughness measured.

This minimum radius is given in inverse Angstrom by:

$$R_{min} = \frac{\pi \sin\theta(a \sin\chi + \Delta Q \cos\chi)}{\lambda\sqrt{\sin^2\theta + \cos^2\theta\cos^2\chi}} \tag{4.12}$$

thus the maximum lateral roughness correlation at which the measurement is sensitive is given as the inverse:

$$\Lambda_{max} = \frac{2\pi}{R_{min}} = \frac{2\lambda\sqrt{\sin^2\theta + \cos^2\theta\cos^2\chi}}{\sin\theta(a \sin\chi + \Delta Q \cos\chi)} \tag{4.13}$$

The smallest wavelength of roughness indistinguishable from the CTR varies depending on the specific rod that is measured. In our case, this wavelength of the (202) rod varies from 4600 Å at (2,0,1.5) to 2600 Å at (2,0,2.5); for the (311) rod this wavelength ranges from 9300 to 4600 Å.

The sensitivity to lateral roughness of the instrument function is considerably smaller than that of the lateral coherent scattering length, thus, the upper limit of roughness measured by CTR scattering (using our experimental setup) is given by the in-plane instrument resolution of the rods associated with the (202) and (311) reflection. Thus, the roughness length scale ranges from half a micron down to ~1.2 Å for the CTR measurements.

4.4 Experimental Results

4.4.1 Samples

The wafers used for this experiment were p-type, 6 inch epitaxial (001) silicon. They were cleaned by an HF dip and cold water rinse, followed by three variations of an RCA clean[55] to achieve different levels of surface roughness. Wafer set A was given a standard RCA clean, consisting of an SC1 bath (5:1:1 H_2O:NH_4OH:H_2O_2), rinse, SC2 bath (5:1:1 H_2O:HCl:H_2O_2), rinse and spin dry. Wafer set B had a 50% reduction in the ammonium hydroxide (NH_4OH) in the SC1 bath, and Wafer set C was given a hot water rinse in place of the SC1 treatment. In the SC1 bath, a protective oxide is formed by the H_2O_2 which inhibits roughening of the surface. The lack of this oxide for wafers in set C allowed some etching of the surface in the hot water, creating the roughest of the three surfaces. Sets B and C had the same SC2 clean, rinse and spin dry as set A. Furnace oxidation was carried out at 800°C, and followed by a 925°C N_2O anneal. Final thickness for the oxides was 60 Å. Data were collected from (2,0,1.5) to (2,0,2.5) for all wafers and from (3,1,0.65) to (3,1,1.4) for the thermally oxidized wafer treated with the full ammonium hydroxide concentration.

4.4.2 Influence of Thermal Oxidation

Crystal truncation rod intensities for the (202) reflection are shown for wafer set A in Figure 4.4. The fall-off in intensity for the wafer terminated by a thermal oxide is clearly slower than the fall-off for the native oxide. Without further analysis we can conclude that the growth of a thermal oxide smooths the interface. The data from below and above the Bragg reflection were fitted simultaneously to the modified theory described above. We obtain an rms roughness of 2.0 Å for the thermal oxide sample and 2.4 Å for the native oxide sample. Error bars on the rms value of the x-ray scattering measurements are estimated to be ±0.1 Å. Smoothing of the interface due to thermal oxidation is seen for all three wafer sets. This has been observed previously for thermally grown oxides on Si(001) for film thickness larger than 1000 Å [34, 56], but the present measurements show that significant smoothing has occurred even for

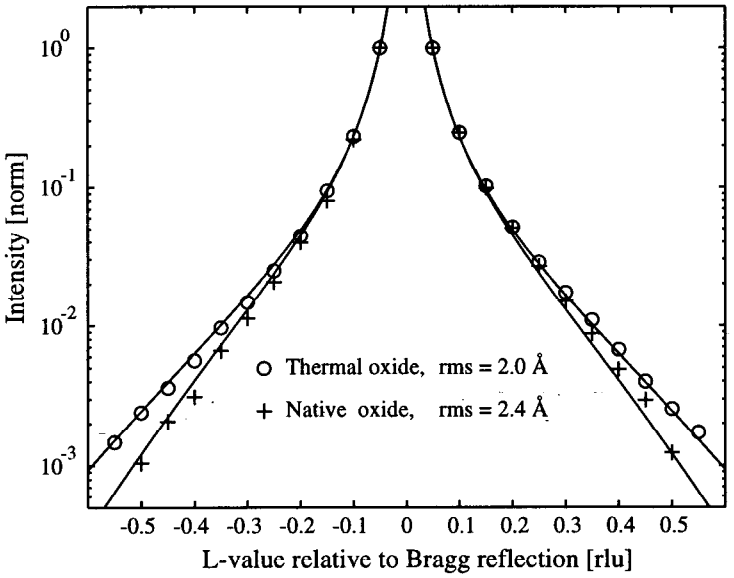

Figure 4.4: (202) Crystal truncation rod intensities of both native and thermal oxide samples cleaned with ammonia at full strength (wafer set A). The data are shown as symbols. The solid lines represent the best simultaneous fit to both sides.

as little as 60 Å of thermal oxidation.

In a dry oxidation process, the wafer is exposed to an oxygen rich atmosphere whereas a wet oxidation corresponds to an atmosphere with a high water content. Both thermal oxidation processes are typically carried out at 750-1000°C. The wet process causes a more rapid oxidation of the silicon and is therefore commonly used for thicker oxides, whereas the dry process is used for gate oxides, which are of the order of 50-80 Å thick. The roughness of the Si-SiO_2 interface was investigated after thermal oxidation of a 60 Å film using both a dry and a wet process. The CTR data are shown in Figure 4.5. The rod intensities for the two wafers are indistinguishable, and the roughness of the interface is therefore the same. Fitting both sides of the rod simultaneously to the modified Andrews & Cowley theory, an rms roughness of 2.1 Å

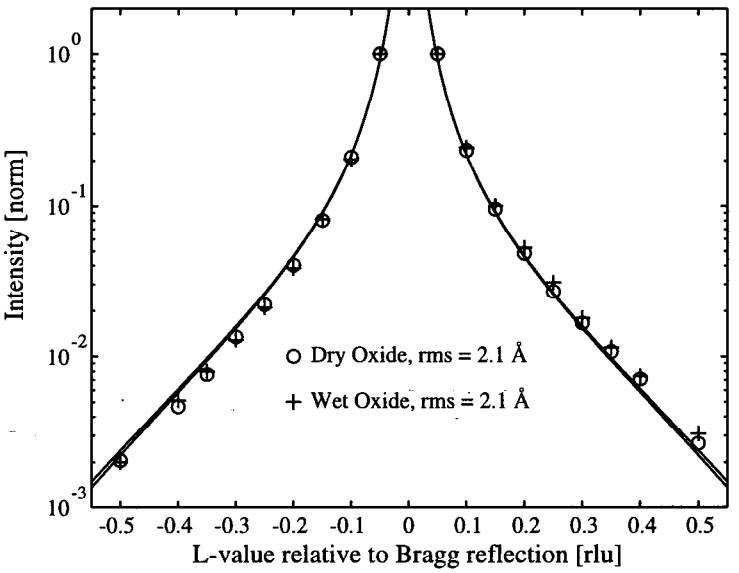

Figure 4.5: (202) rod intensities of a wet and a dry 60 Å thermally grown oxides on Si(001).

is obtained.

4.4.3 Influence of Cleans

In Figure 4.6 the CTR's of all 3 sets are shown for the wafers containing a 60 Å thermally grown oxide. The best fit to both sides of the (202) Bragg reflection is shown as solid lines. The wafer from set C has an rms roughness of 2.7 Å whereas the wafers from sets A & B both yield an rms value of 2.0 Å. The roughness values extracted from the CTR measurements for both the native and thermal oxide samples are also listed in Table 4.1. The roughnesses obtained using CTR scattering are in the range 2.3-3.2 Å for the native oxide wafers and 2.0-2.7 Å for the wafers terminated by a thermal oxide. Interfacial smoothing due to thermal oxidation is seen for all three wafer sets. As confirmation of the theoretical prediction described above, that

the roughness should be independent of the reflection, the (311) rod was measured for the thermal oxide from wafer set A. The rms roughness for this wafer is 2.1 Å. Within the precision of our measurements, these values are the same.

The results from both AFM and CTR techniques show that both concentrations of ammonium hydroxide result in the same roughness and that either concentration of ammonium hydroxide results in a smoother interface than that of the wafer processed with hot water. The x-ray scattering results also show a smoothing of the interface as a result of the oxidation process.

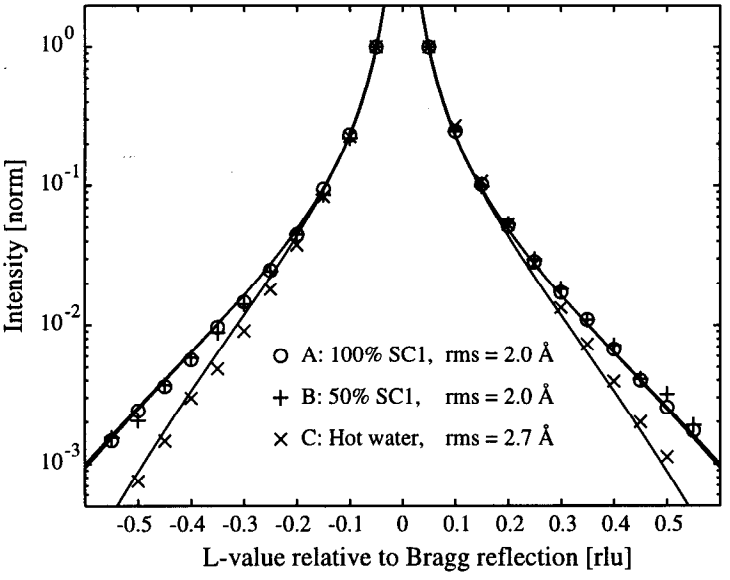

Figure 4.6: (202) Crystal Truncation rod intensities of all three thermal oxide samples exposed to different cleans. The best simultaneous fit to both sides of the Bragg reflection is shown as solid lines.

4.5 Atomic Force Microscopy

The surface roughness of wafers terminated by a native oxide was measured using AFM. These AFM measurements were done by Elizabeth C. Carr of Hewlett Packard Laboratories. For these same wafers, the interfacial roughness was also measured by CTR scattering (see above). Both techniques obtain similar although not identical results. As will be discussed below, the differences in measured roughness between the two techniques can be explained in part by the difference in the lateral length scale probed.

4.5.1 Experimental

The AFM measurements were carried out in air using a Digital Instruments Nanoscope III operating in Tapping Mode. Images were acquired on 1x1μm areas having 512x512 data points. After correcting for artifacts in the piezoelectric scanner, the rms roughness was calculated for each image. Since silicon wafers exposed to air form a native oxide, AFM probes the surface morphology of this oxide.

4.5.2 Results

The AFM images show no ordered features, so the height distribution was extracted from the images and is shown in Figure 4.7. The top of the figure shows the normalized height distributions for the three native oxide wafers and a pure Gaussian fit through each. The Gaussian fit is very good for all three, indicating that our use of a Gaussian fit to the x-ray scattering data is appropriate. The lower part of Figure 4.7 shows the three data sets plotted on the same scale. The native oxide wafers from sets A & B, treated with the SC1 bath, are indistinguishable, whereas the distribution of heights from the native oxide of wafer set C (hot water treatment) is clearly broader. The rms roughness derived from these data are 0.9 Å for the SC1-treated wafers and 2.7 Å for the wafer treated with hot water, as shown in Table 4.1.

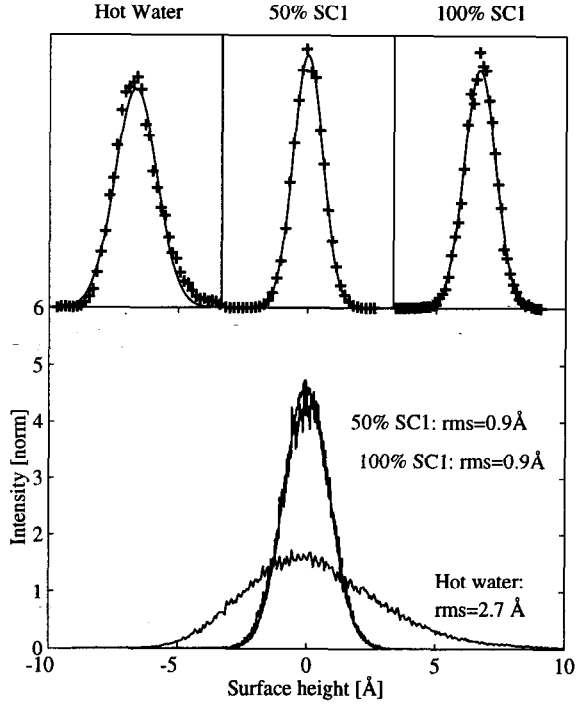

Figure 4.7: Height distribution functions of the wafers terminated by a native oxide extracted from the AFM images. The upper set of figures show the normalized distribution fitted to pure Gaussian functions. The horizontal scale is different for the three curves. The lower figure shows the same three sets of data on the same horizontal scale to show relative width. The same number of pixels are present in each image, so the larger width of the hot water-treated sample results in a lower peak height. Note that the curves from the two wafers treated with SC1 are nearly indistinguishable.

Samples		AFM	CTR
Cleaning	Oxide	[Å]	[Å]
A: 100 % SC1	Native	0.9	2.4
	Thermal		2.0
B: 50 % SC1	Native	0.9	2.3
	Thermal		2.0
C: Hot water	Native	2.7	3.2
	Thermal		2.7

Table 4.1: RMS roughness in Å of the Si-SiO_2 interface obtained with Crystal Truncation Rod (CTR) scattering from the (202) rod. Atomic Force Microscopy (AFM) was used to measure the roughness of the native oxide surface as well. The wafers went through different cleaning procedures (see text).

4.5.3 Lateral roughness scale

Lateral length scale limits of the roughness probed exist for AFM similar to those of CTR scattering. For etched Si AFM tips the minimum lateral dimension that can be resolved is approximately 100 Å due to the diameter of the scanning tip. Note that the sensitivity of AFM to vertical variations is sub-Angstrom. The large length limit for an AFM image is the size of the scan. For a 100 Å diameter tip, several pixels recorded per tip diameter and 512 pixels per line, the image size is $\sim 1\mu m^2$. Larger areas can be scanned with pixel-limited rather than tip-diameter-limited resolution. Although it produces a real-space image of the surface, the in-plane length scales of roughness measured by AFM can be extracted. A measure of the height difference between two points on the surface separated by a distance r can be defined as [54, 57]:

$$g(\vec{r}) = < [z(\vec{r}) - z(0)]^2 > \tag{4.14}$$

where $z(\vec{r})$ is the surface height at r. The average is taken over all pairs of points on the surface separated by a distance r. For separations below which the surface is flat $g(\vec{r})$ is zero (and $g(\vec{r}) = 0$ at $r = 0$). At the largest separation in the measurement $g(\vec{r}) = 2\sigma^2$, where σ is the rms roughness of the surface. The radial separations at which the transition between zero and $2\sigma^2$ occurs correspond to the wavelengths of the roughness.

$g(\vec{r})$ is shown in Figure 4.8 for the wafer treated with the full concentration of

ammonium hydroxide (wafer set A) and terminated by a native oxide. At length scales larger than 200 Å the curve is essentially flat, thus showing that the majority of the roughness measured by AFM occurs at length scales below 200 Å. The rising slope of $g(\vec{r})$ at small r suggests that the wafer is rough at wavelengths below the diameter of the tip. At length scales shorter then the tip diameter (100 Å) the measured roughness includes contributions from the tip shape, which tend to represent the surface as smoother than it actually is. The AFM results suggest that a large part of the surface roughness is occurring at in-plane separations which are similar in size or smaller than the tip diameter.

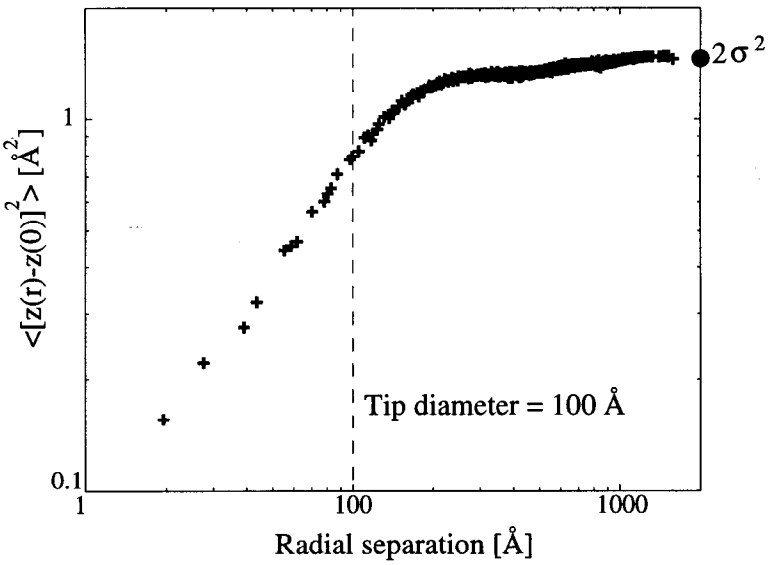

Figure 4.8: The average height-difference squared is shown for the wafer terminated by a native oxide and treated by the full amount of ammonia. The curve is derived from the AFM data. At large separation distances the curves approaches $2\sigma^2$, where σ is the rms value of the image. The plateau starting at r=200 Å shows that a majority of the roughness has an in-plane length scale of less than 200 Å. The vertical dotted line corresponds to the tip diameter of 100 Å.

4.5.4 Comparison to CTR scattering

Comparison of the two techniques show an overall agreement in the relative roughness, i.e. that the wafer exposed to hot water has a considerably higher roughness than those treated with the SC1 bath. However, the absolute roughness values obtained from the two techniques are significantly different. There are at least two reasons why this might occur. The first is that the AFM measurement measures the roughness of the top surface of the native oxide, whereas the CTR scattering measures the roughness of the interface between the bulk silicon and the native oxide. Thus the consistency of the AFM and x-ray scattering results depends on the native oxide exhibiting the same morphology at its two surfaces, i.e. the native oxide has a uniform layer thickness. The native oxide can be quite thin (~5 Å) [7], but may be sufficient to result in some smoothing. However, using UHV-STM and AFM, other groups have reported that the surface morphology of the native oxide resembles that of the clean silicon surface [58] and the steps at the silicon surface are visible on the oxide surface as well [59]. This suggests that the native oxide is conformal and that an AFM measurement of the top surface should be a good representative of the interface.

The second factor which could cause the discrepancy between the two measurements is the difference in length scales to which the two techniques are sensitive. As discussed above, for the AFM measurement the length scale ranges from ~1 μm down to ~100 Å. Roughness with an in-plane correlation larger than that resolvable by the instrument resolution will not contribute to the rms roughness measured by CTR scattering. The coherent scattering length likewise puts an upper limit on the lateral roughness sensitivity, since scattering from the parts of the surface which are further apart than the in-plane coherence will add up as intensities rather than as phases. Any information about roughness correlations are thereby lost.

The length scale of this CTR measurement, ranging from the incident wavelength (~1.2 Å) up to half a micron, includes the length scales probed by the AFM measurement and significantly shorter wavelengths as well. Our measurements are consistent with a surface on which the roughness is predominantly at short length scales, perhaps even atomic length scales. In this case the AFM measurements would show a lower roughness than the CTR measurements, as we observe. Our conclusion

that the interfacial roughness is predominantly short range is supported by Evans-Lutterodt *et al.* [37], who were unable to resolve long wavelength roughness even with the use of a diffracted beam monochromator. The height-height correlation function of the AFM image also shows that a substantial part of the roughness occurs at a separation of less than 100 Å. Thus, the difference in rms roughness measured by the two techniques can be explained by the length scales at which the two techniques are sensitive.

This tends to reinforce the conclusion that the difference in surface roughness measured by AFM and CTR scattering is due to the shorter minimum lateral correlation length of the x-ray technique.

Chapter 5

Miscut

Summary

In this chapter a theory describing the scattering from a miscut crystal surface is developed for both a single cubic and a diamond cubic lattice using the layer summation method. Crystal Truncation Rods (CTR's) are shown to be perpendicular to the surface and not along the crystallographic axes of a miscut crystal. It is shown that for a crystal terminated by a regular step array both an atomistic and a continuum description of CTR scattering give identical results. Furthermore, the atomistic approach is used to show that a diamond cubic surface with a miscut is inherently rough. Even for a small miscut the tilt of the CTR with respect to the crystallographic axes results in complications for measuring the rod intensity. Schemes are presented for determining the exact position of the CTR in reciprocal space and for measuring the miscut of a single crystal. These methods were applied to the measurement of CTR intensities of silicon(001) wafers with miscuts of 0.1 and 4 degrees.

5.1 Introduction

Silicon(001) wafers typically have a miscut of 1/10 degree, which for an ordered step array with single layer steps corresponds to terrace widths of ~780 Å. Even this small a miscut has an influence on the direction of the CTR. As will be shown below, the rod is perpendicular to the surface, so if there is a miscut, no matter how small, the CTR does not follow the principal crystallographic direction, but tilts in such a way that it is perpendicular to the surface. Each Bragg peak has a CTR associated with it. For the case of a surface normal perfectly aligned with a principal crystallographic direction, the rods from each of the Bragg peaks would overlap, i.e. the (2,0,2), (2,0,6) and (2,0,$\bar{2}$) rods would all arrive at the surface at the (200) position). For a real crystal with miscut these rods do not coincide, but are parallel to each other. This separation between rods at the surface has been observed using grazing incidence x-ray scattering and used to evaluate the step distribution of GaAs [60].

Theoretical work on the scattering from stepped surfaces has been done by Lent *et al.* [61, 62]. The effect of miscut had been studied using electron diffraction for vicinal silicon (001) surfaces [63]. Monte Carlo simulations of the step distribution for surfaces in thermal equilibrium have also been done to aid the interpretation of diffraction data [64]. However, the influence of miscut has not been considered for crystal truncation rod scattering.

In this chapter it will be shown that both a theory based on global miscut as well as a theory based on an atomistic approach for describing the miscut of the crystal predict the same functional form for the decay of the CTR away from the Bragg position. It is shown for the atomistic case that the CTR's will remain perpendicular to the surface. It is also shown that the calculated intensity for a single rod from a regular step array is equal to that from a single rod for a flat surface, whereas a variation of the terrace length causes a decrease of the CTR intensity away from the Bragg peak. Such a decrease in intensity is also caused by surface roughness as discussed in Chapter 4.

Due to the tilt of the rods with respect to the crystallographic axes, it can be difficult to locate the exact rod position. The rod intensity is underestimated unless

the center of the rod is found and this underestimation can result in an incorrect value for the roughness. A scheme is presented for determining the exact position of the rod. This method was used to measure the CTR intensities of silicon(001) wafers with miscuts of 0.1 and 4 degrees. Even for a wafer with a 0.1 degree miscut the tilt between the rods and the crystallographic axis is large enough to cause a decrease in the rod intensity unless the rod position is correctly determined. A method is also provided for determining the size and direction of the miscut by measuring a symmetric reflection along two different azimuths of the crystal.

5.2 Theory

5.2.1 Continuum Model

Scattering from a crystal with a perfectly flat surface was discussed in detail in Chapter 2. It was shown that a crystal with a perfectly flat surface can be described in terms of an infinite lattice multiplied by a shape function which is unity where the crystal exists and zero elsewhere. Using this model, Andrews and Cowley [16] showed that the intensity for a semi-infinite crystal is given by:

$$I = \sum_{\vec{\tau}} \frac{|\rho_0(\vec{\tau})|^2}{q_\perp^2}, \tag{5.1}$$

where ρ_0 is the average electron density of the crystal. Let $\vec{Q}$ be the total scattering vector and $\vec{q}$ the momentum transfer relative to the Bragg reflection $\vec{\tau}$ ($\vec{Q} = \vec{\tau} + \vec{q}$). Then $\vec{q}_\perp$ corresponds to the reduced scattering vector, which is the momentum transfer of the Bragg reflection perpendicular to the surface. Thus rods of intensity with a $1/q_\perp^2$ dependence in the direction of the surface normal are associated with each Bragg peak in reciprocal space. For a crystal surface exactly along a crystallographic direction, rods from Bragg peaks with identical in-plane momentum transfer overlap, e.g. for the case of silicon (001), the $(20\bar{2})$, (202), (206) etc. rods, the resulting CTR intensity is given by the sum over those individual rods.

The presence of a miscut will rotate the shape function (which is a Heaviside function in the case of a perfectly flat crystal) with respect to the crystallographic

axes, so that the shape function is in the direction of the surface normal. A Fourier transform of such a system is equivalent to a convolution of the reciprocal lattice with that of the Fourier transform of the Heaviside function. Since the Heaviside function is in the direction of the surface normal, then so will the Fourier transform. Thus, the crystal truncation rods associated with each Bragg peak are simply rotated with respect to the crystallographic axes to be normal to the surface of the crystal. Rods from Bragg peaks with the same in-plane (crystallographic) momentum transfer remain parallel, but they no longer overlap. The intensity along the CTR is therefore not given by the sum over all the rods, but directly by the intensity from the rod arising from the Bragg peak being probed:

$$I = \frac{|\rho_0(\vec{\tau})|^2}{q_\perp^2}. \tag{5.2}$$

Note, that this expression is the same as for a surface which is just slightly rough, as was discussed in Chapter 4. Thus, if a surface is miscut or has some roughness, then the total CTR intensity is dominated by intensity from the rod associated with the nearest Bragg peak.

5.2.2 Atomistic Model

An atomistic model was used by Robinson [17] in order to calculate the rod intensity. This layer summation method was presented in Chapter 2, where the rod intensity was calculated by adding up the structure factor for all the atoms in the crystal. Consider a perfectly flat crystal with a simple cubic lattice, which is terminated along the [001] direction. The rod intensity, at integer values of h and k, was shown to be:

$$I = |f_0|^2 N_1^2 N_2^2 \frac{1}{2\sin^2(\pi l)}, \tag{5.3}$$

where f_0 is the atomic form factor and N_1 and N_2 correspond to the number of unit cells in the crystal along the in-plane crystallographic directions.

To see the effect of miscut on this atomistic formalism, it is clearest to demonstrate for a simple cubic lattice. In Appendix B the more complicated (and more useful) case of a diamond cubic lattice is developed. Consider a simple cubic lattice with a

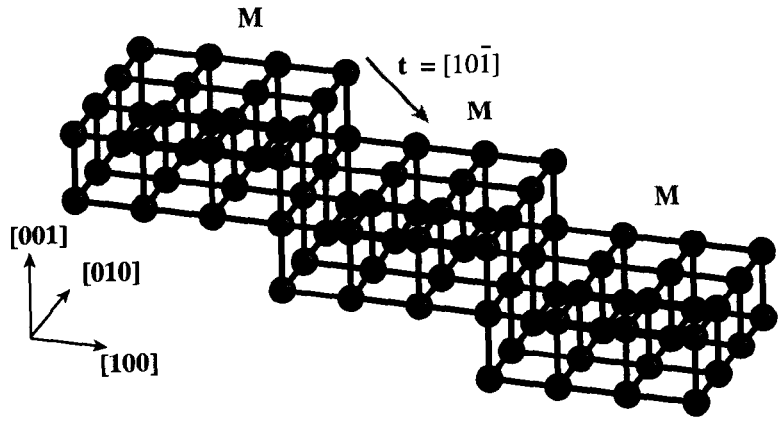

Figure 5.1: Schematic of a simple cubic crystal with a regular step array. The miscut is along the [100] direction of the lattice consisting of N_t terraces of M unit cells. $\vec{t}$ is the translation vector from the end of one terrace to the beginning of the next.

miscut m in the [100] direction as shown in Figure 5.1 with a regular array of terraces (the width of all the terraces are the same). Let the miscut crystal be terminated by N_t terraces each consisting of M unit cells in the miscut direction. Thus the crystal has $N_1 = MN_t$ unit cells in the [100] direction, N_2 unit cells in the [010] direction and N_3 unit cells in the [001] direction. It is convenient to describe the step array as a stacking of planes which are perpendicular to the [100] direction. The structure factor for a single plane is:

$$F_{plane} = f_0 \sum_{j_2=0}^{N_2-1} e^{2\pi i k j_2} \sum_{j_3=0}^{N_3-1} e^{2\pi i l j_2} = f_0 \left(\frac{e^{2\pi i k N_2} - 1}{e^{2\pi i k} - 1} \right) \left(\frac{e^{2\pi i l N_3} - 1}{e^{2\pi i l} - 1} \right). \tag{5.4}$$

The structure factor for the whole crystal is given by summing over the planes of a terrace, then over all the terraces. Because it is a simple cubic lattice, the translation vector from the end of one terrace to the beginning of the next $\vec{t}$ is given by [10$\bar{1}$].

$$\begin{aligned} F &= F_{plane} \sum_{j_1=0}^{M-1} e^{2\pi i h j_1} \sum_{j_s=0}^{N_t-1} e^{2\pi i (Mh-l) j_s} \\ &= f_0 \left(\frac{e^{2\pi i k N_2} - 1}{e^{2\pi i k} - 1} \right) \left(\frac{e^{2\pi i l N_3} - 1}{e^{2\pi i l} - 1} \right) \left(\frac{e^{2\pi i h M} - 1}{e^{2\pi i h} - 1} \right) \left(\frac{e^{2\pi i (Mh-l) N_t} - 1}{e^{2\pi i (Mh-l)} - 1} \right). \end{aligned} \tag{5.5}$$

The scattered intensity is given by:

$$I = |f_0|^2 \left(\frac{\sin^2(\pi k N_2)}{\sin^2(\pi k)}\right)\left(\frac{\sin^2(\pi l N_3)}{\sin^2(\pi l)}\right)\left(\frac{\sin^2(\pi h M)}{\sin^2(\pi h)}\right)\left(\frac{\sin^2(\pi(Mh-l)N_t)}{\sin^2(\pi(Mh-l))}\right). \quad (5.6)$$

The first two factors in the above equation are equivalent to those derived for a perfect crystal with no miscut. The first factor is a sum over the atoms in the k-direction, which for an infinite array yields a delta function for any integer of k. The second factor is a sum in the l-direction, which, because N_3 is finite, results in a decay of the scattering away from the Bragg reflection in the [001] direction. The third factor arises from summing over the atoms on each terrace and causes peaks at the integer positions in the [100] direction. Because M is relatively small, the envelope function in the h-direction is larger than in k or l. The larger the terraces (the smaller the miscut) the sharper these peaks are.

In equation 5.6 the last factor determines the tilt of the rod, i.e. the h and l values where the maximum intensity occurs. For the rod going through the Bragg reflection HKL, and for a given terrace width M, h is given by:

$$h = H + \frac{l-L}{M}, \quad (5.7)$$

or

$$l = M(h-H) + L. \quad (5.8)$$

M is the slope of the rod, and $l = L$ when $h = H$. Because a simple cubic cell is being considered, $-1/M$ is the slope of the surface, 1 cell down for each M cells across. Thus the rod is perpendicular to the surface. Inserting equation 5.7 into equation 5.6 gives the intensity along the rod as a function of l only:

$$I_{ctr} = |f_0|^2 N_t^2 N_2^2 \left(\frac{\sin^2(\pi l N_3)}{\sin^2(\pi l)}\right)\left(\frac{\sin^2(\pi(HM+l-L))}{\sin^2(\pi(H+(l-L)/M))}\right), \quad (5.9)$$

since M, H and L are all integers, the equation can be further simplified to:

$$I_{ctr} = |f_0|^2 N_2^2 N_t^2 \left(\frac{1}{2\sin^2(\pi l)}\right)\left(\frac{\sin^2(\pi l)}{\sin^2(\pi(l-L)/M)}\right) = \frac{|f_0|^2 N_2^2 N_t^2}{2\sin^2(\pi(l-L)/M)}. \quad (5.10)$$

Since $\sin^2(x)$ can be approximated as x^2 for small values of x, then the rod profile can be written as:

$$I_{ctr} = |f_0|^2 \frac{N_2^2 N_t^2 M^2}{2\pi^2(l-L)^2}. \tag{5.11}$$

It was shown earlier that the layer summation method for a crystal without miscut yields a scattered intensity which is proportional to $1/\sin^2(\pi l)$ which corresponds to the sum of $1/q_\perp^2$ for all the Bragg peaks at that in-plane momentum transfer. However, for a miscut surface the rod intensity is directly given by $1/q_\perp^2$, where $q_\perp$ refers to the closest Bragg peak. Physically, the rods are all rotated around their associated Bragg point by the size of the miscut, so that all the rods stay perpendicular to the surface. Since there is no longer overlap, the CTR intensity is that of each rod individually. This agrees with the prediction of the continuum approach.

Extending the theory to an arbitrary direction of miscut does not alter the intensity of the rods or their position in reciprocal space. Appendix B is the derivation of the scattered intensity of a regular step array on the surface of the diamond cubic lattice of silicon. However unlike the CTR intensity from a simple cubic lattice with a regular step array, where the intensity equals that of a single rod on a surface without miscut, the intensity from a single rod for the miscut diamond cubic crystal is less than that from a flat crystal. Thus, a miscut crystal with a diamond cubic lattice is inherently rough. To appreciate why this is so, consider a simple cubic crystal with two terrace widths.

The influence of a variation of terrace length on the CTR intensity can be studied by examining the scattering from a step array with a period of two terraces of width M_1 and M_2 unit cells, respectively. For a crystal consisting of N_t terraces with $2M$ unit cells per bi-terrace ($2M = M_1 + M_2$) the structure factor is:

$$\begin{aligned} F &= F_{plane}\left(\sum_{j_1=0}^{M_1-1} e^{2\pi i h j_1} + e^{2\pi i(hM_1-l)}\sum_{j_2=0}^{M_2-1} e^{2\pi i h j_2}\right)\sum_{j_s=0}^{N_t/2-1} e^{2\pi i(2Mh-2l)j_s} \\ &= F_{plane}\left(\frac{e^{2\pi i h M_1}-1}{e^{2\pi i h}-1} + e^{2\pi i(hM_1-l)}\frac{e^{2\pi i h M_2}-1}{e^{2\pi i h}-1}\right)\left(\frac{e^{2\pi i(Mh-l)N_t}-1}{e^{4\pi i(Mh-l)}-1}\right). \end{aligned} \tag{5.12}$$

The step height is assumed to be one unit cell as in the case of the regular step array.

The intensity is then given by:

$$I = |f_0|^2 \frac{\sin^2(\pi k N_2)}{\sin^2(\pi k)} * \frac{\sin^2(\pi l N_3)}{\sin^2(\pi l)} * \frac{I_{bracket}}{4\sin^2(\pi h)} * \frac{\sin^2(\pi(Mh-l)N_t)}{\sin^2(2\pi(Mh-l)}, \quad (5.13)$$

where

$$\begin{aligned} I_{bracket} &= \left(e^{2\pi i M_1 h} - 1 + e^{2\pi i(2Mh-l)} - e^{2\pi i(M_1 h - l)}\right) \cdot ComplexConjugate \\ &= 4 - 2\cos(2\pi M_1 h) - 2\cos(2\pi M_2 h) - 2\cos(2\pi(2Mh-l)) - \\ &\quad 2\cos(2\pi l) + 2\cos(2\pi(M_1 h - l)) + 2\cos(2\pi(M_2 h - l)) \\ &= 4\left(\sin^2(\pi M_1 h) + \sin^2(\pi M_2 h) + \sin^2(\pi(2Mh-l)) + \right. \\ &\quad \left. \sin^2(\pi l) - \sin^2(\pi(M_1 h - l)) - \sin^2(\pi(M_2 h - l))\right). \end{aligned} \quad (5.14)$$

The first, second and last products in equation 5.13 are identical to that of a regular step array (see equation 5.6). Therefore the rod is oriented in the direction perpendicular to the surface of the crystal as expected. As in the case of a regular step array, the intensity along the rod can be examined by inserting the following condition on h, where HKL is the Bragg reflection associated with the rod:

$$h = H + \frac{2(l-L)}{M_1 + M_2} = H + \frac{(l-L)}{M}. \quad (5.15)$$

Note the similarity between equation 5.15 and 5.7, where M in the equation above corresponds to average terrace width, whereas M in equation 5.7 is the exact terrace width. Thus, the rod intensity as a function of l for a bi-terrace structure is given by:

$$\begin{aligned} I_{ctr}^{2step} &= |f_0|^2 N_t^2 \left(\frac{\sin^2(\pi k N_2)}{\sin^2(\pi k)}\right)\left(\frac{\sin^2(\pi l N_3)}{\sin^2(\pi l)}\right)\left(\frac{1}{\sin^2(\pi(H + (l-L)/M))}\right) \\ &\quad \left(\sin^2(\pi(HM_1 + (l-L)\frac{M_1}{M})) + \sin^2(\pi(HM_2 + (l-L)\frac{M_2}{M})) + \right. \\ &\quad \sin^2(\pi(2HM + l - 2L)) + \sin^2(\pi l) - \sin^2(\pi(HM_1 + (l-L)\frac{M_1}{M} - l)) - \\ &\quad \left. \sin^2(\pi(HM_2 + (l-L)\frac{M_2}{M} - l))\right). \end{aligned} \quad (5.16)$$

Since M_1, M_2, M, H and L are all integers, the equation can be written as:

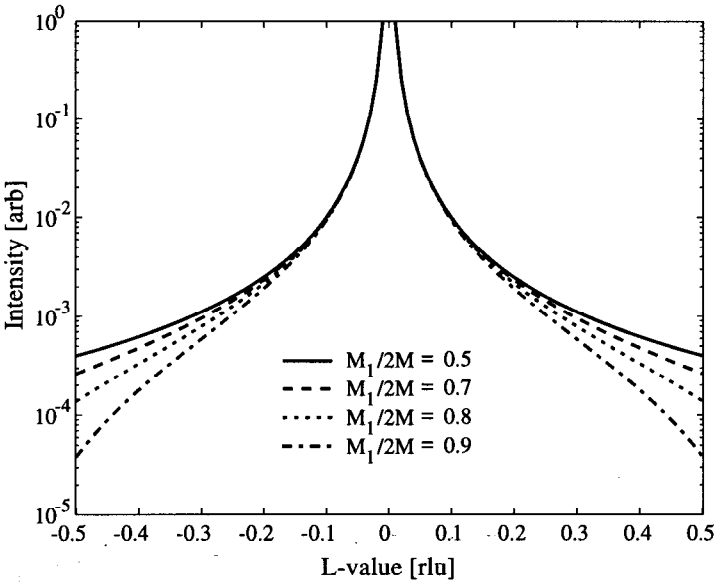

Figure 5.2: CTR intensity for a simple cubic crystal terminated by a bi-terrace array. The width of the bi-terrace is constant at 100 unit cells ($2M = M_1 + M_2 = 100$). The curves represent the calculated intensity for different ratios of unit cells on one terrace (M_1) to the total number of unit cells on a bi-terrace ($2M = M_1 + M_2$). The solid curve corresponds to the CTR intensity of a regular step array ($M_1 = M_2 = 50$).

$$I_{ctr}^{2step} = |f_0|^2 N_t^2 N_2^2 \left(\frac{1}{4\sin^2(\pi l)}\right)\left(\frac{1}{\sin^2(\pi(l-L)/M)}\right)\Big(\sin^2(2\pi(l-L)\frac{M_1}{M})+ \sin^2(2\pi(l-L)\frac{M_2}{M}) + 2\sin^2(\pi l) - \sin^2(\pi(2(l-L)\frac{M_1}{M} - l)) - \sin^2(\pi(2(l-L)\frac{M_2}{M} - l))\Big). \quad (5.17)$$

In the limit of a perfect step array $M_1 = M_2 = M$, the products which contain either M_1 or M_2 drop out of equation 5.17 and it reduces to equation 5.10, which is the rod intensity for a regular step array. However if M_1 is not equal to M_2 a decrease in the intensity occurs. This is shown in Figure 5.2, where the CTR intensity is plotted for different terrace width combinations. All the curves shown correspond to the same miscut of 0.57 degree ($M_1 + M_2 = 100$) . For a regular step array ($M_1 = M_2$) the fall off goes as $1/q^2$, however as the difference in terrace width increases, the intensity

drops faster, i.e. the surface is rougher. The CTR intensity for a miscut diamond cubic crystal (Appendix B) is less than that of a flat crystal due to the two types of surface termination of the silicon lattice in the [001] direction. The closest one can find to a regular step array on the (001) surface is for one terrace length to be different from the other by 1/2 a unit cell.

5.3 CTR Position

In order to determine the intensity of the CTR accurately, the exact position of the CTR needs to be found. As described in the theory section, when a miscut is present the rod is tilted with respect to the crystallographic axis. Since the width of the rod is small and the intensity is low, it is not an easy task to determine its exact location in reciprocal space.

The orientation of the crystal with respect to the diffractometer is determined by finding several Bragg peak positions. Using a standard four-circle diffractometer with the crystal surface normal aligned along the ϕ-axis, the Bragg peaks are found by sequentially scanning θ and χ until a global maximum is reached, with θ being the scattering angle and χ the rotation of the sample about the normal to the scattering plane [46]. Compatible methods can be used for other types of diffractometers. An orientation matrix can be derived from the angular positions of the Bragg peaks which translates diffractometer angles into the reciprocal lattice of the crystal. However, the rod position cannot be found directly using this crystal orientation matrix due to the tilt of the rods with respect to the crystallographic axis.

Due to the extended nature of the CTR one cannot find the maximum of the rod at a particular l-value by using the same approach employed to locate a Bragg peak. Neither θ nor χ scans are orthogonal to the rod, so sequentially scanning those angles will inevitably change the l-value towards that of the Bragg peak. Rather than operating in angle space and scanning single motors, one must scan along axes in reciprocal space using multiple motors simultaneously. Consider a cubic crystal with the surface normal approximately along the [001] direction. By scanning sequentially in the h and k-direction at a constant l-value, the maximum intensity of the rod

is found for that l-value, thus ensuring that the center of the rod is located for a specific out-of-plane momentum transfer away from the Bragg peak. An example of this procedure is presented in the results section below. If the size and direction of the miscut is known, the position of the rod can be calculated. However since the CTR is a very sharp feature parallel to the surface, such a calculation is only approximate and it is still necessary to perform the h and k scans in order to locate the exact rod position.

5.4 Determination of Miscut

There are several ways to determine the size and direction of the miscut of a single crystal. One method is to measure a reflection which is nominally along the surface normal for two azimuthal orientations. For the Si(001) wafers used in this study, the (004) angular position was determined for two in-plane directions which are separated by 90 degrees. For the two in-plane angles, known as ϕ, the reflection is maximized by scanning χ and θ, iteratively. From these two sets of three angles the miscut can be derived.

Let m be the miscut defined as the angle between the surface normal $\vec{n}$ and the crystallographic axis [001]. The miscut vector $\vec{m}$ lies in the surface and is pointed down steps. The miscut along the scattering direction measured in a direction ϕ degrees away from this miscut direction is the effective miscut in that direction:

$$m^{\parallel}_{eff}(\phi) = m\cos(\phi). \tag{5.18}$$

The effective miscut $m^{\parallel}_{eff}$ in the scattering direction is identical to the tilt in θ which brings the reflection into the diffraction condition along that azimuth. Analogously, one can define an effective miscut in the direction perpendicular to the scattering vector.

$$m^{\perp}_{eff}(\phi) = m\sin(\phi). \tag{5.19}$$

The effective miscut in this direction corresponds to the tilt in χ which will bring the Bragg reflection into its diffraction condition. Thus the two equations above can be

written as:

$$\theta = m\cos(\phi) \tag{5.20}$$

$$\chi = m\sin(\phi), \tag{5.21}$$

where θ and χ corresponds to the deviation from the nominal values of the reflection ($\theta_0 = \theta_{Bragg}, \chi_0 = 90$ degrees). Let $\chi_i + \chi_0$ and $\theta_i + \theta_{Bragg}$ be the angular positions for the same symmetric reflection at two different angle settings (i=1,2) separated by the in-plane angle $\Delta\phi$. An offset of the absolute values of χ and θ from the diffractometer angles are included as $\Delta\chi$ and $\Delta\theta$. From the above equations the miscut of the crystal can be expressed as:

$$\begin{aligned} m &= \left.\frac{\chi_1 + \Delta\chi}{\sin\phi_0}\right|_{\theta=\theta_1} = \left.\frac{\chi_2 + \Delta\chi}{\sin(\phi_0 + \Delta\phi)}\right|_{\theta=\theta_2} \\ &= \left.\frac{\theta_1 + \Delta\theta}{\cos\phi_0}\right|_{\chi=\chi_1} = \left.\frac{\theta_2 + \Delta\theta}{\cos(\phi_0 + \Delta\phi)}\right|_{\chi=\chi_2}, \end{aligned} \tag{5.22}$$

where ϕ_0 is the in-plane angle between the miscut direction and the first reflection. Solving this system of equations yields the offset of the diffractometer angles and the direction of the miscut:

$$\Delta\chi = \frac{(cos\Delta\phi - 1)(\chi_1 + \chi_2) + \sin\Delta\phi(\theta_1 - \theta_2)}{2(1 - \cos\Delta\phi)} \tag{5.23}$$

$$\Delta\theta = \frac{(cos\Delta\phi - 1)(\theta_1 + \theta_2) + \sin\Delta\phi(\chi_2 - \chi_1)}{2(1 - \cos\Delta\phi)} \tag{5.24}$$

$$\phi_0 = \arctan\left(\frac{\chi_1 + \Delta\chi}{\theta_1 + \Delta\theta}\right). \tag{5.25}$$

Inserting these values into equation 5.22 gives the size of the miscut. The analysis above can be simplified by measuring the reflections along two perpendicular azimuths ($\Delta\phi = 90$ degrees). In that case the miscut m and its azimuthal direction ϕ_0 simplifies to:

$$m = \sqrt{(\theta_1 - \theta_2)(\chi_2 - \chi_1)} \quad , \Delta\phi = 90° \tag{5.26}$$

$$\phi_0 = \arctan\left(\frac{\theta_1 - \theta_2 + \chi_1 - \chi_2}{\theta_1 - \theta_2 - \chi_1 + \chi_2}\right) \quad , \Delta\phi = 90°. \tag{5.27}$$

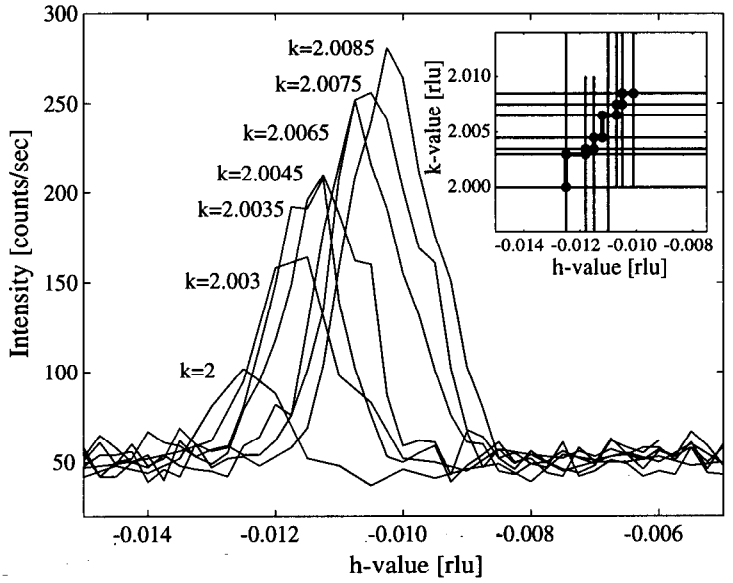

Figure 5.3: Intensities for a series of h-scans through the (022) rod at l=1.8. The rod position was determined using alternate scans along the h and k-direction at a constant l-value. The insert shows the traces of the scans. The horizontal and vertical lines corresponds to the h and k-scans, respectively. The maximum of each scan is identified by a large solid circle.

5.5 Experimental Results

In order to investigate the influence of miscut on CTR scattering, two silicon(001) wafers with different miscuts were examined: one with a 4 degree miscut and one with a 0.1 degree miscut. The 4 degree miscut sample is terminated by a 110 Å thermal oxide, whereas the other wafer is capped by a 60 Å thermal oxide. This variation in film thickness does not influence the CTR, as the CTR is unaffected by an amorphous layer.

5.5.1 202 rod

A series of h-scans is shown in Figure 5.3, which were performed in order to locate the rod position at l=1.8 of the (022) rod. The sample is the Si(001) wafer with a ~4 degree miscut. The curves show an increase in rod intensity by a factor of five

after subtraction of the background from the the first to the last curve. The insert in the figure shows the trace of the h and k-scans in reciprocal space done in order to locate the rod position at $l = 1.8$ of the CTR associated with the (022) reflection. The horizontal lines represent the h-scans, which are the curves shown in the main part of the figure. The vertical lines correspond to the k-scans, which were done between each of the h-scans. The dots are placed at the maximum intensity of the scan. The CTR location at $l = 1.8$ was determined to be at h=-0.0101 and k=2.0085, which is 0.0132 rlu away from the nominal rod position corresponding to a tilt of the rod of 3.8 degrees with respect to the [001] direction. Because a θ-scan is nearly the same as a k-scan for the (202) rod, it is clear from these scans that a θ-rocking curve at the integer position is not sufficient for determining the CTR intensity, as such a procedure would result in a lower rod intensity than is actually present.

Figure 5.4 shows the intensities of the rods associated with the $< 202 >$ type reflections of the Si(001) wafer with a $\sim$4 degree miscut. The 202 and 022 rods probed are separated by 90 degrees. Figure 5.4a shows the intensity obtained using our traditional method of doing a single θ-rocking curve at the integer position. Due to the miscut and, therefore, the tilt of the rod with respect to the crystallographic axis, the full intensity of the rod is not measured. As rocking curves are performed further away from the Bragg peak, the deviation between the rod position and the crystallographic axes increases, i.e. the amount of the rod measured decreases as a function of the distance to the Bragg reflection. This is seen as the asymmetry of the measured intensity. By rotating the sample by 90 degrees and measuring an equivalent rod, the asymmetry of the rod has changed direction. In Figure 5.4b the intensity of the rod is shown when the position of the rod is properly determined using h and k-scans as described above. Fitting the (022) rod results in a 2.3 Å rms value for the low side of the rod and 2.4 Å for the high side, however this difference is within the estimated errorbars of $\pm$ 0.1 Å.

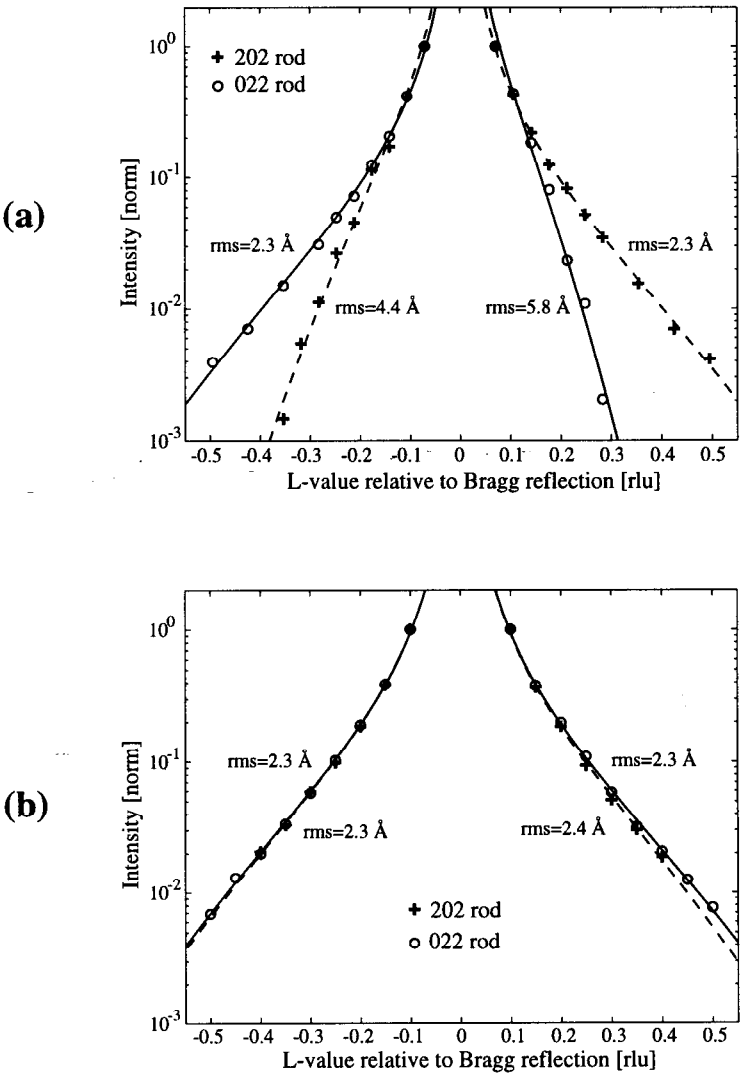

Figure 5.4: (a) X-ray scattering intensities ('+' and 'o') and fits for the (202) and (022) rods from a Si(001) wafer terminated by 110 Å thermal oxide with a 4 degree miscut. The asymmetry in the rod intensities and the reversal of that asymmetry are a result of the incorrect method of determining the CTR position. (b) shows rod intensities from the same rods using our new method for determining CTR position. The symmetric shapes indicate the rod position was properly tracked (see text for details).

5.5.2 311 rod

Although the tilt of the rod is directly proportional to the size of the miscut, for some rods one needs to be careful even for very small miscut. The CTR intensity was measured for the rods associated with both the (202) and (311) reflection of a silicon(001) wafer with a 0.1 degree miscut. Performing θ-rocking curves at the integer positions leads to a nice symmetric $(20l)$ rod intensity. The $(31l)$ intensity, however, shows strong asymmetry as presented in Figure 5.5. A fit to the low side of the rod yields an rms roughness of 4.2 Å, whereas the rms value extracted from the high side of the rod is 1.4 Å. Locating the exact rod position using alternating h and k-scans before doing the θ-scan leads to a more symmetric rod profile (also shown in Figure 5.5). The fit to the low side of the rod gives an rms roughness of 2.1 Å and the fit to high side yield 2.3 Å. Fit to both sides of the 202 rod of the same wafer (not shown) yielded an rms roughness of 2.0 Å.

The discrepancy between the sensitivity of the (202) and (311) rod to the miscut can be explained by the instrument function of the experiment. As described in Chapter 3, the instrument function depends on the wavelengths passed by the monochromator, the divergence of the beam and the angular acceptance of the detector. In our experimental setup the shape of the instrument function is mainly dominated by the large angular acceptance of the detector: 8 mrad in the scattering plane and 2 mrad perpendicular to the scattering plane, which is a consequence of using the slit setting of Specht & Walker [49]. The angular acceptance results in a plane of allowed scattering vectors which is inclined with respect to the rod. This angle is equal to the incident angle α between the beam and the surface of the crystal. As the incident angle of the beam onto the sample is very small on the low side of the (311) rod, it is very easy to miss the rod. As an example, using 10 keV photons we find that α=3.3 degrees at (3,1,0.5), so the rod and the plane of the instrument function are almost parallel. In this case, the rod intercepts the plane of the instrument function over a very small range of θ values.

The total width w of the CTR as measured using a θ-rocking curve is a function of the horizontal angular acceptance of detector b and can be derived from equation

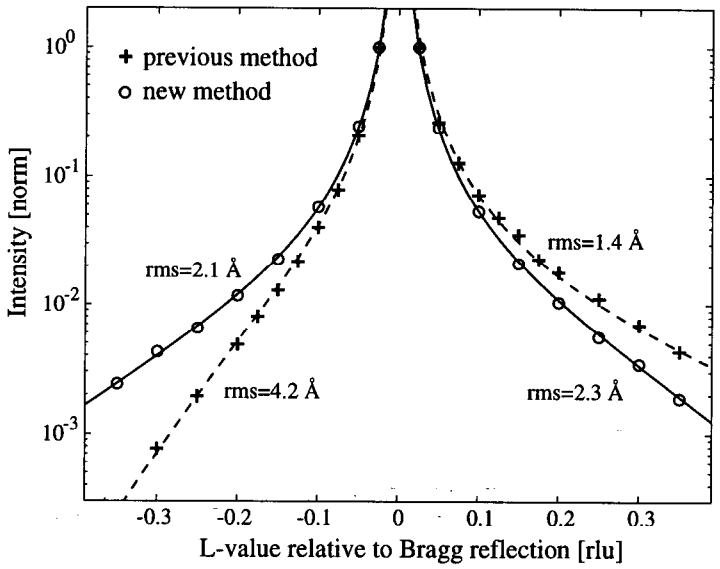

Figure 5.5: The scattered intensity from a (311) rod is presented for a Si(001) wafer terminated by a 60 Å thermal oxide with 0.1 degree miscut. The intensity obtained using our previous approach is shown as '+'s. The intensity measured with the scheme presented in this paper, is plotted as 'o's. The best fit to each side of the Bragg reflection is shown with dashes for our previous method and solid lines for the new method.

10 in [49] as:

$$w = \frac{b}{2}\frac{\tan\chi}{\cos\theta}. \tag{5.28}$$

As χ decreases, the rocking curve width does too. Figure 5.6 shows the width of the CTR as measured by a θ rocking curve vs. l-value for the 0.1 degree miscut wafer. The circles represent the (311) CTR data and the crosses the (202) CTR data. The solid lines are the best simultaneous fit to the data using equation 5.28, which corresponds to an acceptance of 3.0 mrad perpendicular to the diffraction plane. This derived angular acceptance is larger than the actual slit acceptance due to the convolution with the 2 mrad horizontal incident beam divergence. The (111) rod is also shown for comparison. The (311) rod has a very narrow rocking curve width, especially below the (311) reflection. This means that the rod is only in the diffraction

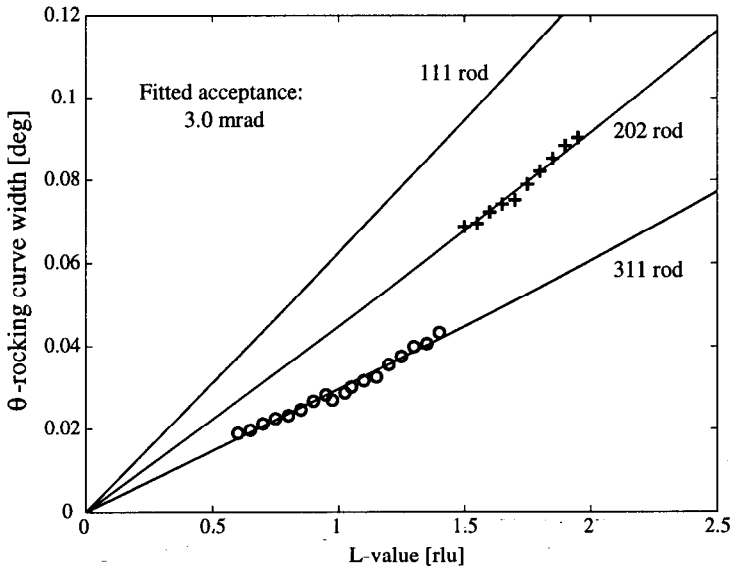

Figure 5.6: The full width of the CTR obtained from θ scans are plotted as a function of the l-value of the rod. The wafer is a Si(001) with a 0.1 degree miscut and is terminated by a 60 Å thermal oxide. The best simultaneous fit to both rods corresponds to an acceptance of the slits of 3.0 mrad in the direction perpendicular to the scattering plane and is shown as solid lines in the figure. For comparison the (111) rod is also shown.

condition over a very short angular range and thus it is difficult to probe the center of the rod. One should therefore be aware that even a very small miscut can influence the measured (311) CTR intensity and high accuracy in determining the rod position is essential for a valid intensity measurement. The (111) rod has a broader rocking curve width, but is still difficult to properly map, especially below the Bragg peak. It was found that the (202) rod has the best combination of rocking curve width and intensity.

Chapter 6

Conclusions

Crystal truncation rod scattering has been shown to be a powerful technique for determining interfacial roughness non-destructively. By measuring the decay of scattering away from a Bragg reflection in the surface direction an rms roughness of the surface or interface can be extracted. It has been shown that an ordered roughness does not have a different effect on different truncation rods, i.e. the rms roughness obtained from a CTR is independent of the momentum transfer of the Bragg peak associated with that rod. We have obtained rms roughness values with an accuracy of ± 0.1 Å. Sensitivity to lateral length scale roughness ranges from the atomic level as determined by the wavelength of the x-rays to approximately 1 μm depending on the instrument function being employed.

The influence of different cleans, as well as the thermal oxidation process, on the Si-SiO_2 interface was investigated. A hot water treatment prior to thermal oxidation has been shown to roughen the Si-SiO_2 interface, whereas different concentrations of ammonium hydroxide in the SC1 bath did not alter the interface roughness. CTR scattering results also show a smoothing of the interface as a result of the oxidation process even for as little as 60 Å of thermal oxidation.

Comparison between AFM and CTR scattering gives a consistent picture of the relative roughness of the wafers, although the absolute numbers do not agree. The differences in the absolute values can be explained by the difference in lateral roughness scale that the two techniques measure. CTR scattering is sensitive down to the wavelength of the x-rays ($\sim$1.2 Å), whereas AFM is limited by the tip size of the cantilever ($\sim$100 Å). Because the difference in lateral length scale between the two techniques is predominantly at the short wavelength end, this indicates that it is at periodicities below $\sim$100 Å that the increased roughness observed by the x-rays is found. As discussed in the introduction, device characteristics are most sensitive to these relatively short wavelengths.

It has been shown using the layer summation method that crystal truncation rods are always perpendicular to the surface of the crystal, which is consistent with that predicted by the convolution of the Fourier transform of a Heaviside function (e.g. the electron density profile of the sample) onto the reciprocal lattice points. The CTR's are thus tilted with respect to the crystallographic axes when a miscut is present.

Determination of the miscut and its direction can be done effectively by measuring the position of a symmetric Bragg reflection along two different azimuths.

A scheme is presented which ensures that the exact position of the CTR is found prior to measuring the rod intensity. It was employed in measuring the rod intensity for silicon(001) wafers with miscuts of different size. Use of this method removed asymmetry of the rods which was observed otherwise, and thus allowed for a more accurate measurement of the interfacial roughness. The intersection of the instrument function with the rods determines the sensitivity of a particular rod to miscut. An instrument function with a small in-plane component is more likely not to include all of the rod in the scattered intensity than an instrument function with a large in-plane component. Since the plane of the instrument function is almost parallel with the rod associated with the (311) rod, the position of the rod needs to be determined very accurately, even for a 0.1 degree miscut, to avoid artificial asymmetry of the CTR intensity.

These calculations also show that a regular step array does not alter the CTR intensity distribution from that of a perfect flat crystal, only the direction of the rod has changed. If the terrace widths vary the CTR intensity is decreased in the same way roughness influences the rod. In the case of Si(001) a miscut will always cause a decrease in the scattered intensity since one cannot create a regular step array on a diamond cubic lattice.

As shown in this thesis, CTR scattering is a viable technique for measuring interfacial roughness and is especially well suited for the Si-SiO_2 system. The technique is developed to a stage where the next logical step would to be to investigate samples with a higher degree of technological interest. An example would be to measure silicon wafers with different amounts of Fe contamination at the surface prior to oxidation, since that is believed to cause roughening of the Si-SiO_2 interface.

Since reflectivity is the most commonly used x-ray scattering technique for measuring surface roughness, it would be interesting to compare the roughness measured using both reflectivity and CTR scattering on the same samples. Such a comparison might also be useful for determining if the native oxide is conformal, although with a sub-10 Å oxide it would be quite difficult.

Another challenging project, but which might be feasible with the new 3rd generation synchrotrons, would be to extract the height-height correlation function from the decay of the CTR in the in-plane direction. As was shown in Appendix A, roughness gives rise to diffuse scattering in which the in-plane distance to the CTR is inversely related to the roughness wavelength. To observe the diffuse scattering around the main CTR reflection, a higher instrument resolution would be needed. This could be achieved with a smaller slit setting than that used for this work, or one might have to use an analyzer crystal to achieve sufficient angular resolution. Thus, one might be able to characterize the diffuse scattering in the vicinity of the rod and deduce the in-plane length scales of the roughness.

CTR scattering can also be extended to measurements on other materials. Interface structures between crystals and liquids, which are otherwise difficult to determine, are well suited to study by CTR scattering. Both environmental and chemically important systems can be studied as well as the interface of crystals in equilibrium with their own melt.

Appendix A

Scattering from a Grating

The scattered intensity is given by the square of the structure factor F. F can be determined by summing up the form factor f_0 over all atoms in the crystal. For a perfect cubic crystal with N_1, N_2 and N_3 atoms in the [100], [010] and [001] direction, respectively, the structure factor is:

$$\begin{aligned} F &= f_0 \sum_{j_1=0}^{N_1-1} e^{iq_1 a j_1} \sum_{j_2=0}^{N_2-1} e^{iq_2 a j_2} \sum_{j_3=0}^{N_3-1} e^{iq_3 a j_3} \\ &= f_0 \left(\frac{e^{iq_1 a N_1} - 1}{e^{iq_1 a} - 1} \right) \left(\frac{e^{iq_2 a N_2} - 1}{e^{iq_2 a} - 1} \right) \left(\frac{e^{iq_3 a N_3} - 1}{e^{iq_3 a} - 1} \right) \end{aligned} \tag{A.1}$$

where q_1, q_2 and q_3 are the projections of the scattering vector Q onto the three cubic axes.

The cube described above can be thought of as consisting of planes of atoms separated by a distance a. In the [100] direction, the structure factor for the planes perpendicular to that direction would be:

$$\begin{aligned} F_{plane} &= f_0 \sum_{j_2=0}^{N_2-1} e^{iq_2 a j_2} \sum_{j_3=0}^{N_3-1} e^{iq_3 a j_3} \\ &= f_0 \left(\frac{e^{iq_2 a N_2} - 1}{e^{iq_2 a} - 1} \right) \left(\frac{e^{iq_3 a N_3} - 1}{e^{iq_3 a} - 1} \right). \end{aligned} \tag{A.2}$$

A grating can be created by moving every other Λ planes an amount T in the [001] direction. The resulting crystal has a grating on the (001) surface with a periodicity of

2Λ. This regular set of translations is mirrored on the bottom of the crystal. However, for a thick crystal this has no influence on the resulting scattered intensity, and makes the mathematics more clear. A sum over the planes in the [100] direction can be separated into three parts. First a sum over the Λ planes on a terrace: $\sum_{j_4=0}^{\Lambda-1} e^{iq_1aj_4}$. Adding up the structure factor for the terrace next to that one can be done by multiplying by a translation vector from one terrace to the next $e^{i(q_1a\Lambda-q_3aT)}$) onto the previous sum. A sum over the periods M of the grating is given by $\sum_{j_1=0}^{M-1} e^{iq_1a2\Lambda j_1}$. Therefore, the stacking of planes in the [100] direction in a grating with M periods yields the structure factor:

$$F = F_{plane}\left(\sum_{j_4=0}^{\Lambda-1} e^{iq_1aj_4} + e^{i(q_1a\Lambda-q_3aT)}\sum_{j_4=0}^{\Lambda-1} e^{iq_1aj_4}\right)\sum_{j_1=0}^{M-1} e^{iq_1a2\Lambda j_1} \tag{A.3}$$

which can be simplified to:

$$\begin{aligned} F &= F_{plane}\sum_{j_4=0}^{\Lambda-1}(1+e^{i(q_1a\Lambda-q_3aT)})e^{iq_1aj_4}\sum_{j_1=0}^{M-1} e^{iq_1a2\Lambda j_1} \\ &= F_{plane}(1+e^{i(q_1a\Lambda-q_3aT)})\left(\frac{e^{iq_1a\Lambda}-1}{e^{iq_1a}-1}\right)\left(\frac{e^{iq_1a2\Lambda M}-1}{e^{iq_1a2\Lambda}-1}\right). \end{aligned} \tag{A.4}$$

The first sum corresponds to summing up over the atoms of one period (2Λ). The displacement from one step to the next is represented as the phase change given inside the parenthesis in the exponent. The second sum is a sum over all the steps of the crystal. As recast, it is clearer to see that the $(1+e^{i\phi})$ term looks like a basis of two objects with a phase relationship. The complete structure factor of the crystal is thus:

$$F = f_0(1+e^{i(q_1a\Lambda-q_3aT)})\left(\frac{e^{iq_1a\Lambda}-1}{e^{iq_1a}-1}\right)\left(\frac{e^{iq_1a2\Lambda M}-1}{e^{iq_1a2\Lambda}-1}\right)\left(\frac{e^{iq_2aN_2}-1}{e^{iq_2a}-1}\right)\left(\frac{e^{iq_3aN_3}-1}{e^{iq_3a}-1}\right) \tag{A.5}$$

The scattered intensity is given by the square of the structure factor:

$$I = 4|f_0|^2\cos^2(a(q_1\Lambda-q_3T)/2)\frac{\sin^2(q_1a\Lambda/2)}{\sin^2(q_1a/2)}\frac{\sin^2(q_1a\Lambda M)}{\sin^2(q_1a\Lambda)}\frac{\sin^2(q_2aN_2/2)}{\sin^2(q_2a/2)}\frac{\sin^2(q_3aN_3/2)}{\sin^2(q_3a/2)} \tag{A.6}$$

Replacing the scattering vector representation with it's reciprocal space equivalent ($q_1 a = 2\pi h$, $q_2 a = 2\pi k$, $q_3 a = 2\pi l$) yields:

$$I = 4|f_0|^2 \cos^2(\pi(h\Lambda - lT)) \frac{\sin^2(\pi h\Lambda)}{\sin^2(\pi h)} \frac{\sin^2(\pi h 2\Lambda M)}{\sin^2(\pi h 2\Lambda)} \frac{\sin^2(\pi k N_2)}{\sin^2(\pi k)} \frac{\sin^2(\pi l N_3)}{\sin^2(\pi l)} \quad \text{(A.7)}$$

Appendix B

Diamond Cubic Lattice

B.1 No Miscut

The layer summation method was applied to a diamond cubic lattice in Chapter 2. However, when a miscut is present, it is convenient to the describe the crystal as a sum of planes which are perpendicular to the miscut direction rather than perpendicular to the surface normal. The surface unit cell of a diamond cubic structure is shown in Figure B.1 and consists of two types of planes (A & B) perpendicular to the [100] direction. The structure factor from each bilayer (which has a basis of four atoms) is:

$$\begin{aligned} F_{DC-bilayer_\perp} &= f_0(1+e^{2\pi i(\frac{k}{2}-\frac{l}{4})}+e^{2\pi i(\frac{h}{2}+\frac{k}{2}-\frac{l}{2})}+e^{2\pi i(\frac{h}{2}-\frac{3l}{4})})\sum_{j_2=0}^{N_2-1}e^{2\pi ik}\sum_{j_3=0}^{N_3-1}e^{2\pi il} \\ &= f_0(1+e^{\pi i(h+k-l)})(1+e^{\pi i(k-\frac{l}{2})})\left(\frac{e^{2\pi ikN_2}-1}{e^{2\pi ik}-1}\right)\left(\frac{e^{2\pi ilN_3}-1}{e^{2\pi il}-1}\right) \quad \text{(B.1)} \end{aligned}$$

The structure factor of a diamond cubic crystal with a perfectly smooth surface is consequently given by summing the structure factor of the bilayers over all the bilayers present in the crystal:

$$\begin{aligned} F_{DC} &= F_{DC-bilayer_\perp}\sum_{j_1=1}^{N_1}e^{2\pi ihj_1} \\ &= f_0(1+e^{\pi i(h+k-l)})(1+e^{\pi i(k-\frac{l}{2})}) \\ &\quad \left(\frac{e^{2\pi ihN_1}-1}{e^{2\pi ih}-1}\right)\left(\frac{e^{2\pi ikN_2}-1}{e^{2\pi ik}-1}\right)\left(\frac{e^{2\pi ilN_3}-1}{e^{2\pi il}-1}\right), \quad \text{(B.2)} \end{aligned}$$

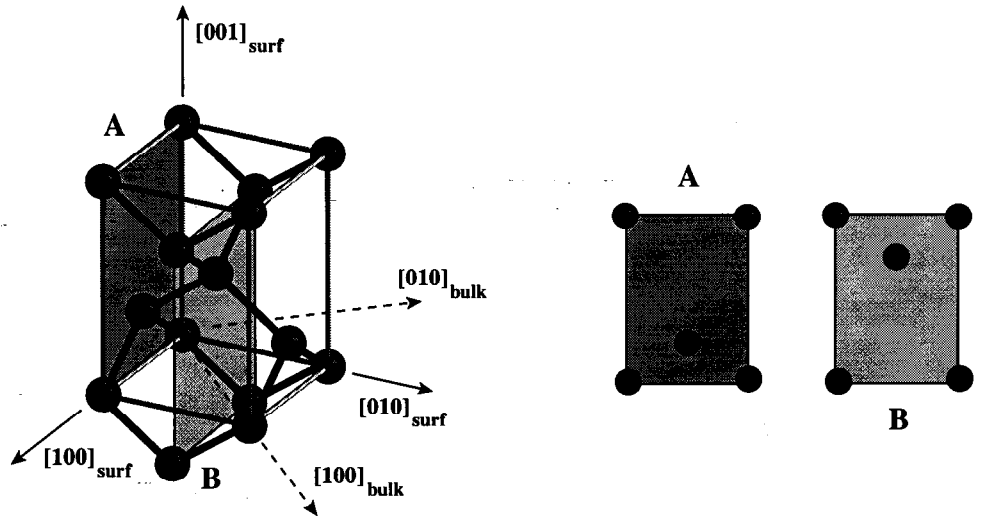

Figure B.1: A diagram of the surface unit cell of the diamond cubic lattice is shown on the left. As indicated with dashed lines, the surface unit cell is rotated 45 degrees with respect to the bulk unit cell. The interatomic bonds are shown as heavy lines and the outline of the unit cell is given by light lines. The surface unit cell consists of two planes (A & B) which contain two atoms each. Their configuration is outlined on the right.

which is identical to Eqn 2.16 derived using bilayers perpendicular to the surface normal.

B.2 Miscut

Termination of a diamond cubic lattice in the [001] direction can be done in two different ways. In one type the atomic bonds of the top layer will be in the [100] direction, whereas the other termination will have atomic bonds in the [010] direction. Introduction of steps onto the (001) surface will cause the surface structure orientation to alternate from terrace to terrace. For simplicity consider the case where the miscut direction is along a step direction, e.g. the [100] direction (i.e. the $[1\bar{1}0]_{bulk}$) with a step array as shown in Figure B.2. Because there is a four atom basis to the unit cell, there can be four different terrace types on the surface and the repeat distance is over four terrace widths. Let the miscut crystal be terminated by N_t periods each consisting of four terraces in the [100] direction, with N_2 unit cells in the [010] direction and N_3 unit cells in the [001] direction. The width of this period is $M_{tot} = 2M_1 + 2M_2 + 1$, where M_1 and M_2 are the number of unit cells on each type of terrace. The extra unit cell arises from the translation vector from one terrace to the next. The structure factor of a single plane is given by:

$$F_{plane} = f_0 \sum_{j_2=0}^{N_2-1} e^{2\pi i k j_2} \sum_{j_3=0}^{N_3-1} e^{2\pi i l j_3} = f_0 \left(\frac{e^{2\pi i k N_2} - 1}{e^{2\pi i k} - 1} \right) \left(\frac{e^{2\pi i l N_3} - 1}{e^{2\pi i l} - 1} \right). \tag{B.3}$$

A sum over all the planes of the four terraces yields:

$$F_{period} = F_{plane}(1 + e^{i\vec{q}\cdot(M_1\vec{a}_1+\vec{t}_1)} + e^{i\vec{q}\cdot((M_1+M_2)\vec{a}_1+\vec{t}_1+\vec{t}_2)} + e^{i\vec{q}\cdot((2M_1+M_2)\vec{a}_1+2\vec{t}_1+\vec{t}_2)}) \sum_{j=0}^{2M_1+2M_2} e^{i\vec{q}\cdot\vec{a}_1 j}, \tag{B.4}$$

where $\vec{t}_1$ is the translation vector from the end of the first to the beginning of the second terrace ($\vec{t}_1 = \frac{1}{4}[20\bar{1}]$) and $\vec{t}_2$ is the translation vector from the end of the second to the start of the third terrace ($\vec{t}_2 = \frac{1}{4}[02\bar{1}]$), as shown in Figure B.2. Thus, in Eqn. B.4, the unit cell of four atoms is represented by the atoms at the four step

edges. A sum of this pseudo-unit cell over all the planes gives the total structure factor of the repeat unit. Evaluating the dot products in Eqn. B.4 yields:

$$\begin{aligned} F_{period} &= f_0(1+e^{2\pi i((M_1+\frac{1}{2})h-\frac{1}{4}l)}+e^{2\pi i((M_1+M_2+\frac{1}{2})h+\frac{1}{2}k-\frac{1}{2}l)}+e^{2\pi i((2M_1+M_2+1)h+\frac{1}{2}k-\frac{3}{4}l)}) \\ &\quad \left(\frac{e^{2\pi ikN_2}-1}{e^{2\pi ik}-1}\right)\left(\frac{e^{2\pi ilN_3}-1}{e^{2\pi il}-1}\right)\left(\frac{e^{2\pi i(2M_1+2M_2+1)h}-1}{e^{2\pi ih}-1}\right) \\ &= f_0(1+e^{2\pi i((M_1+\frac{1}{2})h-\frac{1}{4}l)})(1+e^{2\pi i((M_1+M_2+\frac{1}{2})h+\frac{1}{2}k-\frac{1}{2}l)}) \\ &\quad \left(\frac{e^{2\pi ikN_2}-1}{e^{2\pi ik}-1}\right)\left(\frac{e^{2\pi ilN_3}-1}{e^{2\pi il}-1}\right)\left(\frac{e^{2\pi i(2M_1+2M_2+1)h}-1}{e^{2\pi ih}-1}\right). \end{aligned} \tag{B.5}$$

The structure factor for the whole crystal is then determined by summing the structure factor of one period of four terraces over all the repeat units of the surface:

$$\begin{aligned} F &= F_{period}\sum_{j=0}^{N_t-1} e^{i\vec{q}\cdot((2M_1+2M_2)\vec{a}_1+\vec{t}_1+\vec{t}_2)j} \\ &= F_{period}\left(\frac{e^{2\pi i((2M_1+2M_2+1)h+k-l)N_t}-1}{e^{2\pi i((2M_1+2M_2+1)h+k-l)}-1}\right) \\ &= f_0(1+e^{2\pi i((M_1+\frac{1}{2})h-\frac{1}{4}l)})(1+e^{2\pi i((M_1+M_2+\frac{1}{2})h+\frac{1}{2}k-\frac{1}{2}l)})\left(\frac{e^{2\pi ikN_2}-1}{e^{2\pi ik}-1}\right) \\ &\quad \left(\frac{e^{2\pi ilN_3}-1}{e^{2\pi il}-1}\right)\left(\frac{e^{2\pi iM_{tot}h}-1}{e^{2\pi ih}-1}\right)\left(\frac{e^{2\pi i(M_{tot}h+k-l)N_t}-1}{e^{2\pi i(M_{tot}h+k-l)}-1}\right). \end{aligned} \tag{B.6}$$

The first two factors in the above equation contain the information specific to the structure factor of the unit cell and it is these which determine whether a reflection is allowed. Note also that these are the only factors which contain information about the size of the individual terraces and steps. Only the last two factors contain information about the average miscut of the sample. The second to last factor arises from a sum over the planes of each period and causes peaks at integer positions in the [100] direction. The last factor is a sum of the scattering from all the periods N_t. This leads to rods which are perpendicular to the translation vector from one period to the next $(2(M_1+M_2)\vec{a}_1+\vec{t}_1+\vec{t}_2)$. Consequently, the rods are always perpendicular to the surface of the crystal, since the terrace translation vector is in the plane of the surface. The scattered intensity is given by the square of the structure factor:

$$I = 4|f_0|^2\cos^2(\frac{\pi}{4}((4M_1+2)h-l))\cos^2(\frac{\pi}{2}(M_{tot}h+k-l))\left(\frac{\sin^2(\pi lN_3)}{\sin^2(\pi l)}\right)$$

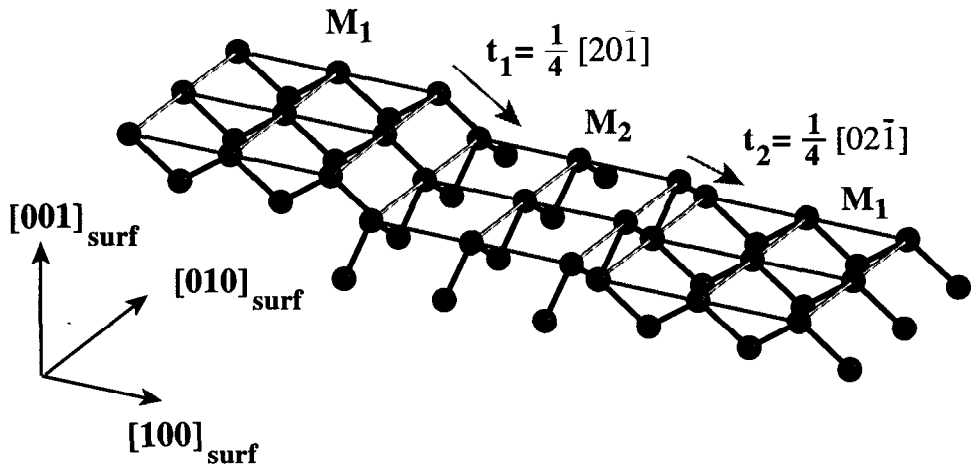

Figure B.2: A diagram is shown of a step array of a diamond cubic lattice with a miscut in the $[100]_{surface}$ direction. The atomic bonds are shown as heavy lines, whereas the outline of the unit cell is shown with light lines. $\vec{t}_1$ and $\vec{t}_2$ represent the translation vectors from the end of one terrace to the beginning of the next terrace. Since there are two types of terraces, one with atomic bonds in the [100] direction and one in [010] direction, there also exist two types of translations.

$$\left(\frac{\sin^2(\pi k N_2)}{\sin^2(\pi k)}\right)\left(\frac{\sin^2(\pi M_{tot} h)}{\sin^2(\pi h)}\right)\left(\frac{\sin^2(\pi(M_{tot}h + k - l)N_t)}{\sin^2(\pi(M_{tot}h + k - l))}\right). \tag{B.7}$$

In Eqn. B.7 the last product determines the tilt of the rod, i.e. h as a function of l for the maximum intensity. For the crystal truncation rod associated with the HKL reflection, h is constrained to:

$$h = H + \frac{l - L}{M_{tot}}, \tag{B.8}$$

for $k = integer$. Note the similarity of this equation to Eqn 5.11, with M replaced here by M_{tot}. Inserting this condition on h into Eqn. B.7 gives the intensity along the rod as a function of l only:

$$\begin{aligned} I_{ctr} \;=\; & 4|f_0|^2 \cos^2\left(\frac{\pi}{4}((4M_1+2)(H + \frac{l-L}{M_{tot}}) - l)\right)\cos^2\left(\frac{\pi}{2}(M_{tot}H + K - L)\right) \\ & \left(\frac{\sin^2(\pi K N_2)}{\sin^2(\pi K)}\right)\left(\frac{\sin^2(\pi l N_3)}{\sin^2(\pi l)}\right)\left(\frac{\sin^2(\pi(H + l - L))}{\sin^2(\pi(H + (l-L)/M_{tot}))}\right) \\ & \left(\frac{\sin^2(\pi(M_{tot}H + K - L)N_t)}{\sin^2(\pi(M_{tot}H + K - L))}\right). \end{aligned} \tag{B.9}$$

Since M_{tot}, H, K and L are all integers, the equation can be further simplified to:

$$I_{ctr} = 4|f_0|^2 \cos^2(\frac{\pi}{4}(2H + (4M_1 + 2)\frac{l-L}{M_{tot}} - l)) \cos^2(\frac{\pi}{2}(M_{tot}H + K - L)) \left(\frac{N_2^2 N_t^2}{2\sin^2(\pi(l-L)/M_{tot})}\right). \quad \text{(B.10)}$$

Since $\sin^2(x)$ can be approximated as x^2 for small values of x, the rod profile can be written as:

$$I_{ctr} = 4|f_0|^2 \cos^2(\frac{\pi}{4}(2H + (4M_1 + 2)\frac{l-L}{M_{tot}} - l)) \cos^2(\frac{\pi}{2}(M_{tot}H + K - L))\frac{N_2^2 N_t^2 M_{tot}^2}{2\pi^2(l-L)^2}. \quad \text{(B.11)}$$

The first $cos^2()$ in Eqn. B.11 arises from a combination of the steps and the basis of the unit cell, whereas the second $cos^2()$ is only a function of the unit cell. This latter goes to zero when $H + K + L$ is an odd number, since $M_{tot} = 2M_1 + 2M_2 + 1$ is always an odd number. This corresponds to one of the conditions for destructive interference in diamond cubic lattices. For this lattice the non-allowed reflections are given in surface units by:

$$\begin{aligned} H + K + L &= 2n + 1 \qquad n = integer \\ 2H + L &= 4n + 2 \qquad n = integer. \end{aligned} \quad \text{(B.12)}$$

If $4M_1+2$ equals M_{tot}, i.e. the terrace widths of the two types of terraces are identical, then the first product would be reduced to $\cos^2(\frac{\pi}{4}(2H-L))$, which corresponds to the second condition for destructive interference of the diamond cubic lattice. However, due to the nature of the translation vectors from one terrace to the next, the two type of terraces cannot have the same width and, therefore, one cannot create a perfect regular step array of a diamond cubic crystal. The effect of a non-perfect step array is a decay of the scattered intensity as a function of the distance from the Bragg reflection analogous to that caused by roughness of the surface. Thus a diamond cubic (001) surface with miscut is inherently rough.

Bibliography

[1] T. Ohmi, M. Miyashita, M. Itano, T. Imaoka, and I. Kawanabe. Dependence of thin-oxide films quality on surface microroughness. *IEEE Transactions on Electron Devices*, 39:537, 1992.

[2] T. Ohmi, K. Kotani, A. Teramoto, and M. Miyashita. Dependence of electron channel mobility on Si-SiO_2 interface microroughness. *IEEE Elec. Device Lett.*, 12:652, 1991.

[3] L. G. Parratt. Surface studies of solids by total reflection of x-rays. *Phys. Rev.*, 95:359, 1954.

[4] L. Nevot and P. Croce. Caractérisation des surfaces par réflexion rasante de rayons X. Application à l'étude du polissage de quelques verres silicates. *Revue Phys. Appl.*, 15:761, 1980.

[5] L. Brugemann, R. Bloch, W. Press, and P. Gerlach. Surface and interface topography of amorphous SiO_2/crystalline Si(001) studied by x-ray diffraction. *J. Phys.: Condens. Matter*, 2:8869, 1990.

[6] T. A. Rabedeau, I. M. Tidswell, P. S. Pershan, J. Bevk, and B. S. Freer. X-ray scattering studies of the SiO_2/Si(001) interfacial structure. *Appl. Phys. Lett.*, 59:706, 1991.

[7] T. A. Rabedeau, I. M. Tidswell, P. S. Pershan, J. Bevk, and B. S. Freer. X-ray reflectivity studies of SiO_2/Si(001). *Appl. Phys. Lett.*, 59:3422, 1991.

[8] O. Sakata, A. Y. Nikulin, and H. Hashizume. X-ray evaluation of microroughness of mechanochemically polished silicon surfaces. *Jpn. J. Appl. Phys.*, 32:L616, 1993.

[9] P. H. Fuoss, L. J. Norton, S. Brennan, and A. Fischer-Colbrie. X ray scattering studies of the Si-SiO_2 interface. *Phys. Rev. Lett.*, 60:600, 1988.

[10] G. Renaud, P. H. Fuoss, A. Ourmazd, J. Bevk, B. S. Freer, and P. O. Hahn. Native oxidation of the Si(001) surface: Evidence for an interfacial phase. *Appl. Phys. Lett.*, 58:1044, 1991.

[11] G. Binnig, C. F. Quate, and C. Gerber. Atomic force microscope. *Phys. Rev. Lett.*, 56:930, 1986.

[12] A. G. Gilicinski, R. M. Rynders, S. E. Beck, Y. E. Strausser, J. R. Stets, B. S. Felker, and D. A. Bohling. Study of silicon surface roughness by atomic force microscopy. *MRS Symp. Proc.*, 324:391, 1994.

[13] M. Kimura, J. Mitsuhashi, and H. Koyama. Si/SiO_2 interface states and neutral oxide traps induced by surface microroughness. *J. Appl. Phys.*, 77:1569, 1995.

[14] A. Crossley, C. J. Sofield, J. P. Goff, A. C. I. Lake, M. T. Hutchings, and A. Menelle. A study comparing measurements of roughness of silicon and SiO_2 surfaces and interfaces using scanning probe microscopy and neutron reflectivity. *J. Non-Cryst. Solids*, 187:221, 1995.

[15] G. S. Shekhawat, R. P. Gupta, S. S. Shekhawat, D. P. Runthala, P. D. Vyas, P. Srivastava, S. Venkatesh, K. Mamhoud, and K. B. Garg. Scanning tunneling microscopy of Si/SiO_2 interface roughness and its dependence on growth conditions. *Appl. Phys. Lett.*, 68:114, 1996.

[16] S. R. Andrews and R. A. Cowley. Scattering of x-rays from crystal surfaces. *J. Phys. C: Solid State Phys.*, 18:6427, 1985.

[17] I. K. Robinson. Crystal truncation rods and surface roughness. *Phys. Rev. B*, 33(6):3830, 1986.

[18] I. K. Robinson, W. K. Waskiewicz, R. T. Tung, and J. Bohr. Ordering of Si(111)/a-Si and Si(111)/SiO_2 interfaces. *Phys. Rev. Lett.*, 57(21):2714, 1986.

[19] I. K. Robinson, R. T. Tung, and R. Feidenhans'l. X-ray interference method for studying interface structures. *Phys. Rev. B*, 38(5):3632, 1988.

[20] P. A. Bennett, B. DeVries, I. K. Robinson, and P. J. Eng. Layerwise reaction at a buried interface. *Phys. Rev. Lett.*, 69:2539, 1992.

[21] C. A. Lucas, D. Loretto, and G. C. L. Wong. Epitaxial growth mechanisms and structure of CaF_2/Si(111). *Phys. Rev. B*, 50(19):14230, 1994.

[22] R. G. v. Silfhout, J. F. v. d. Veen, C. Norris, and J. E. Macdonald. Structure of the Ge(111)-c(2×8) surface as determined from scattered x-ray intensities along crystal truncation rods. *Faraday Discuss. Chem. Soc.*, 89:169, 1990.

[23] I. K. Robinson, E. Vlieg, and K. Kern. Structure and roughening of the Pt(110) surface. *Faraday Discuss. Chem. Soc.*, 89:159, 1990.

[24] D. Gibbs, B. M. Ocko, D. M. Zehner, and S. G. J. Mochrie. Absolute x-ray reflectivity study of Au(100) surface. *Phys. Rev. B*, 38:7303, 1988.

[25] H. Hong, R. D. Aburano, K.-S. Chung, D.-S. Lin, E. S. Hirschorn, T.-C. Chiang, and H. Chen. X-ray truncation rod study of Ge(001) surface roughening by molecular beam homoepitaxial growth. *J. Appl. Phys.*, 79:6858, 1996.

[26] H. Reichert, P. J. Eng, H. Dosch, and I. K. Robinson. Thermodynamics of surface segregation profiles at Cu_3Au(001) resolved by x-ray scattering. *Phys. Rev. Lett.*, 74(11):2006, 1995.

[27] Y. Kashihara. X-ray crystal truncation rod scattering: General intensity formula for no lateral displacements of surface atoms. *Surf. Sci.*, 232:417, 1990.

[28] J. Harada. Evaluation of the roughness of a crystal surface by x-ray scattering. I. theoretical considerations. *Acta Cryst. A*, 48:764, 1992.

[29] S. Nakatani and T. Takahashi. Dynamical treatment of x-ray reflection from crystal surfaces. *Surf. Sci.*, 311:433, 1994.

[30] T. Takahashi and S. Nakatani. Dynamical theory of x-ray diffraction for the study of crystal surfaces. *Surf. Sci.*, 326:347, 1995.

[31] R. A. Cowley and T. W. Ryan. X-ray scattering studies of thin films and surfaces: thermal oxides on silicon. *J. Phys D: Appl. Phys.*, 20:61, 1987.

[32] R. A. Cowley and C. Lucas. X-ray scattering measurements of silicon oxides on silicon. *Colloque de Phys.*, 7:145, 1989.

[33] M.-T. Tang, K. W. Evans-Lutterodt, G. S. Higashi, and T. Boone. Roughness of the silicon(001)/SiO_2 interface. *Appl. Phys. Lett.*, 62(24):3144, 1993.

[34] M. T. Tang, K. W. Evans-Lutterodt, M. L. Green, D. Brasen, K. Krisch, L. Manchanda, G. S. Higashi, and T. Boone. Growth temperature dependence of the Si(001)/SiO_2 interface width. *Appl. Phys. Lett.*, 64(6):748, 1994.

[35] M. L. Green, D. Brasen, K. W. Evans-Lutterodt, L. C. Feldman, K. Krisch, W. Lennard, H.-T. Tang, L. Manchanda, and M.-T. Tang. Rapid thermal oxidation of silicon in N_2O between 800 and 1200°C: Incorporated nitrogen and interfacial roughness. *Appl. Phys. Lett.*, 65(7):848, 1994.

[36] J. L. Dawson, K. Krisch, K. W. Evans-Lutterodt, M.-T. Tang, L. Manchanda, M. L. Green, D. Brasen, G. S. Higashi, and T. Boone. Kinetic smoothening: Growth thickness depence on the interface width of the Si(001)/SiO_2 interface. *J. Appl. Phys.*, 77(9):4746, 1995.

[37] K. W. Evans-Lutterodt and M.-T. Tang. Spectral sensitivities of x-ray diffraction to the roughness of Si/SiO_2 interfaces. *MRS Symp. Proc.*, 355:373, 1995.

[38] B. E. Warren. *X-Ray Diffraction.* Dover Publications, Inc., New York, 1969.

[39] I. K. Robinson. General discussion. *Faraday Discuss. Chem. Soc.*, 89:201, 1990.

[40] Y. Kashihara, K. Kawamura, and J. Harada. X-ray crystal truncation rod scattering: II. An effect of two-dimensional symmetry of the GaAs(001) surface. *Surf. Sci.*, 257:210, 1991.

[41] A. Munkholm, S. Brennan, F. Comin, and L. Ortega. Observation of a distributed epitaxial oxide in thermally grown SiO_2 on Si(001). *Phys. Rev. Lett.*, 75:4254, 1995.

[42] I. K. Robinson and D. J. Tweet. Surface x-ray diffraction. *Rep. Prog. Phys.*, 55:599, 1992.

[43] D. Vaughan. *X-ray data booklet.* Lawrence Berkeley Laboratory, Berkeley, 1986.

[44] R. W. James. *The optical principles of the diffraction of x-rays.* Ox Bow Press, Woodbridge, Connecticut, 1948.

[45] W. H. Zachariasen. *Theory of X-Ray Diffraction in Crystals.* John Wiley and Sonc, Inc., New York, 1945.

[46] W. R. Busing and H. A. Levy. Angle calculations for 3- and 4-circle x-ray and neutron diffractometers. *Acta Cryst.*, 22:457, 1967.

[47] S. Brennan and P. L. Cowan. A suite of programs for calculating x-ray absorption, reflection and diffraction performance for a variety of materials at arbitrary wavelengths. *Rev. Sci. Instrum.*, 63:992, 1992.

[48] S. Brennan. *SUPERvisor: A Program for collecting synchrotron beam line data.* SSRL, 1997.

[49] E. D. Specht and F. J. Walker. A method for the accurate determination of crystal truncation rod intensities by x-ray diffraction. *J. Appl. Cryst.*, 26(2):166, 1993.

[50] D. E. Gray. *American Institute of Physics Handbook.* McGraw-Hill, New York, 1982.

[51] D. T. Cromer and J. B. Mann. X-ray scattering factors computed from numerical Hartee-Fock wave functions. *Acta Cryst. A*, 24:321, 1968.

[52] P. H. Dederichs. The theory of diffuse x-ray scattering and its application to the study of point defects and their clusters. *J. Phys. F: Metal Phys.*, 3:471, 1973.

[53] S. M. Heald and J. B. Hastings. Grazing incidence optics for synchrotron radiation x-ray beamlines. *Nucl. Instrum. and Meth.*, 187:553, 1981.

[54] S. K. Sinha, E. B. Sirota, S. Garoff, and H. B. Stanley. X-ray and neutron scattering from rough surfaces. *Phys. Rev. B*, 38(4):2297, 1988.

[55] W. Kern and D. Puotinen. *RCA Rev.*, 31:187, 1970.

[56] A. Munkholm, S. Brennan, and J. P. Goodbread. Wafer cleaning influence on the roughness of the Si/SiO_2 interface. *MRS Symp. Proc.*, 386:303, 1995.

[57] H.-N. Yang, G.-C. Wang, and T.-M. Lu. *Diffraction from Rough Surfaces and Dynamic Growth Fronts.* World Scientific, Singapore, 1993.

[58] M. Niwa, T. Kouzaki, K. Okada, M. Udagawa, and R. Sinclair. Atomic-order planarization of ultrathin SiO_2/Si(001) interfaces. *Jpn. J. Appl. Phys.*, 33(1):388, 1994.

[59] Y. Homma, M. Suzuki, and N. Yabumoto. Observation of atomic step morphology on silicon oxide surfaces. *Journal of Vacuum Science and Technology A*, 10(4):2055, 1992.

[60] G. Renaud, P. H. Fuoss, J. Bevk, and B. S. Freer. Grazing-incidence x-ray-scattering study of step-step correlations on Si(001) surfaces. *Phys. Rev. B*, 45(16):9192, 1992.

[61] C. S. Lent and P. I. Cohen. Diffraction from stepped surfaces: I. Reversible surfaces. *Surf. Sci.*, 139:121, 1984.

[62] P. R. Pukite, C. S. Lent, and P. I. Cohen. Diffraction from stepped surfaces: II. Arbitrary terrace distribution. *Surf. Sci.*, 161:39, 1985.

[63] D. Saloner, J. A. Martin, M. C. Tringides, D. E. Savage, C. E. Aumann, and M. G. Lagally. Determination of terrace size and edge roughness in vicinal Si(100) surfaces by surface-sensitive diffraction. *J. Appl. Phys.*, 61(8):2884, 1987.

[64] N. C. Bartelt, T. L. Einstein, and E. D. Williams. Diffraction from stepped surfaces in thermal equilibrium. *Surf. Sci.*, 244:149, 1991.